creative commons
COMMONS DEED

저작자표시-비영리-변경금지 2.0 대한민국

이용자는 아래의 조건을 따르는 경우에 한하여 자유롭게

- 이 저작물을 복제, 배포, 전송, 전시, 공연 및 방송할 수 있습니다.

다음과 같은 조건을 따라야 합니다:

저작자표시. 귀하는 원저작자를 표시하여야 합니다.

비영리. 귀하는 이 저작물을 영리 목적으로 이용할 수 없습니다.

변경금지. 귀하는 이 저작물을 개작, 변형 또는 가공할 수 없습니다.

- 귀하는, 이 저작물의 재이용이나 배포의 경우, 이 저작물에 적용된 이용허락조건을 명확하게 나타내어야 합니다.
- 저작권자로부터 별도의 허가를 받으면 이러한 조건들은 적용되지 않습니다.

저작권법에 따른 이용자의 권리는 위의 내용에 의하여 영향을 받지 않습니다.

이것은 이용허락규약(Legal Code)을 이해하기 쉽게 요약한 것입니다.

Disclaimer

dCollection

ULSAN NATIONAL INSTITUTE OF
SCIENCE AND TECHNOLOGY

Doctoral Thesis

Study of Exsolved Nanocatalysts on Perovskite Oxide Supports for Solid Oxide Fuel Cells and Dry Reforming of Methane

Sangwook Joo

School of Energy and Chemical Engineering
(Energy Engineering)

Ulsan National Institute of Science and Technology

2021

ULSAN NATIONAL INSTITUTE OF
SCIENCE AND TECHNOLOGY

Study of Exsolved Nanocatalysts on Perovskite Oxide Supports for Solid Oxide Fuel Cells and Dry Reforming of Methane

Sangwook Joo

School of Energy and Chemical Engineering
(Energy Engineering)

Ulsan National Institute of Science and Technology

ULSAN NATIONAL INSTITUTE OF
SCIENCE AND TECHNOLOGY

Study of Exsolved Nanocatalysts on Perovskite Oxide Supports for Solid Oxide Fuel Cells and Dry Reforming of Methane

A thesis/dissertation submitted to
Ulsan National Institute of Science and Technology
in partial fulfillment of the
requirements for the degree of
Doctor of Philosophy

Sangwook Joo

01/08/2021 of submission

Approved by

Advisor
Guntae Kim

ULSAN NATIONAL INSTITUTE OF SCIENCE AND TECHNOLOGY

Study of Exsolved Nanocatalysts on Perovskite Oxide Supports for Solid Oxide Fuel Cells and Dry Reforming of Methane

Sangwook Joo

This certifies that the thesis/dissertation of Sangwook Joo is approved.

01/08/2021 of submission

Signature

Advisor: Guntae Kim

Signature

Jong-Beom Baek: Thesis Committee Member #1

Signature

Hyun-Kon Song: Thesis Committee Member #2

Signature

Jeong Woo Han: Thesis Committee Member #3

Signature

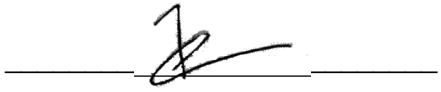

WooChul Jung: Thesis Committee Member #4;

ULSAN NATIONAL INSTITUTE OF
SCIENCE AND TECHNOLOGY

Abstract

In the midst of a surge in future energy demand, heterogeneous catalysts play an essential role in building systems that effectively utilize available resources. When designing a catalyst, it is important to ensure stability and catalytic activity. Exsolution is an effective preparation tool, in this respect, because exsolution grows nanoparticles *in-situ* from the bulk lattice of support oxide under operating conditions. Accordingly, it gives "embedded" property and can prevent deactivation due to coarsening of catalyst through immobilization. Exsolution occurs with the formation of an oxygen vacancy in a reducing atmosphere. Therefore, methods such as temperature control, A-site non-stoichiometry, voltage biasing, lattice strain, and phase transition to make oxygen vacancy have been studied to control the degree of exsolution. In addition to these methods, we have been working on a unique method so-called topotactic exsolution. Topotactic exsolution further increases the number of active exsolved nanoparticles through the exchange with the internal target cation *via* the introduction of the external cation, contributing to the enhanced performance of the catalysts. That is, external cations fill the B-site vacancies within the perovskite, adding to the chemical stability of the structure of the catalyst while also ensuring catalytic activity. This simple yet original method is expected to lead to more research in the field of energy utilization as a way to maximize the advantages of exsolution, which can convert most of the potential cations to nanocatalysts. This dissertation focuses on the applications of an energy conversion device using topotactic exsolution, beginning with the basic and theoretical explanation of solid oxide fuel cell (SOFC) and dry reforming of methane (DRM). In chapter 2, a study on $YBa_{0.5}Sr_{0.5}Co_{2-x}Fe_xO_{5+\delta}$ cathode to help overall understanding of SOFC, and in chapter 3, a study on the first topotactic exsolution, in chapter 4, extended study of topotactic exsolution using different cation, and in chapter 5, topotactic exsolution using atomic layer deposition (ALD) on simple perovskite support oxide are discussed.

ULSAN NATIONAL INSTITUTE OF
SCIENCE AND TECHNOLOGY

ULSAN NATIONAL INSTITUTE OF SCIENCE AND TECHNOLOGY

Contents

ULSAN NATIONAL INSTITUTE OF SCIENCE AND TECHNOLOGY

ULSAN NATIONAL INSTITUTE OF SCIENCE AND TECHNOLOGY

ULSAN NATIONAL INSTITUTE OF
SCIENCE AND TECHNOLOGY

ULSAN NATIONAL INSTITUTE OF SCIENCE AND TECHNOLOGY

List of Figures

ULSAN NATIONAL INSTITUTE OF SCIENCE AND TECHNOLOGY

ULSAN NATIONAL INSTITUTE OF SCIENCE AND TECHNOLOGY

ULSAN NATIONAL INSTITUTE OF SCIENCE AND TECHNOLOGY

ULSAN NATIONAL INSTITUTE OF SCIENCE AND TECHNOLOGY

ULSAN NATIONAL INSTITUTE OF
SCIENCE AND TECHNOLOGY

for Bulk Ni, Bulk Ni-Fe 0.70, and Bulk Ni-Fe 0.60. (E) Time-dependence of CH_4 reactivity and H_2/CO ratio for LSTN-20C-Fe in dry reforming of methane at 700 ^oC.

ULSAN NATIONAL INSTITUTE OF SCIENCE AND TECHNOLOGY

List of Tables

ULSAN NATIONAL INSTITUTE OF SCIENCE AND TECHNOLOGY

Chapter 1 Introduction

1.1. Research background

Population growth, urbanization, and an advance in living standards have dramatically elevated the world's energy demand and environmental burden over the half-century.[1], [2] Energy demand is also expected to continue to increase in the future, causing environmental problems that can no longer tolerate. Indeed, a dramatic increase in atmospheric CO_2 concentrations (Figure 1-1) has led to global warming, threatening human life with extreme climate change, such as a reduction in glaciers/sea-ice/permanent soil layers, and an increase in extreme climate/heat/drought/storm/typhoons.[3]

While the fundamental solution to all energy and environmental problems is elusive, heterogeneous catalysis can play an important role in designing an efficient and appropriate system to maximize the utilization of available resources.[2] By using catalytic reagents, the temperature and waste of transformation can be reduced and the selectivity of the reaction can be increased. In particular, supported metal nanocatalysts, in this regard, have been emphasized in their importance in various catalyst applications owing to the unique properties that arise from their size, shape, and composition.[2], [4], [5] When designing them, it is essential to secure stability and catalytic activity by immobilizing high-surface-area particles through supporting materials. Several preparation methods for supported metal nanocatalysts have been commonly used such as thermal evaporation, pulsed laser deposition, chemical vapor deposition, electrochemical deposition, sol-gel/colloidal techniques, and impregnation methods. However, the deposited metal nanoparticles may undergo agglomeration and

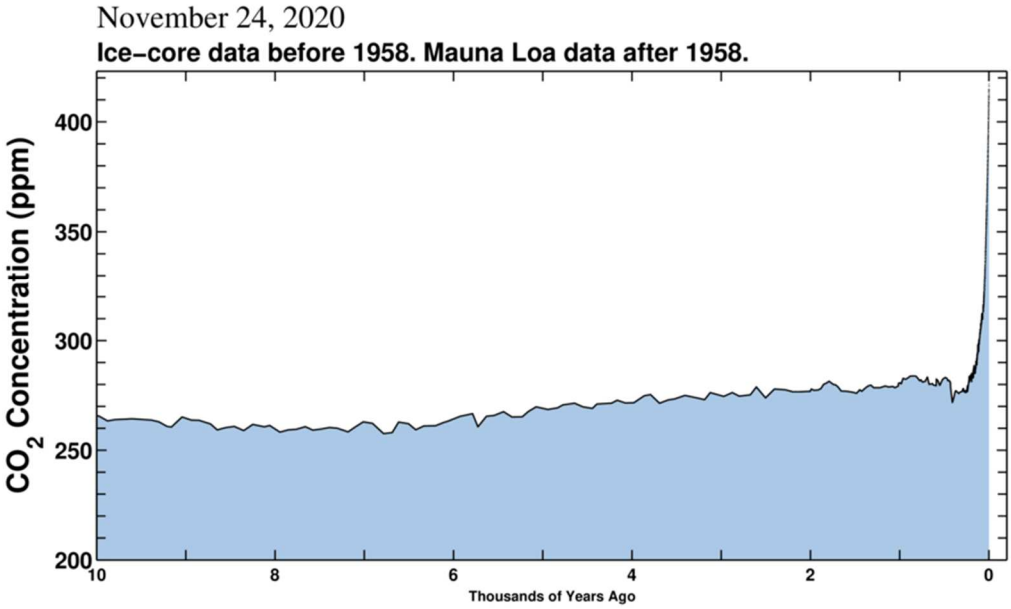

Figure 1-1 Atmospheric CO_2 concentration (ppm) over years[32]

ULSAN NATIONAL INSTITUTE OF
SCIENCE AND TECHNOLOGY

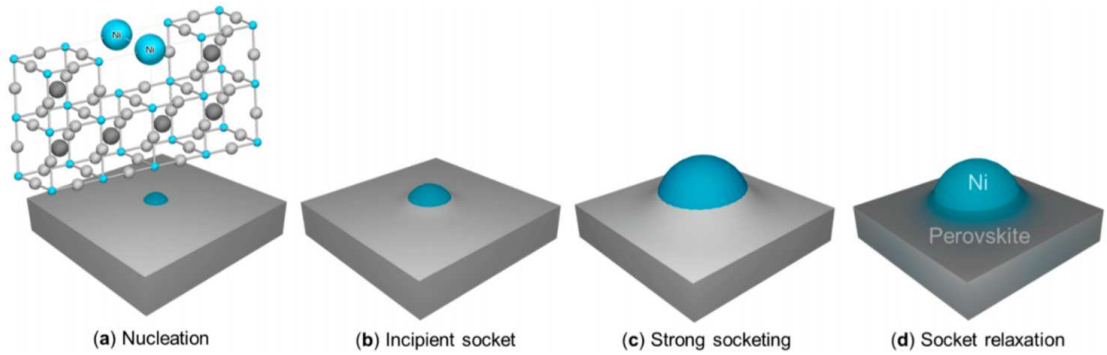

Figure 1-2 Schematic illustration of particle−socket genesis during exsolution. (a) Nucleation at different length scales depicting the particle as partly embedded within the perovskite surface as a consequence of the metal segregating out of the perovskite lattice. (b) As the particle grows isotropically (laterally and vertically), it pushes the perovskite lattice, lifting it slightly. (c) Further growth of the particle leads to a volcano-shaped nanostructure around it. (d) The volcano shape interface eventually relaxes but retains confinement of the particle.[33]

coarsening during operating conditions, leading to fatal performance degradation. Thus, an exsolution technique has been received extensive attention as a promising alternative.[6], [7]

1.2. Exsolution

Exsolution is an effective preparation means of supported active metal particles due to its excellent carbon coking resistance and sintering resistance.[8]–[11] Specifically, exsolution refers to nanoparticles *in-situ* growing on the oxide surface from the cations doped into the support oxide in reducing atmosphere (Figure 1-2). The produced nanoparticles have a strong metal-support interaction (SMSI) owing to their well dispersed and “embedded” properties on the support oxide surface, which provides an advantageous feature for catalyst stability compared to the existing wet impregnation or vapor deposition method.[4] In detail, nanoparticles generated through exsolution are embedded on the oxide surface, so even when carbon growth occurs in an operating environment containing carbon species as a reactant, it occurs in the form of base growth rather than tip growth (Figure 1-3). In tip growth, the nano-catalyst is separated from the supporting material, and agglomeration of the catalyst occurs, leading to deactivation, whereas, in base growth, since the catalyst is settled on the supporting material as it is, more than a certain amount of carbon is no longer produced: carbon tolerance.

Since the exsolution occurs under a reducing atmosphere, a general driving force of exsolution is associated with an oxygen vacancy formation in the perovskite oxides. The oxygen vacancy formation destabilizes the lattice stoichiometry, causing the segregation of B-site cations to maintain structural stability. Several driving forces, such as temperature, non-stoichiometry by A-site defect, voltage biasing, strain, phase transition, and topotactic ion exchange, have been introduced to form the oxygen vacancy (Figure 1-4). However, the degree of oxygen vacancy formation differs for each perovskite structure.

ULSAN NATIONAL INSTITUTE OF SCIENCE AND TECHNOLOGY

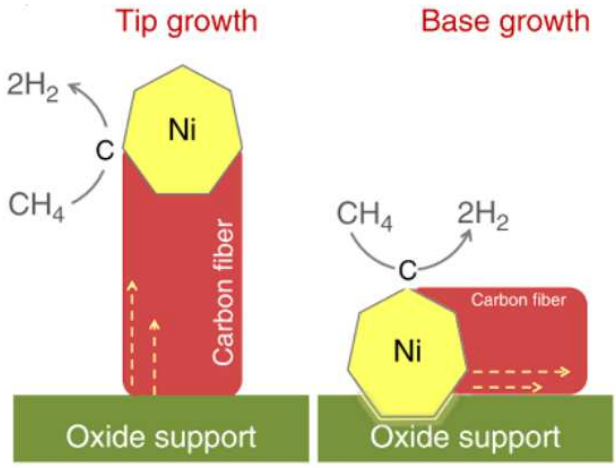

Figure 1-3 Schematic of possible carbon fiber growth mechanisms based on conventional deposition method and exsolution.[8]

As support oxide materials for exsolution, materials based on single perovskite (ABO_3), double perovskite ($A_2B_2O_{5+\delta}$), Ruddlesden Popper (RP, $A_{n+1}B_nO_{3n+1}$), and fluorite (AO_2) have been intensively studied. Among these, perovskite materials, in particular, have excellent structural stability which can withstand lattice mismatch between A-O and B-O bonds, enabling the study of doping various ions at each site. Early exsolution studies were based on a stoichiometric simple perovskite with an A/B ratio of 1. In this case, only cations which are easy to reduce (e.g., Ni^{2+}, Ru^{2+}, Rh^{4+}, Pd^{4+}, and Pt^{4+}) can be exsolved, and only cations near the surface can be released to the surface, limiting the number of exsolved nanoparticles with catalytic active sites. Besides, as the B site falls out of the grid, the lattice becomes unstable, which causes A-site cation segregation of the insulating layer. Therefore, to solve this problem, the perovskites (A/B < 1) with A-site deficiency have been developed.[8], [10] In this case, the A-site deficient perovskites can prevent A-site segregation by having a defect-free perovskite as exsolution proceeds, and the cations which are difficult to reduce under the same conditions can be easily exolved. Recently, topotactic exsolution has been studied as a way to create embedded alloy nanoparticles while maximizing the advantages of the exsolution.[9], [12], [13] Through the method, most of the doped metal cation is exsolved to the surface without leaving cation defects in the parent oxide lattice, rendering the enhanced performance of the exsolved particles while maintaining the overall structural properties of the original support oxide.

The main research objective of the dissertation is to develop highly efficient and stable energy conversion devices using the exsolution phenomenon.

Chapter 1 provides the theoretical backgrounds of the exsolution and its application. In chapter 2, B-site Fe-doped $YBa_{0.5}Sr_{0.5}Co_{2-x}Fe_xO_{5+\delta}$ was investigated for SOFC cathode. In chapter 3, alloy nanoparticles prepared *via* topotactic exsolution was reported to enhance the catalytic activity as a SOFC anode and catalyst for dry reforming of methane. In chapter 4, Ni-Fe bimetallic nanocatalysts

ULSAN NATIONAL INSTITUTE OF SCIENCE AND TECHNOLOGY

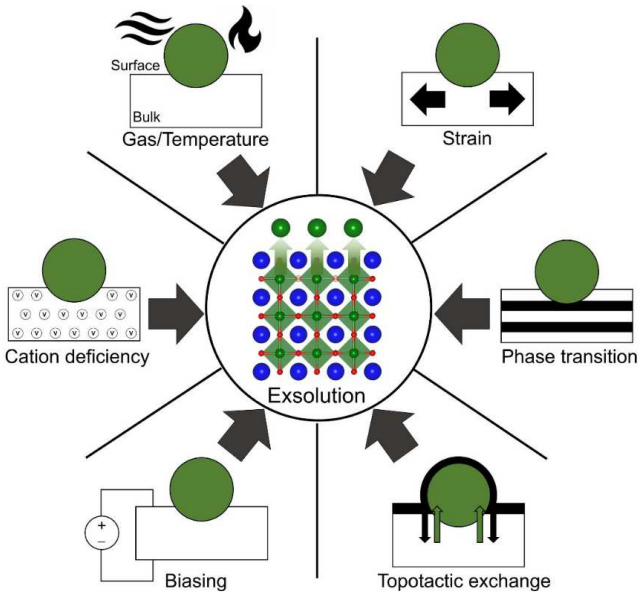

Figure 1-4 Driving forces to promote the exsolution in perovskite oxides: gas/temperature, cation deficiency, biasing, strain, phase transition, and topotactic exchange. In the driving forces, the green spheres indicate exsolved nanoparticle. In the middle circle, blue, green, and red spheres indicate A-site cation, B-site cation, and oxygen, respectively.[9]

produced by topotactic exsolution for dry reforming of methane were reported. In chapter 5, in-situ grown Ni-Fe Nanoparticles on perovskite *via* atomic layer deposition were reported.

1.3. Solid Oxide Fuel Cell (SOFC)

1.3.1. Overview

Solid oxide fuel cell (SOFC) is one of the energy conversion devices that directly convert chemical energy into electrical energy. SOFC mainly operates between 500 °C and 1000 °C and has advantages such as fuel flexibility, high efficiency, and the possibility to utilize high-quality waste heat from high temperatures. The electrical efficiency of SOFC is about 50–60%, but in combined heat and power applications, the efficiency reaches 90%. SOFC is largely composed of three components: a solid electrolyte, a cathode, and an anode (Figure 1-5). The solid electrolyte blocks gas diffusion and electron transfer between the electrodes and only transfers ions. Therefore, the electrolyte must be stable in a redox environment and must be chemically, physically, and mechanically compatible with the electrode materials. Considering the operating environment, the cathode should be a material that has electron/ion conductivity while it must withstand a highly oxidizing atmosphere at high temperature. The anode must withstand a very reducing atmosphere with high electron/ion conductivity.

Specifically, oxygen ions are generated by an oxygen reduction reaction (ORR) in the cathode as shown in the following equation (1.1).

$$\frac{1}{2}O_2 + 2e^- \rightarrow O^{2-} \qquad (1.1)$$

ULSAN NATIONAL INSTITUTE OF SCIENCE AND TECHNOLOGY

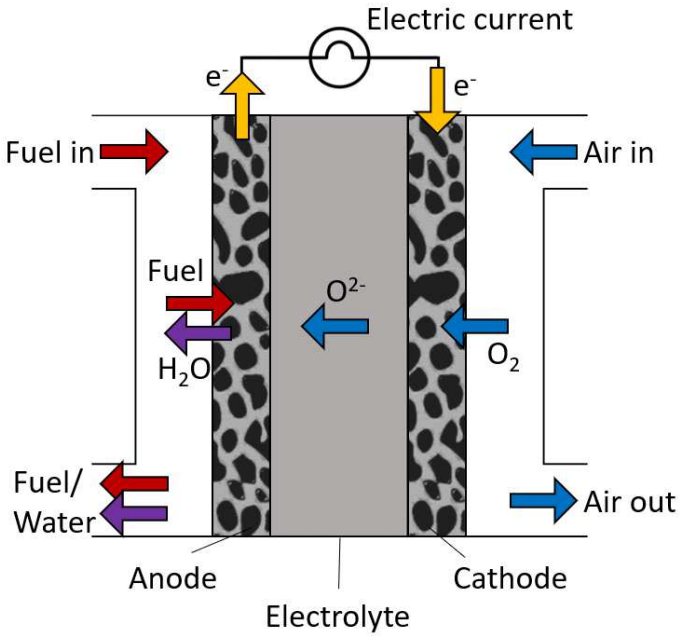

Figure 1-5 Schematic diagram of solid oxide fuel cell

The generated oxygen ions are transferred to the anode through the solid electrolyte, and the transferred oxygen ions participate in the hydrogen oxidation reaction (HOR) to generate water and electrons as shown in equation (1.2).

$$H_2 + O^{2-} \rightarrow H_2O + 2e^- \quad (1.2)$$

1.3.2. Theoretical background

1.3.2.1. Thermodynamic of SOFC

The potential of a system to do electrical work is measured in voltage (also called electrical potential). The electrical work performed when charge Q moves through electrical potential E is as follows.

$$W_{elec} = EQ \quad (1.3)$$

If the charge is caused by the movement of electrons,

$$Q = nF \quad (1.4)$$

where n is the number of moles of electrons transferred and F is the Faraday constant. The maximum electrical work is given as a negative value of Gibbs free-energy difference, as shown below.

$$W_{elec} = -\Delta g_{rxn} \quad (1.5)$$

When the above equations (1.3), (1.4), and (1.5) are all combined, it becomes as follows.

$$\Delta \hat{g} = -nFE \quad (1.6)$$

For example, in a fuel cell where hydrogen and water react, the reaction is

$$H_2 + \frac{1}{2}O_2 \leftrightharpoons H_2O \quad (1.7)$$

ULSAN NATIONAL INSTITUTE OF SCIENCE AND TECHNOLOGY

The Gibbs free-energy change in the reaction is –237 kJ/mol under standard-state conditions, so the reversible voltage is as follows.

$$E^0 = -\frac{\Delta\hat{g}^0_{rxn}}{nF} = -\frac{-237{,}000\frac{J}{mol}}{\left(\frac{2mole^-}{mol}\right)\left(\frac{96{,}485C}{mol}\right)} = +1.23\,V \qquad (1.8)$$

When the reaction is given as,

$$1A + bB \leftrightharpoons mM + nN \qquad (1.9)$$

The van't Hoff isotherm that tells how Gibbs free energy of the system changes as a function of the activity of reactants and products, is as follows,

$$\Delta\hat{g} = \Delta\hat{g}^0 + RT\ln\frac{a_M^m a_N^n}{a_A^1 a_B^b} \qquad (1.10)$$

Combining with equation (1.6) gives the Nernst equation,

$$E = E^0 - \frac{RT}{nF}\ln\frac{a_M^m a_N^n}{a_A^1 a_B^b} \qquad (1.11)$$

Applying this to the fuel cell reaction equation,

$$E = E^0 - \frac{RT}{2F}\ln\frac{1}{p_{H_2}p_{O_2}^{\frac{1}{2}}} = 1.254\,V \qquad (1.12)$$

, which means that we operate a room temperature H_2-O_2 fuel cell on 3 atm pure H_2 and 5 atm air, thermodynamics predicts a reversible cell voltage of 1.254 V.

1.3.2.2. SOFC performance

The electrochemical performance of SOFC is represented by a graph of the current-voltage characteristic (Figure 1-6). The shape is called the current-voltage (*i*-*V*) curve, which represents the voltage output according to the given current output. An ideal fuel cell would maintain a constant voltage regardless of current, which is thermodynamically determined. However, in a practical cell, it has a voltage output smaller than the ideal voltage value due to irreversible losses. The main factors of

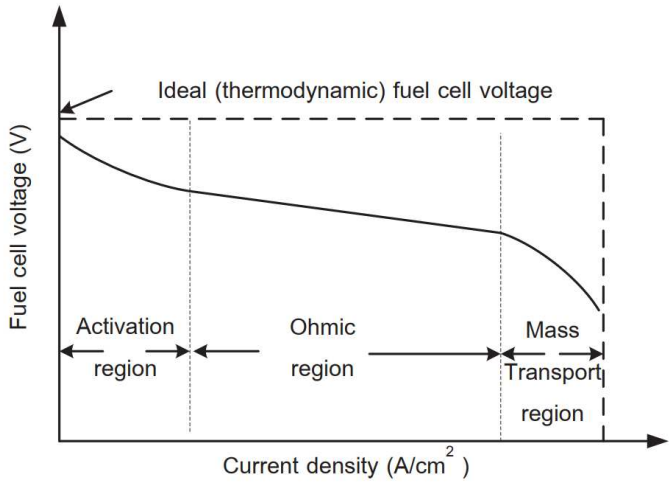

Figure 1-6 Schematic of fuel cell *i*-*V* curve.

ULSAN NATIONAL INSTITUTE OF SCIENCE AND TECHNOLOGY

the losses are activation losses (losses due to electrochemical reaction), ohmic losses (losses due to ionic and electronic conduction), and concentration losses (losses due to mass transport), which determine the characteristic shape of the fuel cell *i-V* curve.

1.3.2.2.1 Activation polarization

The electrochemical reaction involves a charge transfer reaction, which has an activation barrier. Activation polarization resulting from the barrier determines the reaction rate of charge transfer or surface exchange reaction at the electrode. This is because only species in the activated state can undergo a transition from reactant to product. The relationship between activation polarization and current density can be expressed by the following Butler-Volmer equation.

$$i = i_0[e^{\frac{(1-\alpha)nF\eta_{act}}{RT}} - e^{-\frac{-\alpha nF\eta_{act}}{RT}}] \quad (1.13)$$

where i is the current density, i_0 is the exchange current density, α is the charger transfer coefficient, and η_{act} is the activation polarization. One of the terms in the parentheses can be ignored for large values of η, and then the equation (1.13) can be described as the Tafel equation.

$$\eta_{act} = a \pm b\, logi \quad (1.14)$$

Parameters a and b are constants associated with the applied electrode material, electrode reaction type, and temperature.

1.3.2.2.2 Ohmic polarization

In SOFC, charge transfer occurs due to a voltage gradient, and this charge transfer process is known as conduction. Resistance corresponding to voltage loss used for conductive charge transport follows Ohm's law. The ohmic resistance can arise from electrodes, electrolytes, interconnects, etc., and is mainly dominated by electrolyte resistance. Resistance is scaled with the conductor's area A, thickness L, and conductivity σ: $R = L/\sigma A$. Therefore, the electrolyte should be as thin as possible and have high ionic conductivity.

1.3.2.2.3 Concentration polarization

Mass transport governs the supply and removal of reactants and products in SOFC. Poor mass transport can lead to loss of fuel cell performance due to reactant depletion (or product clogging). Various factors can lead to concentration loss: i) slow diffusion in the gas phase within the electrode pores, ii) slow diffusion of reactants/products at the electrolyte interface.

ULSAN NATIONAL INSTITUTE OF SCIENCE AND TECHNOLOGY

1.3.3. Materials for SOFC

1.3.3.1. Electrolyte materials

Electrolyte for SOFC has been mainly studied based on oxygen ion conductors, where current flow is generated by the movement of oxygen ions through the crystal lattice. This movement is achieved by hopping of thermally activated oxygen ions within the lattice, where oxygen defects in the crystal structure play a predominant role. Representative materials of electrolytes with such defects are as follows: ZrO_2-, CeO_2-, and Bi_2O_3-based oxides with fluorite structure, $LaGaO_3$-based perovskite, derivatives of $Bi_4V_2O_{11}$ and $La_2Mo_2O_9$, perovskite- and brownmillerite-like phases (*e.g.*, derived from $Ba_2In_2O_5$), pyrochlores, and $(Gd, Ca)_2Ti_2O_{7-\delta}$.[14]

1.3.3.2. Anode materials

The primary function of the anode in SOFC is to promote the electrochemical oxidation of fuel. When a hydrocarbon fuel such as methane is used as the fuel, the internal reforming or partial oxidation of the fuel is additionally accompanied in the anode. Electrochemical reactions often occur at interfaces or triple-phase boundaries (TPBs). In this case, the anode polarization that occurs in the electrode reaction is determined not only by intrinsic surface catalytic activities toward fuel oxidation, but also by the microstructure, morphology, and transport characteristics of the electrode material. Therefore, the general requirements for a SOFC anode material include good chemical and thermal stability, high electronic conductivity under fuel cell operating conditions, excellent catalytic activity toward the oxidation of fuels, manageable mismatch in coefficient of thermal expansion (TEC) with adjacent cell components, sufficient mechanical strength and flexibility, ease of fabrication into desired microstructures and low cost.[14]

The development of the Ni-YSZ cermet anode was groundbreaking in that Ni-YSZ meets most of the basic SOFC anode requirements. In the porous Ni-YSZ cermet anode, Ni metal provides electron conductivity and catalytic activity, while YSZ ceramic phase lowers the TEC of the anode, prevents the Ni phase from coarsening, and provides an oxygen ion conduction path to extend the active zone. Therefore, to date, Ni-YSZ cermet has been widely used as an anode material due to its high electrical conductivity, excellent catalytic activity for fuel oxidation, and low cost. The idea of a metal-ceramic cermet anode has also been used in the development of SOFCs using other electrolyte materials such as doped cria, $La_{1-x}Sr_xGa_{1-y}Mg_yO_3$ (LSGM), and proton-conducting electrolytes (*e.g.*, doped $BaCeO_3$-$BaZrO_3$). However, when hydrocarbons are directly used as fuel, the Ni-electrolyte cermet anode is easily deactivated by carbon coking or sulfur poisoning at the active site.[15], [16] Therefore, many alternative materials have been studied as the potential anode of SOFC.

For example, it has been reported that Cu-CeO_2-YSZ composite anodes have good carbon coking and sulfur tolerance, but Cu metal particles have low conductivity and low catalytic activity for

ULSAN NATIONAL INSTITUTE OF SCIENCE AND TECHNOLOGY

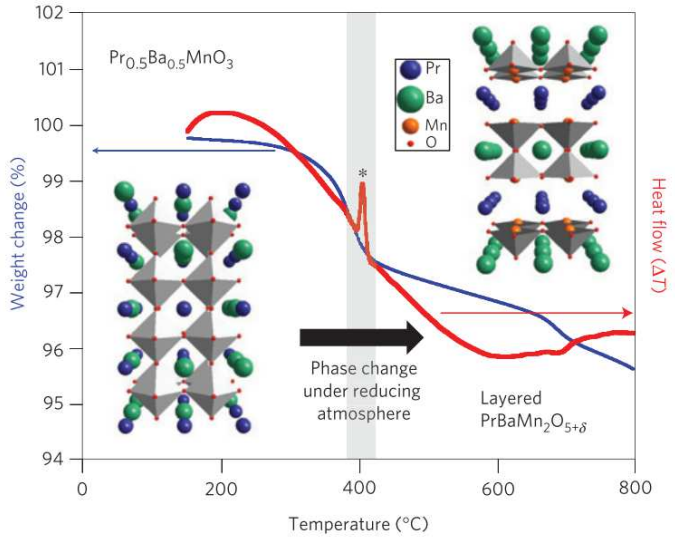

Figure 1-7 Principle of the approach to prepare A-site layered perovskite $PrBaMn_2O_{5+\delta}$. Phase change of Pr0.5Ba0.5MnO3 to layered $PrBaMn_2O_{5+\delta}$ Occurs under a reducing atmosphere. [22]

hydrocarbons.[17] To enhance the electrochemical performance, mixed oxygen-ion electron conductors (MIECs) have attracted considerable interest as alternative anode materials. In fact, several new materials have shown increased tolerance to sulfur poisoning and carbon deposition: Sr_2MgMoO_6 (SMMO)[18], $La_{0.8}Sr_{0.2}Sc_xMn_{1-x}O_{3-\delta}$[19], $La_{0.75}Sr_{0.25}Cr_{0.5}Mn_{0.5}O_3$ (LSCM)[20], $La_{0.33}Sr_{0.67}Ti_xMn_{1-x}O_{3-\delta}$[19], and $Pr_{0.8}Sr_{1.2}(Co,Fe)_{0.8}Nb_{0.2}O_4$ (K-PSCFN)[21]. Recently, Sengodan *et al.* reported $PrBaMn_2O_{5+\delta}$ (PBMO), a new perovskite with a layered double perovskite structure.[22] The layered PBMO anode showed very high electrical conductivity, excellent redox, coking tolerance, and sulfur tolerance. As shown in Figure 1-7, the layered perovskite has a stacking sequence of $[BaO]$-$[MnO_2]$-$[PrO_\delta]$-$[MnO_2]$. In this structure, since most of the oxygen vacancies are located in the PrO layer, a rapid oxygen ion channel is formed to ensure rapid oxygen ion diffusion. Besides, the conductivity of PBMO is 8.16 S cm^{-1} in 5 % H_2 atmosphere at 800 °C, which is higher than that of ceramic anodes previously published in SMMO (4.21 S cm^{-1}) and LSCM (0.96 S cm^{-1}).

1.4. Dry reforming of methane (DRM)

1.4.1. Overview

The dry reforming of methane (DRM) was first reported in 1888[23] and then further investigated by Fischer and Tropsch in 1928[24]. Today, DRM has been studied as a promising way to utilize methane and carbon dioxide at the same time by converting these to syngas (a mixture of H_2 and CO) which can be used as fuel or feedstock in the chemical industry.[25]–[27] Additionally, DRM is very suitable for the subsequent synthesis of long-chain hydrocarbons and oxygenate chemicals such as acetic acid, dimethyl ether, and oxo-alcohol in that it produces syngas with a high CO selectivity and a low H_2/CO ratio compared to other reforming reactions, which is also an advantage in responding to the oil crisis.

ULSAN NATIONAL INSTITUTE OF SCIENCE AND TECHNOLOGY

[25] Despite the economic and environmental advantages of DRM, it has not fully matured for industrial applications because of the deactivation of the conventional Ni-based catalysts from carbon coking and sintering during the reaction.[2], [28] Noble metals (Ir, Rh, Ru, Pt, and Pd) can be used in whole or in part to increase carbon resistance, but they are generally not economical.

To develop a highly active and stable catalyst for the DRM process, active metals, supports, promoters, morphologies, and preparation methods should be properly considered. For example, in the case of support (SiO_2 and Al_2O_3), it can provide a high surface area for the dispersion of active sites and play an auxiliary role in catalytic action. Therefore, the chemical and structural stability of the support at operating temperature and atmosphere is very important. As support, oxides with structures such as spinel, fluorite, Ruddlesden-Popper, and perovskite can be used. In the case of a promoter, it plays a role in improving the reactivity of the catalyst chemically by avoiding sintering of active metal particles or by adjusting basicity or redox property. The preparation methods for catalysts can also considerably influence their chemical properties and catalytic activity. The proper preparation method results in better dispersion of the catalyst, strong metal-support interaction, and higher surface area. In particular, the preparation of nanocatalysts for DRM through exsolution is highly preferred in recent studies because it can secure homogeneous high dispersion of active metal, strong interaction between metal supports, and small particle size.

1.4.2. Thermodynamics of DRM

DRM is an endothermic reaction that requires high temperatures to dissociate stable reactants, CH_4 and CO_2.

$$CH_4 + CO_2 \rightarrow 2CO + 2H_2, \ \Delta H_{298}^0 = 248\ kJ \cdot mol^{-1} \quad (1.15)$$

In an operating condition, possible side reactions may be involved during the DRM process. For example, reverse water gas shift (RWGS) reaction, steam reforming of methane (SRM), methane decomposition, and Boudouard reaction may occur simultaneously. In particular, the RWGS reaction may cause a higher CO_2 conversion than the CH_4 conversion at equilibrium and affect the H_2/CO ratio of the syngas produced.

$$CH_4 + H_2O \rightarrow CO + 3H_2, \ \Delta H_{298}^0 = 206\ kJ \cdot mol^{-1} \quad (1.16)$$

$$CO_2 + H_2 \rightarrow CO + H_2O, \ \Delta H_{298}^0 = 41\ kJ \cdot mol^{-1} \quad (1.17)$$

As routes of carbon formation, Boudouard reaction and methane decomposition reaction should be considered. In the DRM process, carbon formation can occur by CH_4 decomposition in equation (1.18) or Boudouard reaction in equation (1.19).

$$CH_4 \rightarrow C + 2H_2, \ \Delta H_{298}^0 = 75\ kJ \cdot mol^{-1} \quad (1.18)$$

$$2CO \rightarrow C + CO_2, \ \Delta H_{298}^0 = -172\ kJ \cdot mol^{-1} \quad (1.19)$$

ULSAN NATIONAL INSTITUTE OF
SCIENCE AND TECHNOLOGY

The CH_4 decomposition is an endothermic reaction, whereas the Boudouard reaction is exothermic, thus the CH_4 decomposition occurs above 557 ^oC and the Boudouard reaction can occur below 700 ^oC.[29] However, carbon generation is highly affected by the ratio of reactants (between CH_4 and CO_2), catalyst properties, GHSV, and the presence of dilution gas, so it is difficult to generalize the prediction of carbon generation simply by calculating thermodynamics.[25]

ULSAN NATIONAL INSTITUTE OF SCIENCE AND TECHNOLOGY

References

[1] McKinsey & Company, *Energy Insights* **2019**, 31.

[2] S. De, J. Zhang, R. Luque, N. Yan, *Energy Environ. Sci.* **2016**, *9*, 3314.

[3] P. Szuromi, *Science.* **2019**, *366*, 834.

[4] T. W. van Deelen, C. Hernández Mejía, K. P. de Jong, *Nat. Catal.* **2019**, *2*, 955.

[5] J. Hwang, R. R. Rao, L. Giordano, Y. Katayama, Y. Yu, Y. Shao-Horn, *Science.* **2017**, *358*, 751.

[6] B. Hua, M. Li, Y. F. Sun, J. H. Li, J. L. Luo, *ChemSusChem* **2017**, *10*, 3333.

[7] J. Zhang, M.-R. Gao, J.-L. Luo, *Chem. Mater.* **2020**, *32*, 5424.

[8] D. Neagu, T. S. Oh, D. N. Miller, H. Menard, S. M. Bukhari, S. R. Gamble, R. J. Gorte, J. M. Vohs, J. T. S. Irvine, *Nat Commun* **2015**, *6*, 8120.

[9] O. Kwon, S. Joo, S. Choi, S. Sengodan, G. Kim, *J. Phys. Energy* **2020**, *2*, 032001.

[10] D. Neagu, G. Tsekouras, D. N. Miller, H. Menard, J. T. S. Irvine, *Nat Chem* **2013**, *5*, 916.

[11] Y.-F. Sun, Y.-Q. Zhang, J. Chen, J.-H. Li, Y.-T. Zhu, Y.-M. Zeng, B. S. Amirkhiz, J. Li, B. Hua, J.-L. Luo, *Nano Lett.* **2016**, *16*, 5303.

[12] S. Joo, O. Kwon, K. Kim, S. Kim, H. Kim, J. Shin, H. Y. Jeong, S. Sengodan, J. W. Han, G. Kim, *Nat. Commun.* **2019**, *10*, 697.

[13] S. Joo, O. Kwon, S. Kim, H. Y. Jeong, G. Kim, *J. Electrochem. Soc.* **2020**, *167*, 064518.

[14] J. W. Fergus, H. Rob, L. Xianguo, D. P. Wilkinson, J. Zhang, *Solid Oxide Fuel Cells Materials Properties and Performance*, CRC Press, **2008**.

[15] a Atkinson, S. Barnett, R. J. Gorte, J. T. S. Irvine, a J. McEvoy, M. Mogensen, S. C. Singhal, J. Vohs, *Nat. Mater.* **2004**, *3*, 17.

[16] S. Sengodan, M. Liu, T.-H. Lim, J. Shin, M. Liu, G. Kim, *J. Electrochem. Soc.* **2014**, *161*, F668.

[17] Z. Cheng, J. H. Wang, Y. Choi, L. Yang, M. C. Lin, M. Liu, *Energy Environ. Sci.* **2011**, *4*, 4380.

[18] Y.-H. Huang, R. I. Dass, Z.-L. Xing, J. B. Goodenough, *Science.* **2006**, *2*, 254.

[19] G. Corre, G. Kim, M. Cassidy, J. M. Vohs, R. J. Gorte, J. T. S. Irvine, *Chem. Mater.* **2009**, *21*, 1077.

[20] S. Tao, J. T. S. Irvine, *Nat. Mater.* **2003**, *2*, 320.

[21] C. Yang, Z. Yang, C. Jin, G. Xiao, F. Chen, M. Han, *Adv. Mater.* **2012**, *24*, 1439.

[22] S. Sengodan, S. Choi, A. Jun, T. H. Shin, Y.-W. Ju, H. Y. Jeong, J. Shin, J. T. S. Irvine, G. Kim, *Nat. Mater.* **2014**, *14*, 205.

[23] Z. J. Lang, *Phys. Chem.* **1888**, *2*, 161.

[24] B. F. Fischer, H. Tropsch, *Chem* **1928**, *3*, 39.

[25] W. Jang, J. Shim, H. Kim, S. Yoo, H. Roh, *Catal. Today* **2019**, *324*, 15.

ULSAN NATIONAL INSTITUTE OF SCIENCE AND TECHNOLOGY

[26] Z. Bian, S. Das, M. H. Wai, P. Hongmanorom, S. Kawi, *ChemPhysChem* **2017**, *18*, 3117.

[27] S. Sengodan, R. Lan, J. Humphreys, D. Du, W. Xu, H. Wang, S. Tao, *Renew. Sustain. Energy Rev.* **2018**, *82*, 761.

[28] Z. Liu, D. C. Grinter, P. G. Lustemberg, T. D. Nguyen-Phan, Y. Zhou, S. Luo, I. Waluyo, E. J. Crumlin, D. J. Stacchiola, J. Zhou, J. Carrasco, H. F. Busnengo, M. V. Ganduglia-Pirovano, S. D. Senanayake, J. A. Rodriguez, *Angew. Chemie - Int. Ed.* **2016**, *55*, 7455.

[29] G. J. M. S. Wang, G.Q. Lu, *Energy Fuels* **1996**, *10*, 896.

[30] R. D. Shannon, *Acta Cryst.* **1976**, *A32*, 751.

[31] O. Kwon, S. Sengodan, K. Kim, G. Kim, H. Y. Jeong, J. Shin, Y.-W. Ju, J. W. Han, G. Kim, *Nat. Commun.* **2017**, *8*, 15967.

[32] "Atmospheric CO_2 concentration," can be found under https://sioweb.ucsd.edu/programs/keelingcurve/wp-content/plugins/sio-bluemoon/graphs/co2_10k.png, **n.d.**

[33] D. Neagu, V. Kyriakou, I. L. Roiban, M. Aouine, C. Tang, A. Caravaca, K. Kousi, I. Schreur-Piet, I. S. Metcalfe, P. Vernoux, M. C. M. Van De Sanden, M. N. Tsampas, *ACS Nano* **2019**, *13*, 12996.

ULSAN NATIONAL INSTITUTE OF SCIENCE AND TECHNOLOGY

Chapter 2 Investigation of a Layered Perovskite for IT-SOFC Cathodes: B-Site Fe-Doped $YBa_{0.5}Sr_{0.5}Co_{2-x}Fe_xO_{5+\delta}$

This chapter has been published.

Reproduced with permission from S. Joo, J. Kim, J. Shin, T.-H. Lim, G. Kim, J. Electrochem. Soc. 2016, 163, F1489.

2.1. Introduction

Solid oxide fuel cells (SOFCs) are regarded as promising energy conversion-storage systems because of high-energy conversion efficiency, efficient reclamation of waste heat, low pollutant emissions, and extensive fuel flexibility over other fuel cells.[1]-[3] However, even with these benefits, the high operating temperature (800-1000 ^{o}C) causes several problems, *e.g.*, expensive maintenance cost, material degradation, and material compatibility challenges.[4] Recent studies thus have focused on developing intermediate temperature SOFCs (IT-SOFCs) operating from 500 to 700 ^{o}C to minimize these issues. The lowered operating temperature, however, results in slow oxygen reduction kinetics and high over-potential at the cathode, consequently leading to inferior cell performance. The development of cathode materials with high electro-catalytic activity for the oxygen reduction reaction (ORR) at intermediate temperatures consequently has become an important goal in this area of research.[5]

In this respect, mixed ionic-electronic conducting (MIEC) cathodes have been widely investigated for application to intermediate-temperature solid oxide fuel cells (IT-SOFCs).[6] In particular, cobalt-based simple perovskites, for instance, $Ba_{0.5}Sr_{0.5}Co_{0.8}Fe_{0.2}O_{3-\delta}$[7], [8] and $La_{0.6}Sr_{0.4}Co_{0.2}Fe_{0.8}O_{3-\delta}$[9], have been proposed as MIEC cathode materials. Recently, double-perovskite (or layered perovskite) oxides, $LnBaCo_2O_{5+\delta}$ (Ln = Pr, Nd, Sm, and Gd), have been studied in efforts to exploit their fast oxygen kinetics, specifically oxygen diffusion and oxygen surface exchange. These materials can be structurally described with a stacking sequence of …[LnO_δ] - [CoO_2] - [BaO] - [CoO_2]… along the c-axis.[10], [11] This structure possesses a [LnO_δ] layer with reduced oxygen bonding strength providing a disorder-free channel for ion transport, resulting in an increase of the oxygen ion diffusivity.[12], [13]

In spite of these favorable oxygen kinetic properties of the cobalt-based cathode materials, there is a large gap in the thermal expansion behavior relative to electrolyte materials.[14], [15] The mismatch of the thermal expansion coefficient (TEC) between the electrode and the electrolyte can lead to delamination at the electrode/electrolyte interface due to the stress developed upon heating and cooling processes, leading to severe cell degradation.[16] This drawback can be minimized by introducing Y (Yttrium) into the Ln-site which decreases ionicity of the Y-O bonds because the stronger ionic bonds can account for the larger thermal expansion compared to weaker ionic bonds. A smaller TEC with

ULSAN NATIONAL INSTITUTE OF SCIENCE AND TECHNOLOGY

lower Ln-O bond ionicity has been observed with various $LnBaCo_2O_{5+\delta}$ (Ln = La, Nd, Sm, Gd, and Y) systems.[17] The TEC for the double-perovskite $YBaCo_2O_{5+\delta}$ is reported as 15.8×10^{-6} K^{-1} at temperatures between 80 and 900 ^oC in air, while other double-perovskite cathodes such as $LnBaCo_2O_{5+\delta}$ (Ln = Gd, Sm, Nd, and La) have higher TECs of $16.6 \sim 24.3 \times 10^{-6}$ K^{-1} under the same conditions,[17] indicating that the double-perovskite $YBaCo_2O_{5+\delta}$ has a closer TEC to that of $Ce_{0.9}Gd_{0.1}O_{2-\delta}$ (GDC) electrolyte (*e.g.*, 12.5×10^{-6} K^{-1}.[18]).

However, double-perovskite $YBaCo_2O_{5+\delta}$ still suffers from phase instability. In particular, it showed several XRD reflections from decomposition as a result of sintering temperature above 800 ^oC in air. This phase instability may be resulted from less bound Y^{3+} cations under a large amount of oxygen vacancies in the Ln-O layer due to the tendency to have low oxygen coordination numbers compared to those of large Ln^{3+}.[19] Regarding the stability issue, Sr substitution for Ba has been investigated as an effective way to enhance the stability by controlling the oxygen content in $YBaCo_2O_{5+\delta}$.[19]-[21]

In this context, we assume that transition metal doping into Co on the B-site could also increase the oxygen content leading to enhance structural integrity. Many groups have previously researched the effect of Fe substitution on the structure and properties of $LnBaCo_{2-x}Fe_xO_{5+\delta}$, where the oxygen content is proportional to the amount of Fe.[13], [22], [23] Based on these findings, we present here $YBa_{0.5}Sr_{0.5}Co_{2-x}Fe_xO_{5+\delta}$ (x = 0, 0.25, 0.5, and 0.75) for the first time with the aims of stabilizing structural properties, reducing the TEC, and maximizing electrochemical properties for application as an IT-SOFC cathode.

2.2. Experimental

2.2.1. Synthesis of powders and bars

Cathode materials $YBa_{0.5}Sr_{0.5}Co_{2-x}Fe_xO_{5+\delta}$ (YBSC(F)s) (x = 0, 0.25, 0.5, and 0.75) were synthesized by the Pechini method. The required amounts of $Y(NO_3)_3 \cdot 6H_2O$ (Adrich, 99.9%), $Ba(NO_3)_2$ (Aldrich, 99+%), $Sr(NO_3)_2$ (Adrich, 99+%), $Co(NO_3)_2 \cdot 6H_2O$ (Adrich, 98+%), and $Fe(NO_3)_3 \cdot 9H_2O$ (Aldrich, 98+%) were dissolved in distilled water. After that, citric acid and ethylene glycol (mole ratio of metal cations : citric acid : ethylene glycol = 1 : 1.2 : 1.5) were added into the solution as heterogeneous agents under continuous stirring and the solution was heated to 250 ^oC for combustion. The resultant powders were pre-calcined at 600 ^oC for 4 h and then ball-milled in acetone for 24 h. The calcined powders were dry-pressed into pellets at 5 MPa and sintered at 1150 ^oC for 12 h ~ 24 h in air (to achieve relative density > 92%) for the measurement of XRD, electrical conductivity, iodometric titration, and dilatometry. For preparation of anode support materials, $Ce_{0.9}Gd_{0.1}O_{2-\delta}$ (GDC) and NiO were synthesized by glycine-nitrate process (GNP). For preparation of cathode slurries, the pre-calcined YBSC(F)s, GDC, and an organic binder (Heraeus V006) were blended (at a weight ratio of 6 : 4 : 12).

ULSAN NATIONAL INSTITUTE OF SCIENCE AND TECHNOLOGY

2.2.2. Fabrication of cells

For impedance spectroscopy, symmetric cells of electrode | GDC | electrode were fabricated. GDC pellet with thickness of ~1 mm was sintered at 1350 ^{o}C for 4 hours in air and polished to 0.65 mm. Cathode slurries were then screen-printed onto both sides of the dense GDC electrolyte with an active electrode area of 0.36 cm^2 each and sintered at 950 ^{o}C for 4 hours in air.

In order to determine electrochemical performance of cathode, anode-supported single cells with a configuration of Ni-GDC | GDC | cathode were prepared using a drop-coating method. For preparation of Ni-GDC anode support, NiO , GDC, and starch at a weight ratio of 6 : 4 : 1.5 were ball-milled in ethanol for 24 hours. The dried NiO-GDC mixture was then pelletized (~0.6 mm thick and 15mm diameter). A GDC suspension for drop-coating was prepared by dispersing GDC powders (Aldrich) in ethanol with proper amount of binder (polyvinyl Butyral, B-98) and dispersant (Triethanolamine, Alfa Aesar) at a ratio of 1 : 10. The GDC suspension was then drop-coated to a Ni-GDC anode support, followed by drying in air and subsequent co-sintering at 1400 ^{o}C for 5 hours. Cathode slurries are screen-printed on the GDC electrolyte with active cathode area of 0.36 cm^2.

2.2.3. Characterization of cathodes

A four-electrode measurement is used for the YBSC(F)s cathodes in order to measure electrical conductivities in air. Rectangular samples for conductivity measurement were prepared from sintered pellets. Ag wire were attached to the sample end surfaces, which were fixed with Ag paste. A constant current of 100 mA was applied to sample and the voltage difference was measured using a potentiostat (BioLogic) in a temperature range of 100 to 750 ^{o}C with an interval of 50 ^{o}C.

For the symmetric and single cell measurement, Ag wires were attached to the two electrodes each using Ag paste. The cells were fixed on the end of an alumina tube using a ceramic adhesive (Aremco, Ceramabond 552).

In order to evaluate the electrocatalytic activity of cathode, impedance spectra for symmetric cells were measured under OCV in a frequency range of 1 mHz to 500 kHz with 10 mV AC perturbation in a temperature range of 500-650 ^{o}C.

For the single cell test, H_2 with 3 vol % H_2O was supplied to anode as the fuel at a flow rate of 100 mL min^{-1}, whereas air was supplied to cathode. Impedance spectra and I-V polarization curves were measured using a BioLogic Potentiostat in a temperature range of 500-650 ^{o}C.

The crystalline structures were examined by an X-ray powder diffraction (XRD) (Bruker, D8 Advance, Cu Ka radiation) analysis. The *in situ* XRD was also carried out in the temperature range of 100 ^{o}C to the operating temperature (Bruker, D8 Advance). The microstructures and morphologies of YBSC(F)s samples were probed using a field emission scanning electron microscope (SEM) (Nova SEM). A thermogravimetric analysis (TGA) was carried out using a SDT-Q600 (TA Instrument, USA) in a temperature range from 100 ^{o}C to 900 ^{o}C with a heating/cooling rate of 2 ^{o}C min^{-1} in air. The initial

ULSAN NATIONAL INSTITUTE OF
SCIENCE AND TECHNOLOGY

oxygen content (at room temperature) were determined by iodometric titration. Dilatometry (DIL-402C) was used to determine the TEC of samples in a temperature range of 100-800 ^{o}C under ambient air.

ULSAN NATIONAL INSTITUTE OF SCIENCE AND TECHNOLOGY

2.3. Result and discussion

2.3.1. XRD

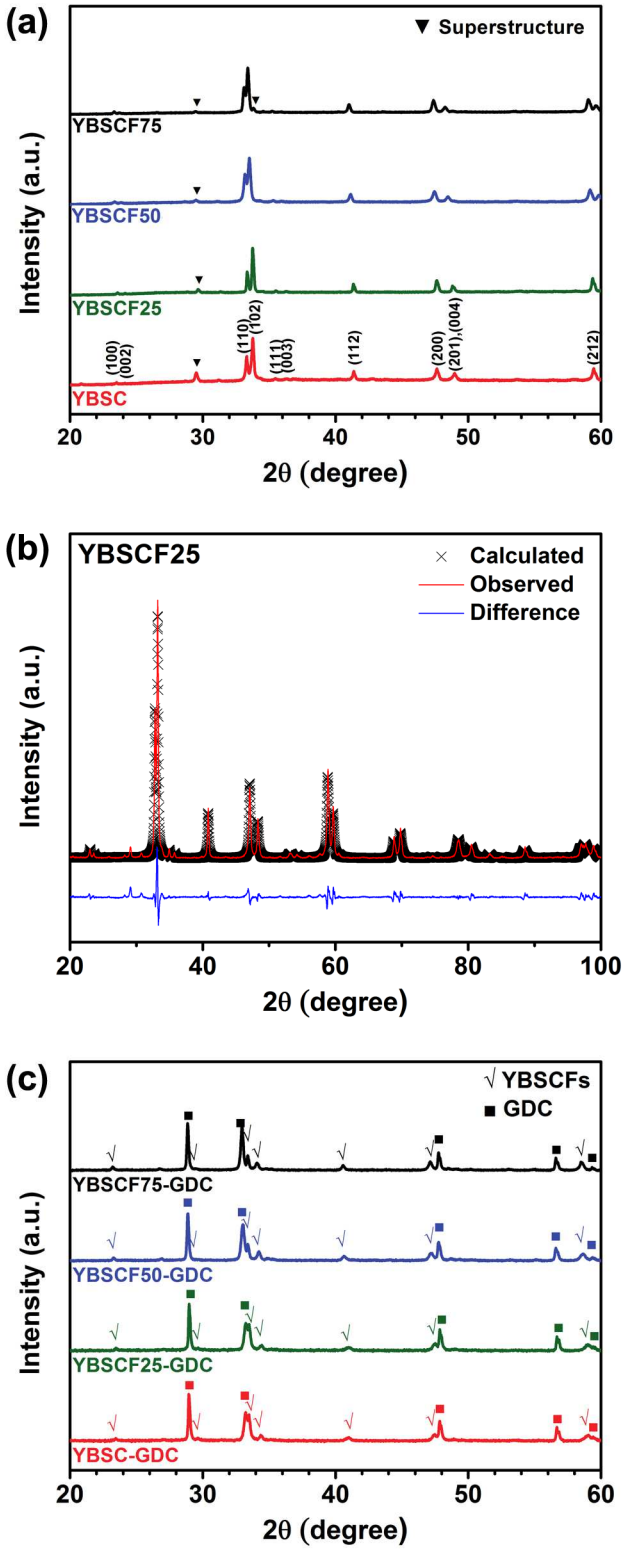

Figure 2-1 (a) X-ray diffraction patterns of YBSC(F)s powders sintered at 1150◦C for 12 h in air. (b) Observed and calculated XRD profiles and the difference between them for YBSCF25. (c) XRD patterns of YBSC(F)s and GDC mixture sintered at 950◦C for 4 h in air.

ULSAN NATIONAL INSTITUTE OF SCIENCE AND TECHNOLOGY

Table 2-1 Abbreviations of specimens

Chemical composition	Abbreviations
$Ce_{0.9}Gd_{0.1}O_{2-\delta}$	GDC
$YBa_{0.5}Sr_{0.5}Co_2O_{5+\delta}$	YBSC
$YBa_{0.5}Sr_{0.5}Co_{1.75}Fe_{0.25}O_{5+\delta}$	YBSCF25
$YBa_{0.5}Sr_{0.5}Co_{1.5}Fe_{0.5}O_{5+\delta}$	YBSCF50
$YBa_{0.5}Sr_{0.5}Co_{1.25}Fe_{0.75}O_{5+\delta}$	YBSCF75

Table 2-2 Space group and structure parameters of YBSC(F)s

Chemical composition	Space group	a (Å)	b (Å)	c (Å)	Volume (Å^3)
YBSC	*P4/mmm*	3.8528	3.8528	7.4950	111.25
YBSCF25	*P4/mmm*	3.8584	3.8584	7.5326	112.14
YBSCF50	*P4/mmm*	3.8585	3.8585	7.5607	112.56
YBSCF75	*P4/mmm*	3.8638	3.8638	7.5848	113.23

X-ray diffraction (XRD) patterns of $YBa_{0.5}Sr_{0.5}Co_{2-x}Fe_xO_{5+\delta}$ (x = 0, 0.25, 0.5, and 0.75) are shown in Figure 2-1 (a). The abbreviations used to identify the various samples are given in Table 2-1. All of the YBSC(F)s are identified as single-phase double-perovskites without any impurity phases. With increasing the amount of Fe, lattice parameters are increased due to the substitution of the larger Fe^{3+} and Fe^{4+} ions into the smaller Co^{3+} and Co^{4+} ions.[23] Figure 2-1 (b) shows the Rietveld refinement data of YBSCF25, presenting good agreement between the observed and calculated profiles. As summarized in Table 2, the Rietveld refinement data show that all the YBSC(F)s crystallize in the tetragonal space group, *P4/mmm*.

In general, the undesired insulating layer caused by the interfacial reaction between an electrode and electrolyte can obstruct the oxide-ionic and electronic transport.[24] Kim *et al.* reported that a $YBaCo_2O_{5+\delta}$ cathode had an interfacial reactivity with $La_{0.8}Sr_{0.2}Ga_{0.8}Mg_{0.2}O_{2.8}$ (LSGM) electrolyte after being heated at 1000 ^oC for 3 h.[17] In this study, $Gd_{0.1}Ce_{0.9}O_{2-\delta}$ (GDC) is selected as an electrolyte

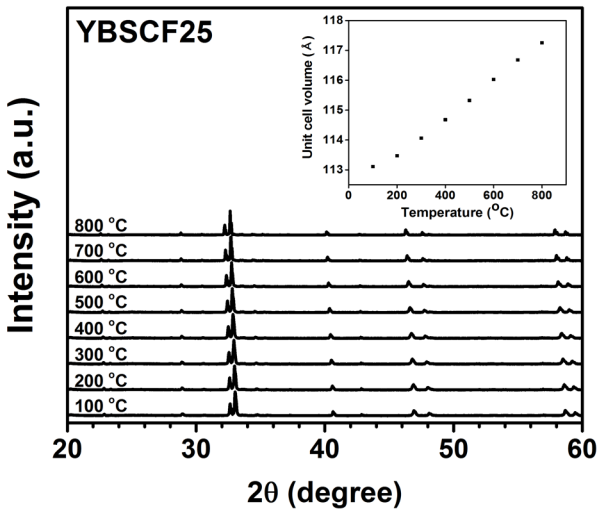

Figure 2-2 The *in situ* XRD patterns of $YBa_{0.5}Sr_{0.5}Co_{1.75}Fe_{0.25}O_{5+\delta}$ (YBSCF25) at various temperatures. The inset shows the dependence of temperature on unit cell volume V (Å^3).

ULSAN NATIONAL INSTITUTE OF SCIENCE AND TECHNOLOGY

because of the absence of interfacial reactions between it and YBSC(F)s cathodes. To examine the chemical compatibility, the XRD patterns of the YBSC(F)s-GDC composite (7:3 weight ratio) after heat treatment at 950 °C for 4 h were evaluated and the results are shown in Figure 2-1 (c). From the patterns, there are no observed interfacial reactions or apparent secondary phases between them.

Table 2-3 Comparison of thermal expansion coefficient of YBSC(F)s between via *in situ* XRD and dilatometry

Chemical composition	TEC via *in situ* XRD (10^{-6} K^{-1})	TEC via dilatometry (10^{-6} K^{-1})
YBSC	17.31	17.61
YBSCF25	17.89	17.69
YBSCF50	18.00	18.14
YBSCF75	18.14	18.16

The phase stability of YBSC(F)s under the operating conditions of a SOFC cathode is confirmed via *in situ* X-ray diffraction measurements in a temperature range of 100-800 °C under ambient air. As shown in Figure 2-2, YBSCF25 shows no chemical or structural changes upon heating, demonstrating thermal stability under the operating conditions. The main peaks are lower-angle shifted as the temperature

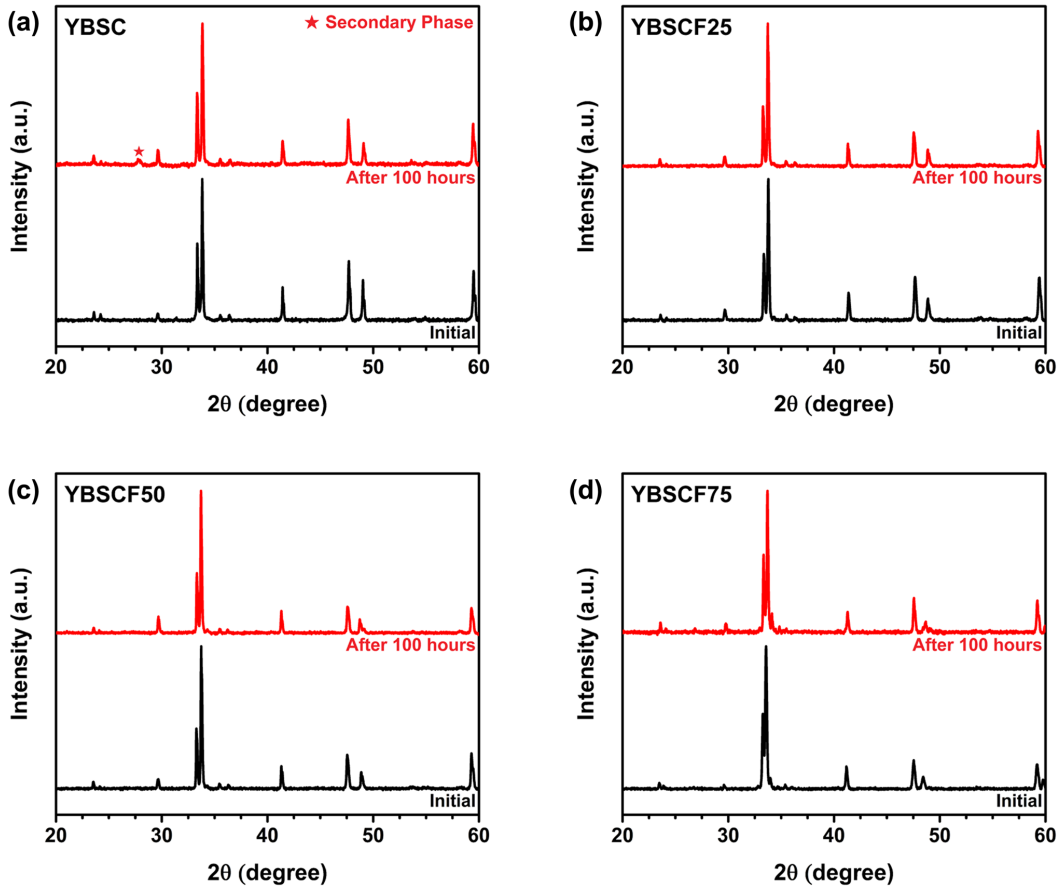

Figure 2-3 X-ray diffraction patterns for the cathode powders re-annealed at 700 °C in ambient air: (a) YBSC, (b) YBSCF25, (c) YBSCF50, and (d) YBSCF75.

ULSAN NATIONAL INSTITUTE OF SCIENCE AND TECHNOLOGY

increases, implying that the volume of unit cells increases due to the larger size of B-site cations after reduction, as shown in the inset of Figure 2-2. It can be interpreted that the reduction of Co^{4+} to Co^{3+} caused by a loss of oxygen gives rise to high TECs due to the larger ionic size of Co^{3+} relative to that of Co^{4+}.

The thermal expansion coefficient (TEC) calculated from *in situ* X-ray diffraction of YBSC(F)s increases with the amount of Fe, which is in accordance with the dilatometry data in Table 2-3. The effect of Fe doping can be ascribed to the increase of the average ionic radius of B-site ions leading to high TECs[25] due to the larger ionic radius of the doped Fe ($r_{Fe^{3+}}$= 0.785 Å, coordination number = 6, and high spin state) compared to that of Co ($r_{Co^{3+}}$= 0.75 Å, coordination number = 6, and high spin state)[30].

In order to assess the structural stability of the YBSC(F)s under practical operating conditions, all sintered samples were exposed to 700 ^{o}C for 100 hrs under ambient air. The samples were then identified by XRD, as shown in Figure 2-3. The formation of a secondary phase (marked with ★) is observed only for the re-annealed YBSC, which is identified as BaO (JCPDS#01-0746). On the other hand, no additional phase is identified from the re-annealed YBSCF25, YBSCF50, and YBSCF75, suggesting that Fe replacement for Co effectively enhances the structure stability of YBSC. This can be described by the increasing oxygen content in the Y-O layer with the amount of Fe content.[19]

2.3.2. SEM

Scanning electron microscopy (SEM) was performed to probe the microstructure of YBSC(F)s-GDC composites after screen printing on the GDC electrolyte at 950 ^{o}C. Figure 2-4 depicts a cross-sectional

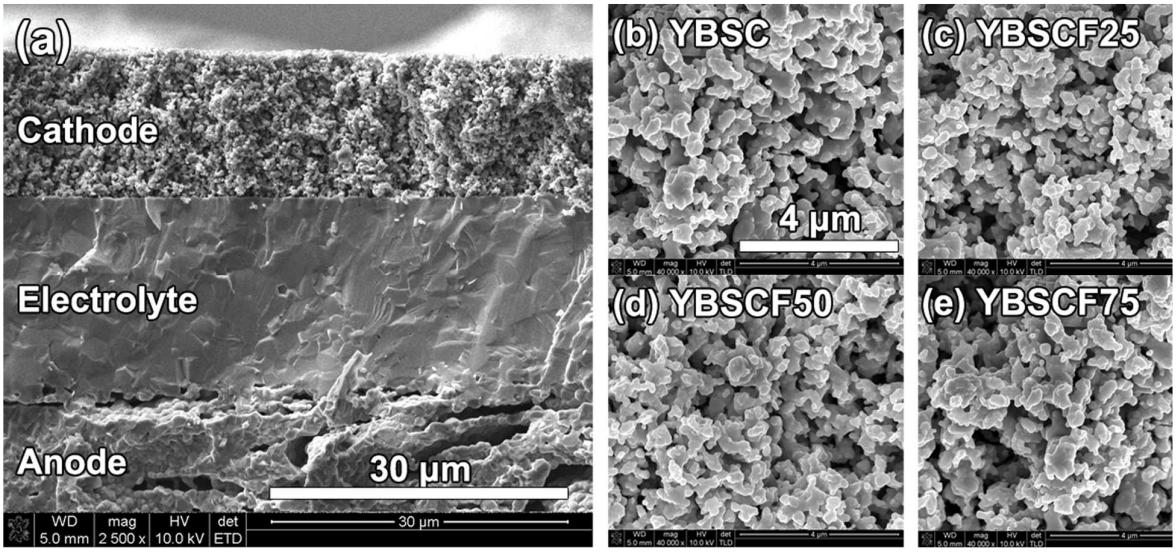

Figure 2-4 Scanning electron microscopy images of YBSC(F)s-GDC cathodes; (a) a cross-section consisting of the dense GDC electrolyte with the porous YBSCF25-GDC composite cathode and Ni-GDC anode; (b)-(f) microstructure of YBSC(F)s-GDC cathodes fabricated using screen printing followed by sintering at 950 ^{o}C for 4 hours.

ULSAN NATIONAL INSTITUTE OF
SCIENCE AND TECHNOLOGY

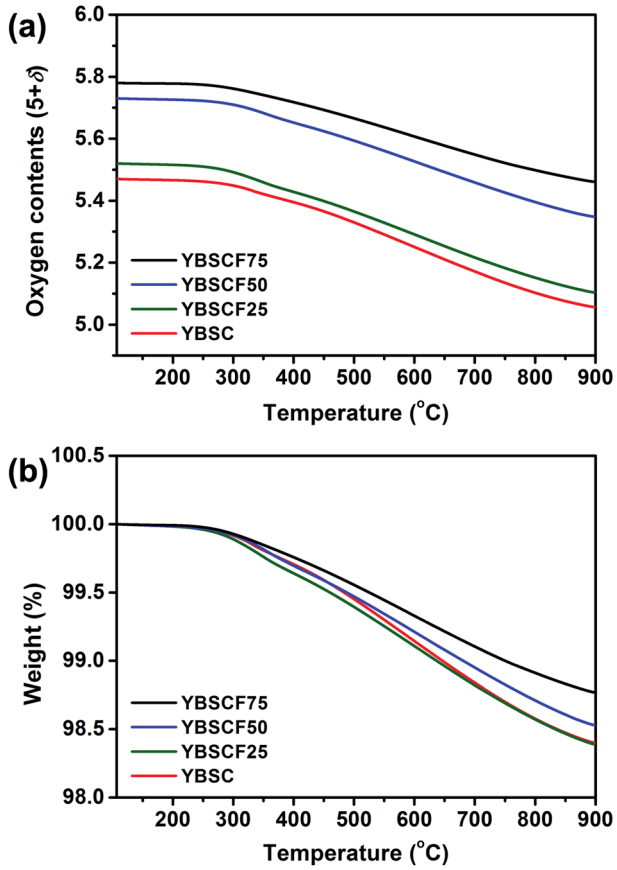

Figure 2-5 (a) Variation of oxygen content in YBSC(F)s and (b) the variation in oxygen loss (%) with temperature in air.

SEM image of YBSCF25-GDC|GDC|Ni-GDC with an overview of the three layers, indicating that the porous cathode (15 μm) and dense electrolyte (20 μm) appear adhered well. The electrolyte is fine and dense without any pores or cracks. As depicted in Figure 2-4 (b)-(e), the detailed microstructures of the porous YBSC(F)-GDC cathodes are similar, and the particle size seems to be insensitive to the amount of Fe substitution.

2.3.3. TGA

Figure 2-5 (a) presents the temperature dependence of the oxygen nonstoichiometry for YBSC(F)s, determined by a thermogravimetric analysis (TGA) from 100 to 900 °C in air. The initial oxygen content is determined from iodometric titration and the YBSC(F)s start to lose oxygen above 300 °C. The data in Figure 2-5 (b) reveal that the extent of oxygen loss decreases with increasing Fe content, which is described by the stronger Fe-O bond restraining the oxygen loss upon heating, compared to the Co-O bond.[27]

ULSAN NATIONAL INSTITUTE OF SCIENCE AND TECHNOLOGY

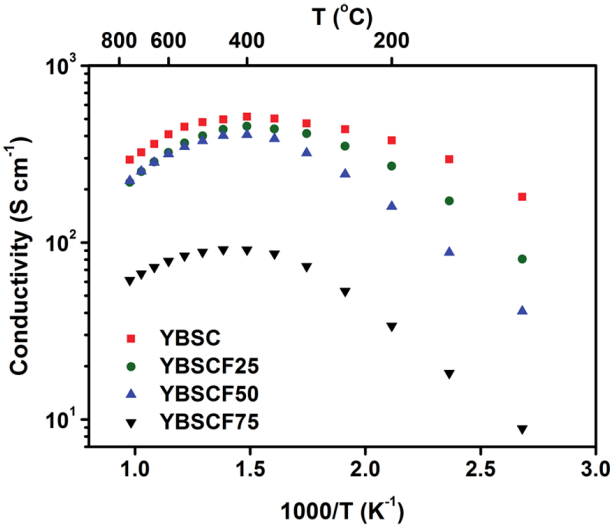

Figure 2-6 Electrical conductivities of YBSC(F)s in a temperature range 100-750 ºC in air.

2.3.4. Electrical conductivity

The temperature dependence of the electrical conductivity of YBSC(F)s in air is presented by an Arrhenius plot in Figure 2-6. The sudden decrease in the conductivity of YBSC(F)s above 400 °C is characteristic of a metal-insulator (M-I) transition accompanied by the low-spin to high-spin transition of Co^{3+} ions.[28], [29] Above the M-I transition temperature, 400 °C, the electrical conductivity decreases due to the increasing loss of oxygen content. This might originate from the decreased concentration of oxygen, which can be described by the predominant defect according to the following pseudo-chemical reaction:[30]

$$\frac{1}{2}O_2 + V_O^{\cdot\cdot} + Co_{Co}^{x} \leftrightarrow O_O^{x} + 2Co_{Co}^{\cdot}$$

This gives the following equation to maintain the electroneutrality:

$[V_O^{\cdot\cdot}] = 2[Co_{Co}^{\cdot}]$

Therefore, the decrease in the oxygen content via increasing temperature gives rise to a decrease in electronic holes, which is associated with the electronic conductivity of the samples.

At a given temperature, the electrical conductivity decreases with increasing Fe content in YBSC(F)s. This is attributed to the decreased covalency of the Fe^{4+}-O bond compared to the Co^{4+}-O bond resulting

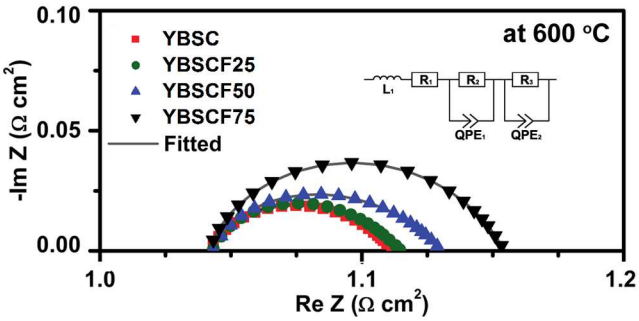

Figure 2-7 Impedance spectra of the YBSC(F)s-GDC composite on the GDC electrolyte in a symmetric cell measured under OCV conditions.

ULSAN NATIONAL INSTITUTE OF SCIENCE AND TECHNOLOGY

in an increase of electron localization and a decrease of electrical conductivity with increasing Fe content.[23], [31] The electrical conductivities of all samples are within a range of 408-78 S/cm at 600 °C, which is adequate for their use as cathodes in SOFCs.

Table 2-4 Electrochemical impedance spectroscopy fitting results of YBSC(F)s-GDC measured at 600 °C in air

Composition	R_1 (Ω cm^2)	R_2 (Ω cm^2)	R_3 (Ω cm^2)	R_p (Ω cm^2)
YBSC	1.0425	0.0767	0.0003	0.0770
YBSCF25	1.0767	0.0774	0.0006	0.0780
YBSCF50	0.9668	0.0990	0.0009	0.0999
YBSCF75	1.0115	0.1174	0.0017	0.1191

Table 2-5 ASR comparision in composite system at 600 °C

Chemical composition	ASR values (Ω cm^2)
YBSCF25-GDC (in this work)	0.077 (40 wt% GDC)
$La_{0.6}Sr_{0.4}Co_{0.2}Fe_{0.8}O_3$-GDC[32]	0.105 (60 wt% GDC)
$Sm_{0.5}Sr_{0.5}CoO_3$-$Sm_{0.2}Ce_{0.8}O_{1.9}$ (SDC)[33]	0.180 (30 wt% SDC)

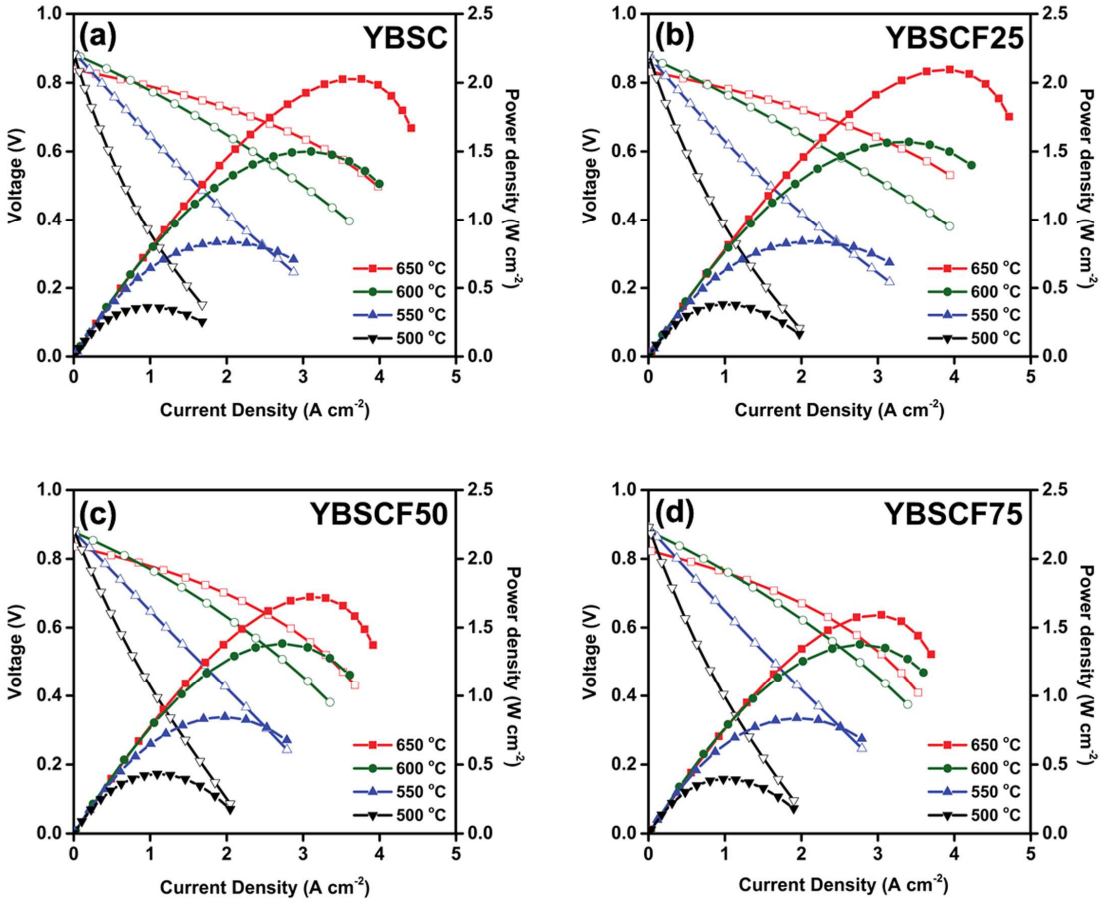

Figure 2-8 *I-V* curves and the corresponding power density curves of a single cell for (a) YBSC-GDC, (b) YBSCF25-GDC, (c) YBSCF50-GDC, and (d) YBSCF75-GDC composite cathodes at various temperatures.

ULSAN NATIONAL INSTITUTE OF
SCIENCE AND TECHNOLOGY

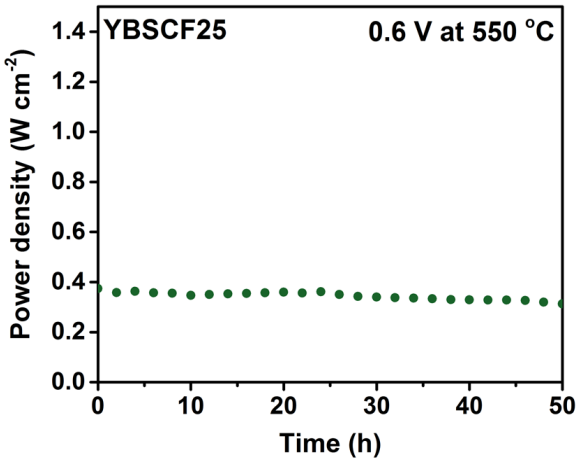

Figure 2-9 Long term cell stability result for YBSCF25-GDC under a constant voltage of 0.6 V at 550 ºC.

2.3.5. ASR

The ASRs of YBSC(F)s-GDC are obtained by alternating current (AC) impedance spectroscopy to determine the electrocatalytic activity of cathode for ORR. The impedance curves were fitted with an equivalent circuit, as shown in Figure 2-7. In this diagram, the intercept with the real axis at high frequency corresponds to ohmic resistance (R_1), consisting of the resistances from the electrolyte, electrodes, and current collectors (mainly originated from electrolyte). According to the previous interpretation, the electrode response consists of two main contributions at high frequency and low frequency.[34] The contribution at high frequency corresponds to R_2, which involves charge transfer process, including the migration and diffusion of oxygen ions from the triple-phase boundary (TPB) into the electrolyte. The contribution at low frequency (R_3), on the other hand, is associated with non-charge transfer processes including oxygen surface exchange, solid-state diffusion, and gas-phase diffusion.

The polarization resistance (R_p) of the cathode materials is defined by the sum of R_2 and R_3. The values of R_p are increased with the amount of Fe as summarized in Table 4. In detail, most of the total cell impedance comes from R_2, implying that the process of charge transfer is a key factor for the oxygen reduction reaction in YBSC(F)s cathode, which is in agreement with the results of a previous study.[20] As summarized in Table 5, the minimum ASR value is about 0.077 $\Omega \cdot cm^2$ at 600 ^oC for x = 0 and 0.25, which is substantially lower than the values presented in previous reports.[19], [20], [22], [32], [33]

2.3.6. Single cell performance

The cell performance of the YBSC(F)s-GDC cathodes in SOFCs is measured using Ni-GDC/GDC/cathode cells with humidified H_2 (3% H_2O) as a fuel and ambient air as an oxidant in a temperature range of 500-650 ^oC. Figure 2-8 shows that the OCV values are approximately 0.83V at

ULSAN NATIONAL INSTITUTE OF SCIENCE AND TECHNOLOGY

650 ^{o}C and increase with decreasing operating temperature. As expected from the ASR results, YBSCF25 shows the best cell performance, ~1.5 W cm^{-2} at 600 ^{o}C, and then the cell performance is reduced for x = 0.5 and 0.75.

Moreover, as presented in Figure 2-9, the long-term cell stability of YBSCF25-GDC cathode using the same cell configuration and gas for single cell was evaluated under a constant voltage of 0.6 V at 550 ^{o}C, showing its moderate cell stability with a power density of 0.36 W cm^{-2} over 50 h.

In conclusion, YBSCF25 is regarded as a promising cathode material for IT-SOFCs with Fe substitution in YBSC because of the enhanced structural stability, sufficient electrical properties and excellent electrochemical performance.

2.4. Conclusions

We investigated new layered perovskite oxides $YBa_{0.5}Sr_{0.5}Co_{2-x}Fe_xO_{5+\delta}$ (x = 0, 0.25, 0.5, and 0.75) by analyzing their structural properties, thermal expansion coefficient (TEC), electrical properties, and electrochemical performance for application to an IT-SOFC cathode. The XRD spectra demonstrate that all samples are chemically compatible with the GDC electrolyte. The Fe-doped YBSCs exhibit enhanced structural stability compared to the YBSC under practical operating conditions. This is ascribed to the higher amount of oxygen in the Y-O layer with Fe doping. The electrical conductivities are also suitable under actual operating conditions for all YBSC(F)s. Further, remarkable power density of 1.5 W cm^{-2} for x = 0.25 at 600 ^{o}C is also demonstrated. Considering the reduced TEC with YBSC(F)s, enhanced structural stability, and achieved power density, the x = 0.25 sample represents an optimum composition in YBSC(F)s system for use as a cathode in intermediate temperature SOFCs.

ULSAN NATIONAL INSTITUTE OF SCIENCE AND TECHNOLOGY

References

[1] S. Sengodan, S. Choi, A. Jun, T. H. Shin, Y.-W. Ju, H. Y. Jeong, J. Shin, J. T. S. Irvine, G. Kim, Nat. Mater. **2014**, 14, 205.

[2] A. Jun, S. Yoo, Y.-W. Ju, J. Hyodo, S. Choi, H. Y. Jeong, J. Shin, T. Ishihara, T. Lim, G. Kim, J. Mater. Chem. A **2015**, 3, 15082.

[3] M. D. Gross, J. M. Vohs, R. J. Gorte, J. Mater. Chem. **2007**, 17, 3071.

[4] B. C. Steele, A. Heinzel, Nature **2001**, 414, 345.

[5] S. Yoo, A. Jun, Y. Ju, D. Odkhuu, J. Hyodo, H. Y. Jeong, N. Park, J. Shin, T. Ishihara, G. Kim, Angew. Chemie Int. Ed. **2014**, 53, 13064.

[6] W. Jung, K. L. Gu, Y. Choi, S. M. Haile, Energy Environ. Sci. **2014**, 7, 1685.

[7] Y. Bu, Q. Zhong, D.-C. Chen, Y. Chen, S. Y. Lai, T. Wei, H. Sun, D. Ding, M. Liu, J. Power Sources **2016**, 319, 178.

[8] Z. Shao, S. M. Haile, Nature **2004**, 431, 170.

[9] V. Dusastre, J. A. Kilner, Solid State Ionics **1999**, 126, 163.

[10] G. Kim, S. Wang, A. J. Jacobson, L. Reimus, P. Brodersen, C. A. Mims, J. Mater. Chem. **2007**, 17, 2500.

[11] G. Kim, S. Wang, A. J. Jacobson, Z. Yuan, W. Donner, C. L. Chen, L. Reimus, P. Brodersen, C. A. Mims, Appl. Phys. Lett. **2006**, 88, 024103.

[12] A. A. Taskin, A. N. Lavrov, Y. Ando, Appl. Phys. Lett. **2005**, 86, 1.

[13] S. Choi, S. Yoo, J. Kim, S. Park, A. Jun, S. Sengodan, J. Kim, J. Shin, H. Y. Jeong, Y. Choi, G. Kim, M. Liu, Sci. Rep. **2013**, 3, 2426.

[14] A. Jun, J. Kim, J. Shin, G. Kim, ChemElectroChem **2016**, 3, 511.

[15] A. Jun, J. Shin, G. Kim, Phys. Chem. Chem. Phys. **2013**, 15, 19906.

[16] J. Kim, S. Choi, S. Park, C. Kim, J. Shin, G. Kim, Electrochim. Acta **2013**, 112, 712.

[17] J. H. Kim, A. Manthiram, J. Electrochem. Soc. **2008**, 155, B385.

[18] B. C. H. Steele, Solid State Ionics **1995**, 75, 157.

[19] J. H. Kim, Y. N. Kim, Z. Bi, A. Manthiram, M. P. Paranthaman, A. Huq, Solid State Ionics **2013**, 253, 81.

[20] F. Meng, T. Xia, J. Wang, Z. Shi, J. Lian, H. Zhao, J.-M. Bassat, J.-C. Grenier, Int. J. Hydrogen Energy **2014**, 39, 4531.

[21] G. Aurelio, R. D. Sánchez, J. Curiale, G. J. Cuello, J. Phys. Condens. Matter **2010**, 22, 486001.

[22] J. Xue, Y. Shen, T. He, J. Power Sources **2011**, 196, 3729.

[23] Y. N. Kim, J. H. Kim, A. Manthiram, J. Power Sources **2010**, 195, 6411.

[24] C. Rossignol, J. M. Ralph, J. M. Bae, J. T. Vaughey, Solid State Ionics **2004**, 175, 59.

[25] M. Mori, N. M. Sammes, Solid State Ionics **2002**, 146, 301.

ULSAN NATIONAL INSTITUTE OF
SCIENCE AND TECHNOLOGY

[26] R. D. Shannon, Acta Cryst. **1976**, A32, 751.

[27] S. Park, S. Choi, J. Kim, J. Shin, G. Kim, ECS Electrochem. Lett. **2012**, 1, F29.

[28] K. T. Lee, A. Manthiram, J. Electrochem. Soc. **2006**, 153, A794.

[29] Y. Moritomo, M. Takeo, X. Liu, T. Akimoto, A. Nakamura, Phys. Rev. B **1998**, 58, R13334.

[30] S. Park, S. Choi, J. Shin, G. Kim, Electrochim. Acta **2014**, 125, 683.

[31] S. Choi, J. Shin, G. Kim, J. Power Sources **2012**, 201, 10.

[32] S. B. Adler, J. A. Lane, B. C. H. Steele, J. Electrochem. Soc **1996**, 143, 3554.

[33] Y. Leng, S. H. Chan, Q. Liu, Int. J. Hydrogen Energy **2008**, 33, 3808.

[34] C. Xia, W. Rauch, F. Chen, M. Liu, Solid State Ionics **2002**, 149, 11.

ULSAN NATIONAL INSTITUTE OF SCIENCE AND TECHNOLOGY

Chapter 3 Cation Swapped Homogeneous Nanoparticles in Perovskite Oxides for Highly-efficient Power Density

This chapter has been published and has been cited in the thesis by co-author O. Kwon.

Reproduced with permission from S. Joo, O. Kwon, K. Kim, S. Kim, H. Kim, J. Shin, H. Y. Jeong, S. Sengodan, J. W. Han, G. Kim, Nat. Commun. 2019, 10, 697. This work is licensed under the Creative Commons Attribution 4.0 International License (CC BY 4.0). Copyright 2019 The Authors.

3.1. Introduction

Exsolution has been recently explored as a method for the preparation of nanoparticles (NPs) with superior catalytic activity and durability for energy conversion and storage. Specifically, exsolution refers to the formation of metal nanoparticles on the surface of a metal oxide via the release and anchoring of cations from the host lattice to the oxide surface in a reducing atmosphere, producing catalysts with enhanced lifetime compared to traditional deposition techniques (*e.g.*, chemical vapor deposition or wet impregnation) by avoiding particle agglomeration.[1], [2]

Despite its benefits, the exsolution process presents two major challenges. Firstly, a significant amount of exsolved metal can remain embedded in the host bulk due to the limited diffusion rate of metal cations.[3], [4] Secondly, exsolution can cause structural instability in the host material due to excessive loss of cations.[5] To overcome these challenges, several factors governing the degree of exsolution, such as the nature of the host lattice and environmental conditions,[6] have been extensively investigated in simple perovskite[7], [8] (ABO_3) or layered perovskite[9]-[13] ($AA'B_2O_5$). For example, A-site deficiency ($A/B < 1$) in perovskite oxide (ABO_3) has been actively researched recently in terms of cation stoichiometry/non-stoichiometry manipulation.[7], [14]-[16]

Meanwhile, topotactic ion exchange is an interesting soft chemical method that has been applied to numerous perovskite-related compounds for cation replacement.[17], [18] Therefore, it could be envisaged as a solution with wide applicability for the complete exsolution of metal cations without leaving cation defects in the host lattice, thereby maintaining the overall structural features of the parent metal oxide.[17]

Herein, we report the use of topotactic ion exchange to overcome the problems associated with common exsolution techniques. When a stoichiometric layered perovskite oxide ($AA'B_{2-x}C_xO_{5+\delta}$) is used, the exsolution of y moles of C metal from the B site would be accompanied by the formation of the corresponding amount of B-site vacancies (Schottky-type defect) (equation 1). In contrast, in the topochemical ion exchange concept, such layered perovskite oxide can yield x moles of exsolved C metal by the ion exchange with x moles of the guest cation G (equation 2). Overall, the topochemical ion exchange produces the layered perovskite without B-site vacancies, thereby preserving the atomic

ULSAN NATIONAL INSTITUTE OF SCIENCE AND TECHNOLOGY

connectivity of the B–O–B network for an efficient oxygen transport and electron conduction.

$$\underbrace{AA'B_{2-x}C_xO_{5+\delta}}_{\text{Stoichiometric layered perovskite}} \rightarrow \underbrace{AA'B_{2-x}C_{x-y}\square_yO_{5+\delta}}_{\text{Residual layered perovskite with B-site vacancy (}\square\text{)}} + \underbrace{yC}_{\text{Exsolved metal}} \quad (1)$$

$$\underbrace{AA'B_{2-x}C_xO_{5+\delta}}_{\text{Stoichiometric layered perovskite}} + \underbrace{xG}_{\text{Guest cation}} \xrightarrow[\text{exchange}]{\text{Topotactic ion}} \underbrace{AA'B_{2-x}G_xO_{5+\delta}}_{\text{New layered perovskite without B-site vacancy}} + \underbrace{xC}_{\text{Exsolved metal}} \quad (2)$$

We selected the layered perovskite $PrBaMn_{1.7}Co_{0.3}O_{5+\delta}$ (PBMCo) as the host and Fe (Fe^{3+}/Fe^{4+}) as the guest cation. A previous study revealed that, in layered perovskite, the Co cation has a higher tendency to be exsolved toward the surface than Fe, mainly due to the higher co-segregation energy of Co (−0.55 eV) compared to that of Fe (−0.15 eV).[9] Therefore, when the Fe guest cation is externally introduced into the host material, the initial host PBMCo can be converted to $PrBaMn_{1.7}Fe_{0.3}O_{5+\delta}$ (PBMFe) through topotactic cation exchange. This simple synthetic approach not only can readily exsolve most of the cations from the bulk lattice but also can produce new compounds with multiple functionalities by exsolving nanoparticles without leaving cation defects. Moreover, we illustrate that the as-exsolved particles exhibit high catalytic activities, which are verified by solid oxide fuel cell anode test and dry reforming reaction of methane.

Table 3-1 Nomenclature for the compounds based on the Fe infiltrated PBMCo system

Compound	**Abbreviations**
$PrBaMn_{1.7}Co_{0.3}O_{5+\delta}$	PBMCo
$PrBaMn_{1.7}Co_{0.3}O_{5+\delta}$ + 3 wt. % infiltration of Fe	PBMCo-3-Fe
$PrBaMn_{1.7}Co_{0.3}O_{5+\delta}$ + 7 wt. % infiltration of Fe	PBMCo-7-Fe
$PrBaMn_{1.7}Co_{0.3}O_{5+\delta}$ + 12 wt. % infiltration of Fe	PBMCo-12-Fe
$PrBaMn_{1.7}Co_{0.3}O_{5+\delta}$ + 15 wt. % infiltration of Fe	PBMCo-15-Fe
$PrBaMn_{1.7}Co_{0.3}O_{5+\delta}$ + 12 wt. % infiltration of Co-Fe	PBMCo-12-CoFe
$PrBaMn_2O_{5+\delta}$	PBM
$PrBaMn_2O_{5+\delta}$ + 12 wt. % infiltration of Fe	PBM-12-Fe
$PrBaMn_2O_{5+\delta}$ + 12 wt. % infiltration of Co	PBM-12-Co
$PrBaMn_{1.7}Fe_{0.3}O_{5+\delta}$	PBMFe
$PrBaMn_{1.7}Fe_{0.3}O_{5+\delta}$ + 12 wt. % infiltration of Co-Fe	PBMFe-12-CoFe
$PrBa_{0.5}Sr_{0.5}Co_{1.5}Fe_{0.5}O_{5+\delta}$	PBSCF

ULSAN NATIONAL INSTITUTE OF SCIENCE AND TECHNOLOGY

$Ce_{0.9}Gd_{0.1}O_{2-\delta}$	GDC
$La_{0.4}Ce_{0.6}O_{2-\delta}$	LDC
$La_{0.9}Sr_{0.1}Ga_{0.8}Mg_{0.2}O_{3-\delta}$	LSGM

wt. %: weight percent to anode

3.2. Experimental

3.2.1. Synthesis of parent materials

$Pr_{0.5}Ba_{0.5}Mn_{0.85}Co_{0.15}O_{3-\delta}$, $Pr_{0.5}Ba_{0.5}Mn_{0.85}Fe_{0.15}O_{3-\delta}$, and $Pr_{0.5}Ba_{0.5}MnO_{3-\delta}$ were prepared by the Pechini sol-gel synthesis method. The required amounts for stoichiometry of $Pr(NO_3)_3{\cdot}6H_2O$ (Aldrich, 99.9%, metal basis), $Ba(NO_3)_2$ (Aldrich, 99+%), $Mn(NO_3)_2{\cdot}4H_2O$ (Aldrich, 98%), $Fe(NO_3)_3{\cdot}9H_2O$ (Aldrich, 98+%), and $Co(NO_3)_2{\cdot}6H_2O$ (Aldrich, 98+%) were dissolved in distilled water. After complete dissolution, proper amounts of ethylene glycol and citric acid as complexing agents were added to the solution and combustion process on heating plate is followed to make fine powders. These powders were calcined at 600 ^oC for 4 h to eliminate organic residue. The chemical composition of the synthesized powders and their abbreviations are given in Table 3-1.

3.2.2. Fabrication of fuel cells

Commercial electrolyte powders, $La_{0.9}Sr_{0.1}Ga_{0.8}Mg_{0.2}O_{3-\delta}$, (LSGM, 99.9% Kceracell) was pressed into pellet of 0.9 g and sintered at 1475 ^oC. After sintering, pellet was polished to about 250 μm. A buffer layer, $La_{0.4}Ce_{0.6}O_{2-\delta}$ (LDC) was prepared by ball milling stoichiometric amounts of La_2O_3 and CeO_2 (Sigma, 99.99%) in ethanol and then calcined at 1,000 ^oC for 6h. LDC is applied between anode and electrolyte to prevent ionic inter-diffusion. Anode powder PBMCo was mixed with an organic binder (Heraeus V006) (1:2 weight ratio) to make slurry ink. Cathode powders composed of $PrBa_{0.5}Sr_{0.5}Co_{1.5}Fe_{0.5}O_{5+\delta}$ (PBSCF)-$Ce_{0.9}Gd_{0.1}O_{2-\delta}$ (at a weight ratio of 60:40) were mixed with an organic binder (1:1.2 weight ratio) for a cathode slurry ink as described elsewhere.[19], [30] These electrode inks were applied on the LSGM electrolyte pellet by screen printing method to produce a configuration of PBMCo | LDC | LSGM | PBSCF-GDC, which was followed by sintering at 950 ^oC in air for 4 h. The Fe precursor solution was infiltrated on PBMCo after sintering. The porous electrodes had an active area of 0.36 cm^2 and thickness about 20 μm. For the electrochemical tests, Ag wires were fixed to both electrodes using Ag paste as current collectors and the cell was sealed on an alumina tube using a ceramic adhesive (Ceramabond 552, Aremco). The entire cell was placed inside a furnace and heated to the desired temperature. I-V polarization curves were measured using a BioLogic Potentiostat.

3.2.3. Infiltration

A deposition on sample was fulfilled by an infiltration procedure. Precursor solution for infiltration of

ULSAN NATIONAL INSTITUTE OF SCIENCE AND TECHNOLOGY

Fe and Co-Fe were prepared in 0.7 M by dissolving an appropriate amount $Fe(NO_3)_3 \cdot 9H_2O$ (Aldrich, 98+%), $Co(NO_3)_2 \cdot 6H_2O$ (Aldrich, 98+%), and citric acid into distilled water. Precursor solutions were infiltrated into porous PBMCo with various weight percent to parent material (3, 7, and 12 wt. %) and then calcined in air at 450 °C for 4 h. This infiltration procedure was repeated to achieve the targeted weight percent.

3.2.4. Exsolution characterization

To compare the exsolution phenomenon with varying the amount of the deposited Fe on PBMCo, pre-calcined PBMCo was fired at 950 °C in air for 4 h. The sintered PBMCo was infiltrated with Fe precursor solution and reduced at 850 °C in H_2 atmosphere (with 3% H_2O) for 4 h.

The crystal structures of the samples were identified by an XRD (Bruker, D8 Advance, Cu Ka radiation, 40 kV, 40 mA). The morphologies of materials were investigated using SEM (FEI, Nova Nano 230 FE-SEM). TEM images were obtained with a FEI Titan (3) G2 60-300 with an imaging-forming Cs corrector at an accelerating voltage of 80 kV. N_2 adsorption and desorption isotherms measurement was carried out at -196 °C (BELSORP-Mini II, BEL Co.) to evaluate the pore structure and specific surface area. The specific surface area of the catalysts was calculated from the N_2 adsorption and desorption isotherms results by the BET method. XPS analyses were conducted on ESCALAB 250XI from Thermo Fisher Scientific with a monochromatic A1-Kα (ultraviolet He1, He2) X-ray source.

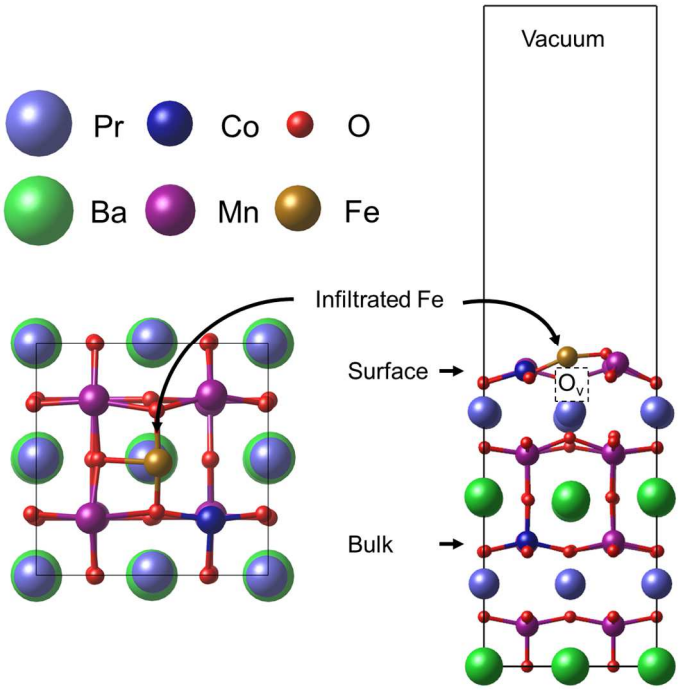

Figure 3-1 Top and side views of surface model structures of Fe infiltrated PBMCo used in our DFT calculations. Note that the locations of initial and final states of the segregated Co are assumed to be the first and the fifth layers in our slab model. For the calculations of Fe infiltrated PBMCo, one Fe atom is added on the surface of PBMCo. The oxygen vacancy formation (O_v) is mostly favorable at a nearest neighbor of surface Co and infiltrated Fe.

ULSAN NATIONAL INSTITUTE OF SCIENCE AND TECHNOLOGY

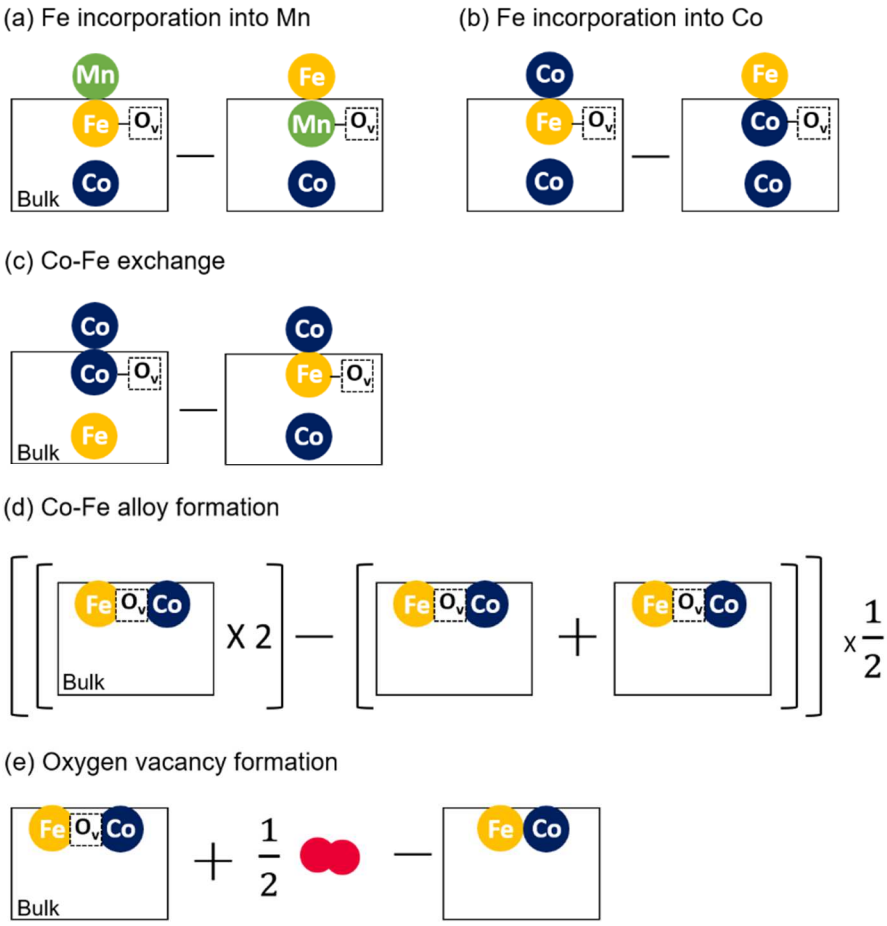

Figure 3-2 Schematic illustration for DFT-calculated energetics at each elementary step. The incorporation energy was defined by the total energy difference between the systems where the infiltrated Fe is located on the surface of PBMCo and at the surface B-metal lattice of (a) Mn or (b) Co. (c) The Co-Fe exchange energy was calculated by the total energy difference between the systems before and after the exchange of the location of surface Fe and bulk Co. (d) The alloy formation energy was calculated by the total energy difference between the systems where two different B-site metals are separated and aggregated. (e) The oxygen vacancy formation energy was calculated by total energy difference of the supercells with and without an oxygen vacancy.

3.2.5. Computational details

DFT calculations were carried out using the Vienna Ab initio Simulation Package (VASP)[31], [32]. Exchange-correlation energies were treated by Perdew-Burke-Ernzerhof (PBE) functional based on generalized gradient approximation (GGA)[33]. An energy cutoff of 400 eV was used for plane-wave expansion. A 3 × 3 × 1 Monkhorst-Pack *k*-point sampling of the Brillouin zone was used for all slab calculations[34]. Gaussian smearing was used with a width of 0.05 eV to determine partial occupancies. Geometries were relaxed using a conjugate gradient algorithm until the forces on all unconstrained atoms were less than 0.03 eV/Å. In order to take into account for on-site Coulomb and exchange

ULSAN NATIONAL INSTITUTE OF SCIENCE AND TECHNOLOGY

interactions, GGA+*U* schemes were used with the effective *U* values of 4.0, 3.3, and 4.0 for Mn, Co, and Fe, respectively. The 8 layered PBMO slab model was constructed with the vacuum thickness of up to 17 Å in the *z*-direction by cleaving a bulk PBMO structure[9]. The dopant position at top surface or in 5th layer represents that it is located at surface or in bulk, respectively.

In order to describe the alloy formation, we substituted two Mn atoms with Co or Fe atom in PBMO (Figure 3-1). The Gibbs free energies were also calculated for the thermodynamics of alloy and oxygen vacancy formation based on our previous calculation scheme (Figure 3-2)[9].

3.2.6. Catalytic activity of dry-reforming of methane

Catalytic activity for dry reforming of methane was evaluated through gas chromatography (GC) (Agilent 7820A GC instrument) with a thermal conductivity detector (TCD) and a packed column (Agilent carboxen 1000). The gas used for GC measurement were controlled using a mass flow controller (MFC) (Atovac GMC1200) and the exact volume value of gas was calibrated through a bubble flow meter.

The 0.2 g of sample powder (950 ^{o}C sintered in air for 4 h) was prepared and packed in the middle of the quartz tube reactor using glass wool. The sample powder was *in-situ* reduced at 900 ^{o}C for 30 minutes while blowing humified H_2 (3% H_2O) gas in a quartz tube reactor.

After reduction, purging for 1 hour with He gas before each measurement to remove residual H_2, then CO_2, CH_4, and He were inserted with a ratio of 20:20:60 ml min^{-1}, respectively.

The dry reforming reaction is shown as below, CO_2 conversion and CO selectivity were calculated using the following equations.[35], [36]

$$CH_4 + CO_2 \leftrightarrow 2CO + 2H_2 \ (\Delta H^0_{298K} = 247\ \mathrm{kJ/mol})$$

$$CO_2\ \text{conversion} = \frac{[CO_2]_{\text{consumed}}}{[CO_2]_{\text{feed}}} \times 100\% = \frac{[CO]_{\text{detect}}}{[CO]_{\text{detect}} + 2[CO_2]_{\text{detect}}} \times 100\%$$

$$CO\ \text{selectivity} = \frac{[CO]_{\text{detect}}}{[CO]_{\text{detect}} + [CO_2]_{\text{detect}}} \times 100\%$$

ULSAN NATIONAL INSTITUTE OF SCIENCE AND TECHNOLOGY

3.3. Result and discussion

3.3.1. System for the topotactic ion exchange/exsolution

Table 3-2 The amount of infiltrated Fe in mole percentage.

Sample	Weight percent of Fe_2O_3 infiltrated (%)	Mol of Fe_2O_3 for the weight percentage to 1 mol of PBMCo	Mole of Fe
PBMCo-12-Fe	12	0.35	0.18
PBMCo-7-Fe	7	0.21	0.10
PBMCo-3-Fe	3	0.09	0.04
Remarks	*(Weight for 1 mol of PBMCo) = 469.28 g/mol *(Weight for 1 mol of Fe_2O_3) = 159.69 g/mol		

In this work, a layered stoichiometric perovskite, $PrBaMn_{1.7}Co_{0.3}O_{5+\delta}$, was selected as the ion exchange host for the preferential exsolution of Co to exemplify the topotactic manipulation. We selected Co as exsolving cation since Co in the B sites has the highest co-segregation energy toward exsolution among various transition metals (Mn, Co, Ni, and Fe), whereas Fe was chosen as the guest material with the lowest co-segregation energy.[9] The deposition of guest cation was done by infiltrating a nitrate solution having different weight percentages of Fe (0, 3, 7, and 12 wt.% with respect to the host material) on $Pr_{0.5}Ba_{0.5}Mn_{0.85}Co_{0.15}O_{3-\delta}$. The amount of infiltrated Fe was also calculated in a mole percentage as shown in Table 3-2. After the infiltration, $Pr_{0.5}Ba_{0.5}Mn_{0.85}Co_{0.15}O_{3-\delta}$ deposited with Fe oxide was annealed in humified hydrogen at 850 °C to exsolve nanoparticles along with phase transition from simple perovskite to layered perovskite structure. Table 3-1 summarizes the different abbreviations of the samples.

ULSAN NATIONAL INSTITUTE OF SCIENCE AND TECHNOLOGY

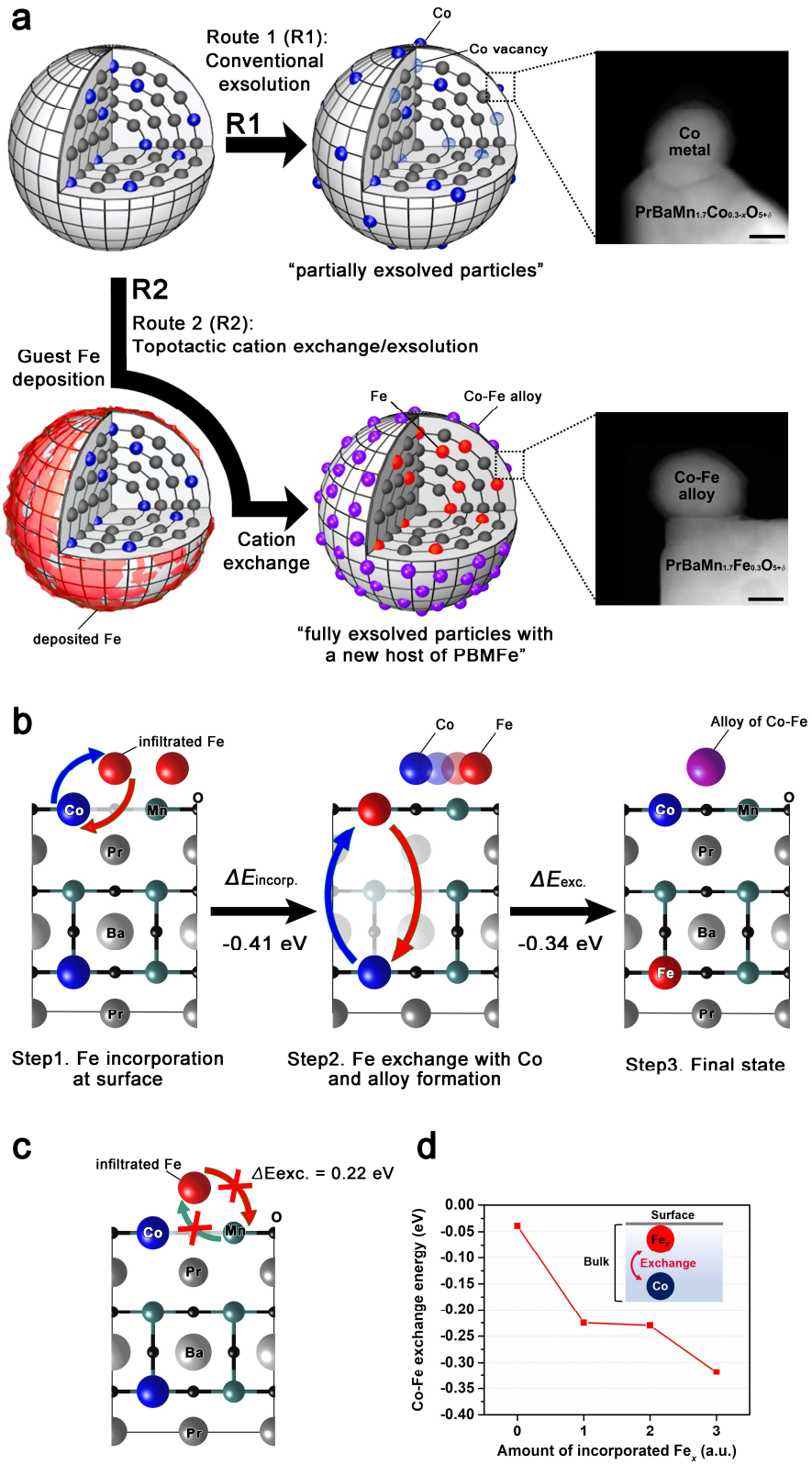

Figure 3-3 Schematic of exsolution process and DFT calculations. (a) Exsolution process with and without topotactic ion exchange. (b) Topotactic ion exchange energetics for the mechanism of particle exsolution via Fe infiltration on the PBMCo surface. (c) The unfavorable incorporation energy of infiltrated Fe with Mn of the top surface. (d) Calculated energetics for the Co–Fe$_x$ exchange depending on arbitrary Fe concentration.

ULSAN NATIONAL INSTITUTE OF SCIENCE AND TECHNOLOGY

3.3.2. Ion exchange and density functional theory calculation

In the process of Co exsolution under a reducing atmosphere, the Co cation in the host material PBMCo undergoes topotactic ion exchange with the deposited Fe due to the difference of co-segregation energy between Co and Fe. Thus, Co tends to be exsolved to the surface while Fe remains in the bulk in the $PrBaMn_{1.7}T_{0.3}O_{5+\delta}$ system (T = Mn, Ni, Co, or Fe).[9] In a stoichiometric layered perovskite, the exsolution of transition metal cation was observed along with the phase transition under a reducing atmosphere (R1 in Figure 3-3a), leaving B-site vacancies (Schottky-type defect). Under typical conditions, only a limited fraction of B-site transition metal can be exsolved. In a stoichiometric layered perovskite of $PrBaMn_{1.7}Ni_{0.3}O_{5+\delta}$ composition, only 58% of Ni can migrate to the surface, leaving many B-site vacancies,[9] with the concomitant decrease in both the oxygen ion conduction and electron conduction paths. On the contrary, for the topotactic ion exchange/exsolution method (R2 in Figure 3-3a), the guest cation is deposited on the patent stoichiometric layered perovskite material followed by reduction. During the exsolution process, the topotactic ion exchange occurs between the lattice Co and the deposited Fe. In parallel, all the Co cations from the B sites are exsolved without the formation of B-site vacancies. The filling of the B sites eventually leads to improved ionic and electrical conduction paths. In the topotactic ion exchange process, Fe dissolves into the underlying perovskite lattice due to its low co-segregation energy compared to that of other transition metals.

To simulate the topotactic ion exchange process between B-site cations, DFT calculation was performed. We assumed that the process occurs through two major stages, *i.e.*, (1) incorporation of the infiltrated Fe into the lattice and (2) exchange between the incorporated Fe and the host Co, and the energy at each stage was investigated. This mechanism of cation exchange in layered perovskites can be expressed in point defect (Schottky-type defect) reactions as follows:

Exsolution without cation exchange,

$$Co_{Co}^{\times} + O_{O}^{\times} \leftrightarrow CoO + V_{O}^{\bullet\bullet} + V_{Co}'' \quad (4)$$

$$CoO \leftrightarrow Co_{(\text{metallic exsolution})} + \frac{1}{2}O_2 \quad (5)$$

Exsolution by topotactic ion exchange,

$$Co_{Co}^{\times} + O_{O}^{\times} + FeO_{(\text{infiltrated})} \leftrightarrow CoO_{(\text{exsolved})} + V_{O}^{\bullet\bullet} + Fe_{Co}^{\times} \quad (6)$$

$$CoO \leftrightarrow Co_{(\text{metallic exsolution})} + \frac{1}{2}O_2 \quad (7)$$

Where $Co_{Co}^{\times}$ denotes the Co in the Co site with net charge zero, $O_{O}^{\times}$ denotes oxygen in the oxygen site with net charge zero, $V_{O}^{\bullet\bullet}$ denotes the oxygen ion vacancy with the net charge of +2, V_{Co}'' denotes the cation vacancy in the Co site with the net charge of −2, $Fe_{Co}^{\times}$ denotes the incorporated Fe in the Co site with net charge zero, and FeO/CoO denotes the Fe/Co oxide, respectively.

Once Fe is deposited on the host PBMCo, Fe incorporates into the near surface of PBMCo through the exchange with the Co cations on the B sites. Since both the exsolved Co and host Mn can co-exist at

ULSAN NATIONAL INSTITUTE OF SCIENCE AND TECHNOLOGY

the near surface of PBMCo, we compared two possible exchange pathways, Fe ↔ Co and Fe ↔ Mn, on the B cation layer of the surface. Our results show that Fe ↔ Co (−0.41 eV) is thermodynamically more favored than Fe ↔ Mn (0.22 eV) (Figure 3-3b and Figure 3-3c). Thus, the incorporation of Fe occurs through its exchange with Co. After the incorporation, further exchange between the incorporated Fe and the bulk Co is thermodynamically favorable, with an exchange energy of −0.34 eV. Therefore, it can be concluded that Co exsolution is facilitated by the incorporation of Fe.

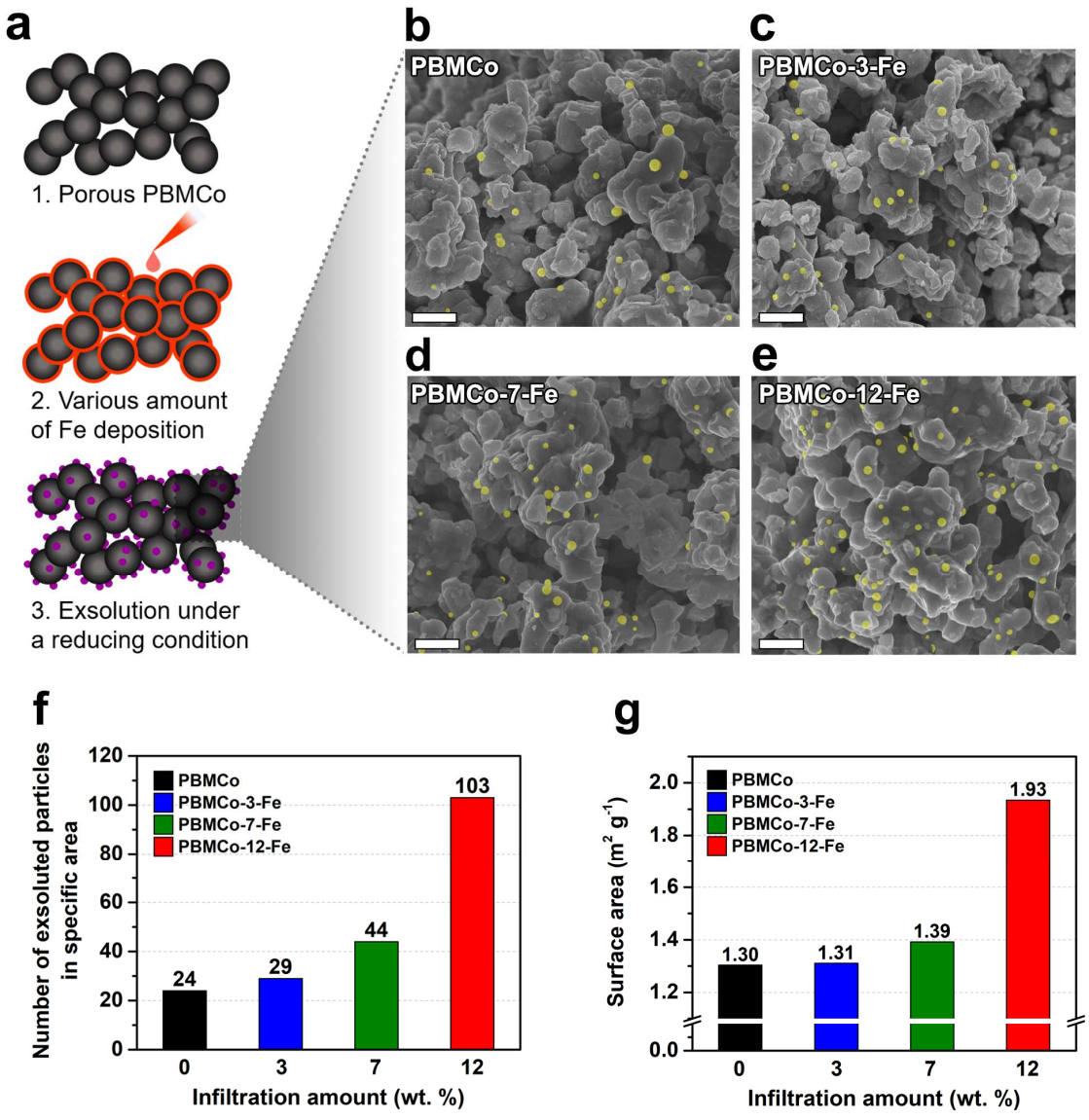

Figure 3-4 SEM images and population of exsolved particles. (a) Sample preparation process for confirming the correlation between the amount of infiltrated Fe and the population of exsolved nanoparticles. (b)–(e) SEM images of (b) PBMCo, (c) PBMCo-3-Fe, (d) PBMCo-7-Fe, and (e) PBMCo-12-Fe (exsolved nanoparticles are highlighted in yellow highlight); scale bars are 500 nm. (f) Number of exsolved particles in specific area counted by Image J. (g) Specific surface area calculated by the BET method.

ULSAN NATIONAL INSTITUTE OF SCIENCE AND TECHNOLOGY

Next, the Co–Fe exchange energy was calculated as a function of the incorporated Fe concentration in an arbitrary unit (Figure 3-3d). As the arbitrary concentration of the incorporated Fe increases up to the specific concentration, the Co–Fe exchange is thermodynamically favored. This also supports that the Fe incorporation into the host PBMCo possibly accelerates Co exsolution. The Gibbs energy of aggregation ($\Delta G_{aggr.}$) of Co–O_v–Fe at the surface (surface alloy formation) is 0.01 eV, implying that the aggregation of Co and Fe requires only little energy on the surface. This result is consistent with that of the TEM investigation that will be discussed later, which evidences the formation of a Co–Fe alloy. In

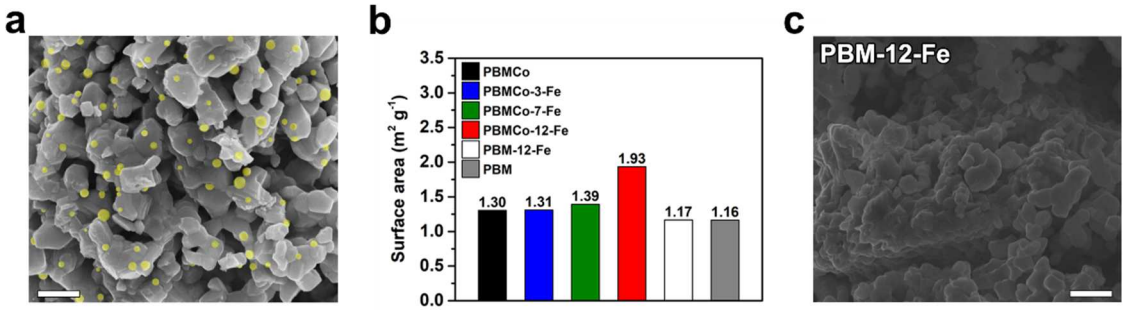

Figure 3-5 SEM images and population of particles. (a) SEM image of PBMCo-15-Fe; scale bar 500 nm. (b) Comparison of the specific surface area between samples calculated by the BET methods. (c) SEM image of PBM-12-Fe; scale bar 500 nm.

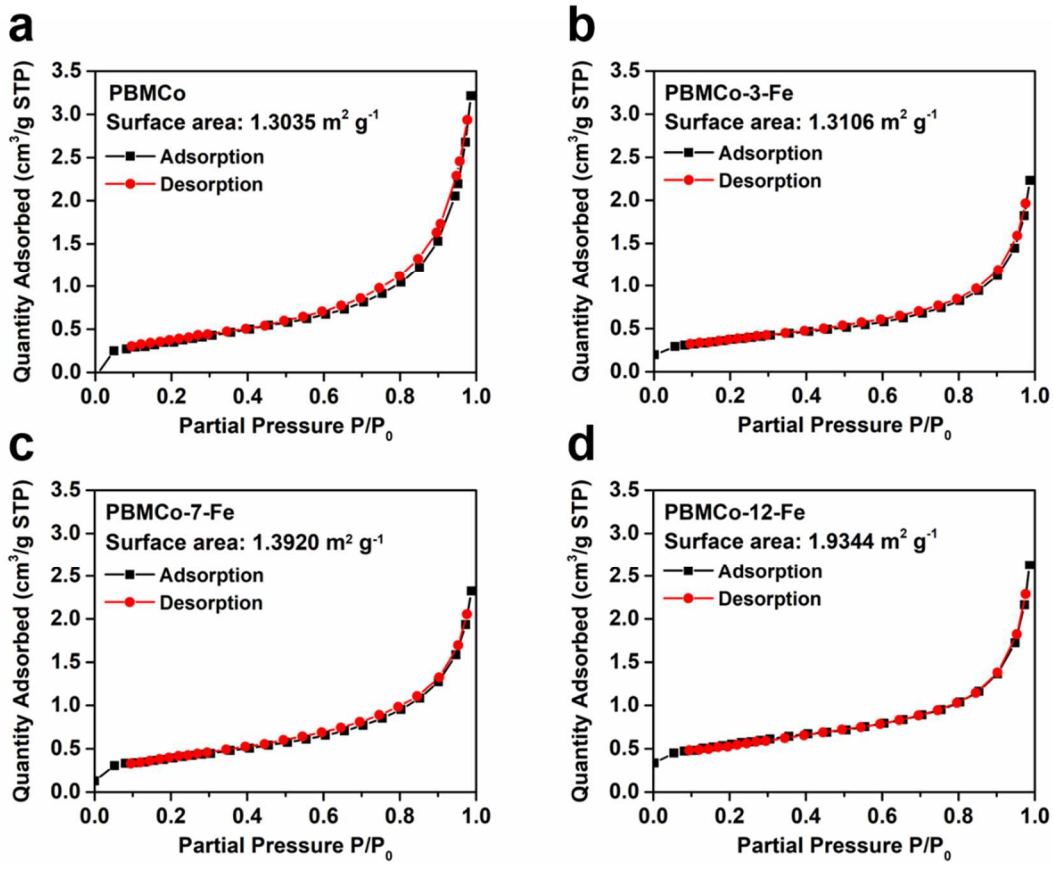

Figure 3-6 N_2 adsorption and desorption isotherms measurement of (a) PBMCo, (b) PBMCo-3-Fe, (c) PBMCo-7-Fe, and (d) PBMCo-12-Fe.

ULSAN NATIONAL INSTITUTE OF SCIENCE AND TECHNOLOGY

addition, the lower oxygen vacancy formation energy at the surface of PBMCo-12-Fe (2.52 eV) compared to that of the host PBM (2.97 eV) would promote further reduction of Co–Fe aggregation to form Co–Fe alloy NPs.

3.3.3. Correlation between exsolved particles and infiltration

To provide evidence of the occurrence of topotactic ion exchange, we varied the amount of infiltrated Fe precursor and investigated the correlation between the amount of Fe deposition and the population of exsolved nanoparticles through scanning electron microscopy (SEM) and Brunauer–Emmett–Teller

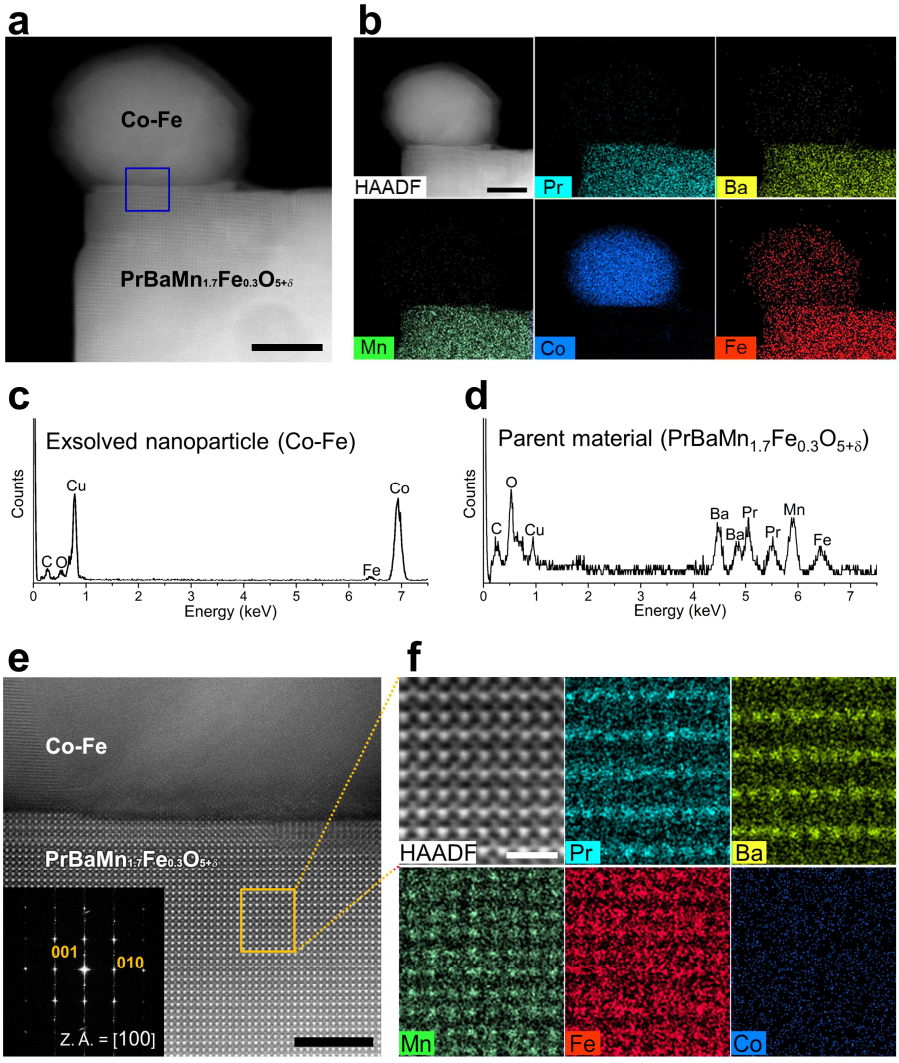

Figure 3-7 TEM analysis of exsolved particles and the parent material of PBMCo-12-Fe. (a) HAADF scanning TEM image of PBMCo-12-Fe. (b) EDS elemental map of Pr, Ba, Mn, Co, and Fe; scale bar 20 nm. (c) EDS spectrum of the exsolved nanoparticles. (d) EDS spectrum of the parent material of PBMCo-12-Fe. (e) HADDF scanning TEM image of PBMCo-12-Fe (blue square in Figure 3-7a) and the corresponding fast-Fourier transformed pattern with zone axis = [100]; scale bar 5 nm. (f) EDS elemental map of Pr, Ba, Mn, Fe, and Co in the parent material of PBMCo-12-Fe (yellow rectangle in Figure 3-7d); scale bar 1 nm.

ULSAN NATIONAL INSTITUTE OF
SCIENCE AND TECHNOLOGY

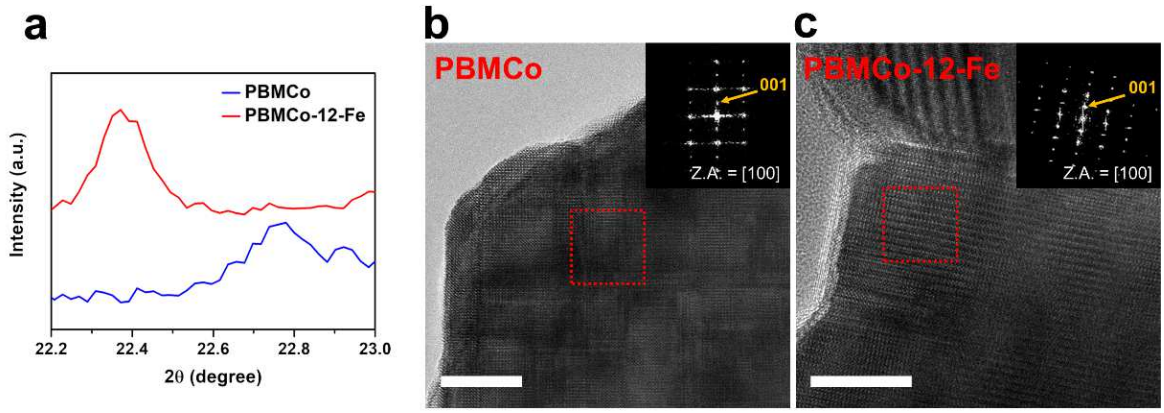

Figure 3-8 (a) X-ray diffraction patterns of PBMCo and PBMCo-12-Fe samples around 22 º. HR TEM image of (b) PBMCo and (c) PBMCo-12-Fe samples and the corresponding fast-Fourier transformed pattern with zone axis = [100]; scale bar 10 nm.

(BET) analysis. Figure 3-4a shows the schematics of the experimental process. The SEM images of PBMCo, PBMCo-3-Fe, PBMCo-7-Fe, and PBMCo-12-Fe are shown in Figure 3-4b–e. The micrographs illustrate that spherical exsolved nanoparticles of 20–50 nm are evenly distributed on the surface of the parent material. Interestingly, as the amount of infiltrated Fe precursor increase from 0 to 12 wt.%, more spherical particles seem to be exsolved to the surface of the layered perovskite. To provide a more quantitative correlation between the population of particles and the amount of deposited Fe, the exsolved nanoparticles in a specific area were numbered by an image analysis tool (Image J software). As seen in Figure 3-4f, the results demonstrate that the amount of deposited Fe oxides promotes exsolution, particularly a significant increase up to 12 wt.% of infiltrated Fe oxides. With the amount of 15 wt.% infiltration, number of the exsolved nanoparticles in a specific area is not deviated from that of 12 wt.% (counted as 98 particles shown in Figure 3-5a), indicating that the promotion of exsolution is saturated at the certain amount of the deposition. These trends are in good agreement with the BET analysis of the specific surface area of the material, as shown in the right axis of Figure 3-4f, Figure 3-5 and Figure 3-6. This can be explained by the fact that the specific surface area is affected only by the exsolved nanoparticles, not by the amount of Fe deposition. To validate this statement, we deposited Fe on $Pr_{0.5}Ba_{0.5}MnO_{3-\delta}$ and annealed it in H_2 to form a PBM with layered perovskite structure. The samples with 12 wt.% Fe (PBM-12-Fe) and without Fe (PBM) show a specific surface area of 1.16 and 1.17 $m^2\ g^{-1}$, respectively (Figure 3-5b), and the surface morphology of PBM-12-Fe (Figure 3-5c) appears to be smooth, indicating that the contribution to the specific surface area by infiltration of 12 wt.% Fe on the layered perovskite support is negligible.

3.3.4. Examination of exsolved particles and parent oxide

To investigate the crystalline structure and composition of the layered perovskite with exsolved nanoparticles, we examined the samples using transmission electron microscopy (TEM). As shown in

ULSAN NATIONAL INSTITUTE OF SCIENCE AND TECHNOLOGY

the high-angle annular dark field (HAADF) scanning TEM image of PBMCo-12-Fe (Figure 3-7a), nanoparticles having about 30 nm diameter were exsolved from the parent material. In addition, the PBMCo-12-Fe sample was subjected to energy dispersive spectroscopy (EDS) (Figure 3-7b), showing that the exsolved nanoparticles consist of a Co–Fe alloy, and the parent layered perovskite contains Pr, Ba, Mn, and Fe, which is consistent with the EDS spectrum results (Figure 3-7c and d). This disappearance of Co in the lattice is due to the topotactic ion exchange between the lattice Co and deposited Fe, clearly showing that Co and Fe switch their lattice positions. To gain further insights on the crystal lattice and the topotactic ion exchange, we performed atomic-scale scanning TEM analysis. The A-site ordering was observed by a small additional spot in the fast-Fourier transformed (FFT) pattern indexed to (001) of the tetragonal structure (Figure 3-7e). Furthermore, atomic-scale EDS mapping was conducted in the parent oxide (orange rectangle in Figure 3-7e) to investigate the A-site cation ordering and the positions of Co and Fe (Figure 3-7f). It was found that the atomic positions of Pr, Ba, and Mn remained unaltered, while some Fe was observed in the position of Mn, which implies that Fe entered the B sites of PBMCo. Meanwhile, Co signals were not clearly observed in the EDS mapping, which demonstrates that most of the Co was exsolved to the surface due to the topotactic ion exchange with Fe.

Moreover, we examined XRD peaks around 22 ° to determine the change in lattice as exchanging cations (Figure 3-8a). The peaks around 22 ° corresponding to (200) are 22.79 ° and 22.37 ° for PBMCo and PBMCo-12-Fe, respectively. The peak shift to the left indicates that the lattice expansion occur due to the cation exchange of smaller Co ions (Co^{2+} (r=0.745 Å) or Co^{3+} (r=0.545 Å)) and larger Fe ions (Fe^{2+} (r = 0.780 Å) or Fe^{3+} (r=0.645 Å)).[19], [20] We also measured high-resolution TEM to confirm the lattice constants before and after the exchange. As shown in the HR TEM images, the lattice spaces

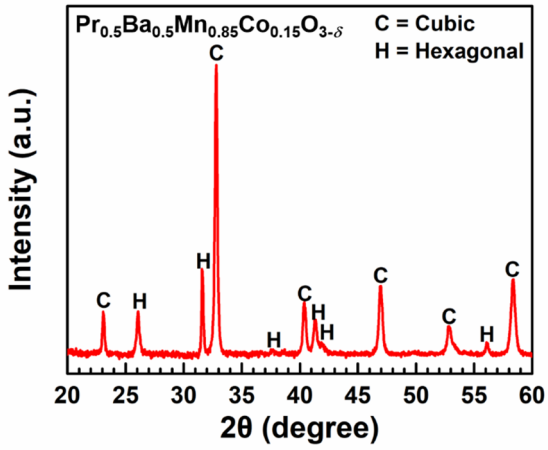

Figure 3-9 X-ray diffraction patterns of $Pr_{0.5}Ba_{0.5}Mn_{0.85}Co_{0.15}O_{3-\delta}$ sintered at 950 °C for 4 h in air.

ULSAN NATIONAL INSTITUTE OF SCIENCE AND TECHNOLOGY

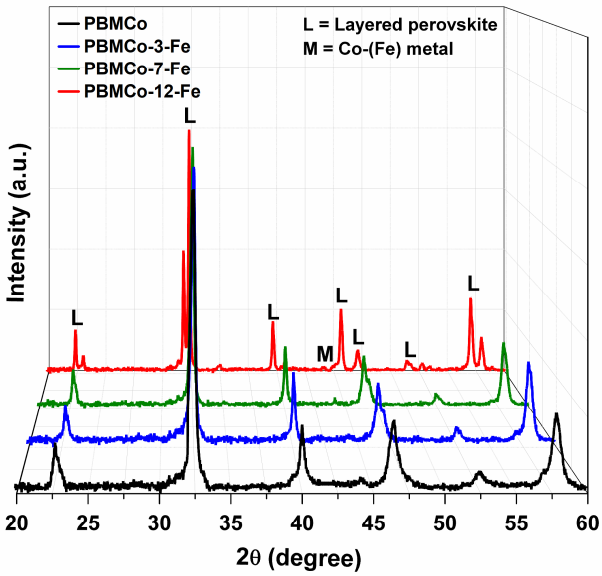

Figure 3-10 X-ray diffraction patterns of PBMCo, PBMCo-3-Fe, PBMCo-7-Fe, and PBMCo-12-Fe samples.

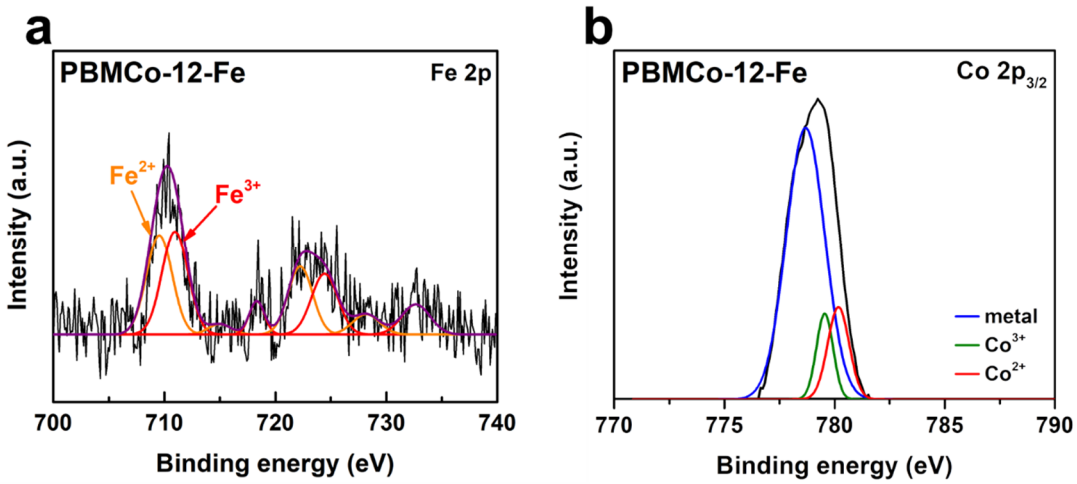

Figure 3-11 X-ray photoelectron spectroscopy of (a) Fe 2p for PBMCo-12-Fe and (b) Co $2p_{3/2}$ for PBMCo-12-Fe.

between (001) planes of before (Figure 3-8b) and after (Figure 3-8c) exchange are identified as 0.803 and 0.815 nm by fast-Fourier transformed pattern, respectively. Therefore, it can be concluded that the lattice constant of the layered perovskite somewhat increases after the exchange between Co and Fe.

3.3.5. X-ray diffraction and X-ray photoelectron spectroscopy analysis

The perovskite oxides were analyzed by X-ray diffraction before and after reduction. From the XRD diffraction pattern (Figure 3-9), it can be deduced that the host material samples sintered at 950 °C in air for 4 h exhibit simple perovskite structures of mixed cubic and hexagonal phases without secondary

ULSAN NATIONAL INSTITUTE OF SCIENCE AND TECHNOLOGY

phase. The diffraction patterns of the PBMCo, PBMCo-3-Fe, PBMCo-7-Fe, and PBMCo-12-Fe samples are shown in Figure 3-10. Under a reducing atmosphere, all the samples experience phase transition from simple perovskite to layered perovskite along with the formation of exsolved nanoparticles on the surface of host materials. For PBMCo, the peak for exsolved Co metal is observed at $2\theta = 44.26^{o}$ (JCPDS card#15-0806). As the amount of deposited Fe increases, the peak for metal is lower-angle shifted (44.26 ^{o} for PBMCo and PBMCo-3-Fe and 44.17 ^{o} for PBMCo-7-Fe and PBMCo-12-Fe, respectively) due to the formation of the Co–Fe alloy, which originates from the dissolution of Fe in the Co lattice.[21] The diffraction pattern of PBMCo-12-Fe exhibits several additional peaks that are absent in those of the other perovskite oxides. This can be ascribed to the formation of $PrBaMn_{1.7}Co_{0.3-y}Fe_yO_{5+\delta}$ from $Pr_{0.5}Ba_{0.5}Mn_{0.85}Co_{0.15}O_{3-\delta}$ as a result of the swapping between Co and Fe cations according to equation (8). When the B sites of Co are fully substituted by the Fe cations, the parent material is transformed into $PrBaMn_{1.7}Fe_{0.3}O_{5+\delta}$, whose characteristic peak splitting is easily

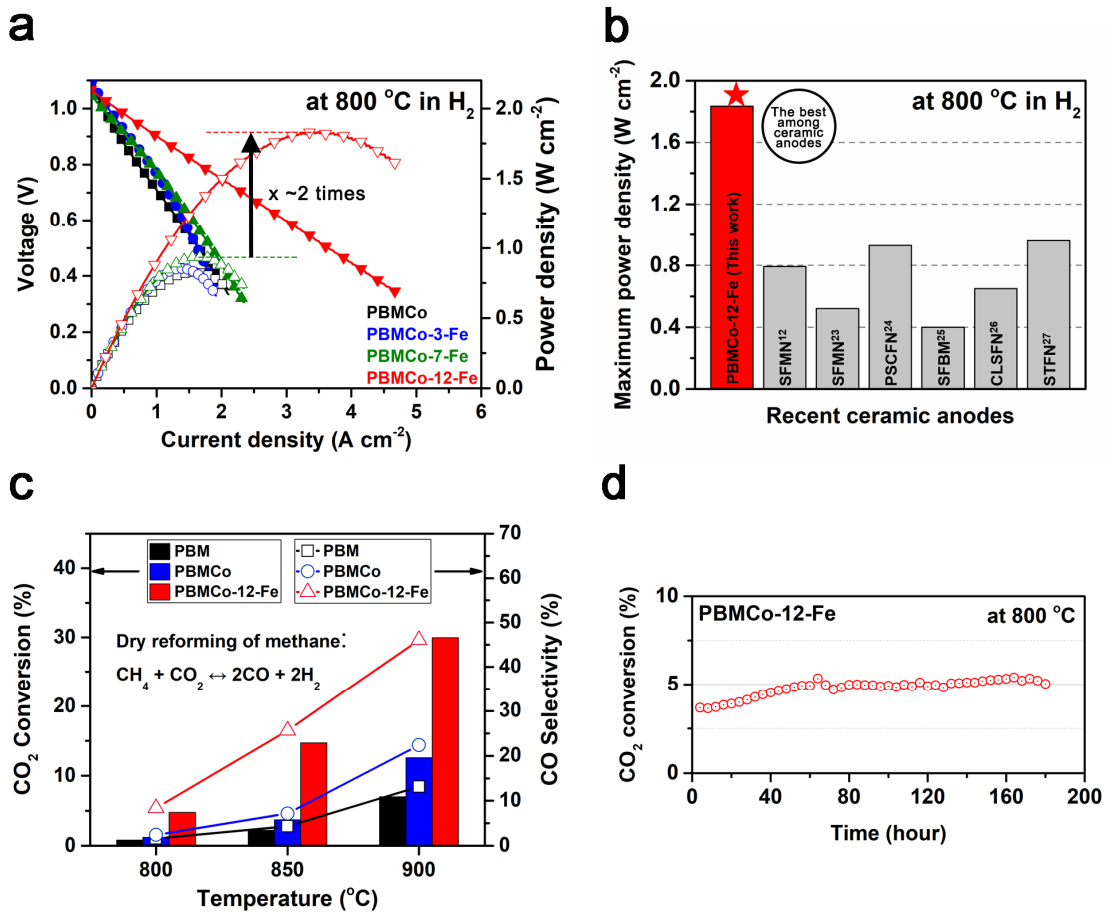

Figure 3-12 Catalytic properties of the PBMCo-*x*-Fe samples. (a) *I-V* curve and the maximum power densities of the PBMCo-x-Fe samples. (b) Comparison of the maximum power density at 800 °C in H_2 from the present work and other reported studies.[12], [23]-[27] (c) Conversion of CO_2 and selectivity of CO measured for PBM, PBMCo, and PBMCo-12-Fe in dry reforming of methane at various temperatures. (d) Time-dependence of CO_2 conversion for PBMCo-12-Fe in dry reforming of methane at 800 °C.

ULSAN NATIONAL INSTITUTE OF SCIENCE AND TECHNOLOGY

distinguishable from that of $PrBaMn_{1.7}Co_{0.3}O_{5+\delta}$.[31] These results clearly demonstrate the topotactic ion exchange between the host cation Co and the deposited Fe that leads to the selective exsolution of Co without any change in the crystal structure except the exchange of B-site cations.

$$Pr_{0.5}Ba_{0.5}Mn_{0.85}Co_{0.15}O_{3-\delta} + Fe_2O_3\ (\text{deposition})$$
$$\xrightarrow{reducing} PrBaMn_{1.7}Co_{0.3-y}Fe_yO_{5+\delta} + yCo - Fe\ (\text{exsolution and formation of alloy}) \quad (8)$$

X-ray photoelectron spectroscopy (XPS) was performed to determine the oxidation states of B-site dopants in PBMCo-3-Fe, PBMCo-7-Fe, and PBMCo-12-Fe. As shown in Figure 3-11, the binding energy peaks of Fe ions in the bulk for Fe $2p_{3/2}$ and Fe $2p_{1/2}$ consist of 710 and 723.7 eV corresponding to Fe^{2+}, 712.5 and 725.5 eV corresponding to Fe^{3+}, respectively. For the all samples, Fe is present as the form of mixed Fe^{2+} and Fe^{3+}. In the case of Co, Co metal is predominant and Co^{2+} and Co^{3+} coexist in a similar ratio.

ULSAN NATIONAL INSTITUTE OF SCIENCE AND TECHNOLOGY

3.3.6. Catalytic activity

To investigate the applicability of the present topotactic ion exchange/exsolution method, the electrochemical performance of fuel cells based on PBMCo-*x*-Fe as the anode was evaluated and compared with that of a PBM anode. The fuel cells with a configuration of PBMCo-*x*-Fe | LDC | LSGM | PBSCF-GDC were tested in humidified H_2 (with 3% H_2O) as the fuel and ambient air as the oxidant. The maximum power densities (MPDs) were 0.826, 0.853, 0.938, and 1.834 W cm^{-2} for PBMCo, PBMCo-3-Fe, PBMCo-7-Fe, and PBMCo-12-Fe, respectively, at 800 °C in humidified H_2 (Figure 3-12a). The number of exsolved particles was found to increase with the amount of Fe infiltration due to the topotactic ion exchange, which resulted in a tremendous enhancement of the electrochemical performance of the SOFC anode. In contrast, the samples without metal exsolution, *i.e.*, the parent PBM

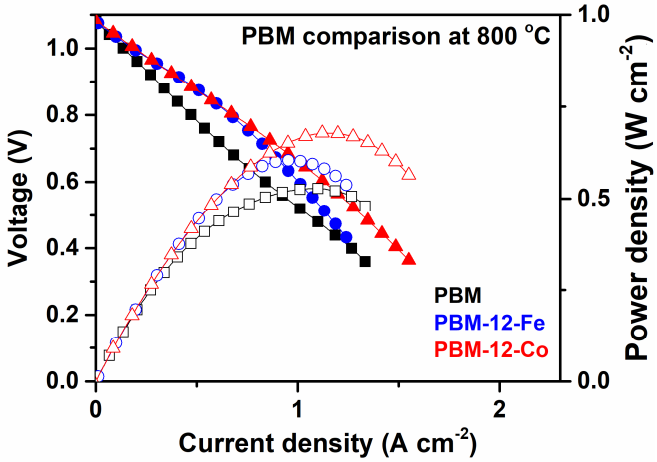

Figure 3-13 I-V curve and power densities of the PBM, PBM-12-Fe, and PBM-12-Co at 800 ºC in H_2 (3% H_2O).

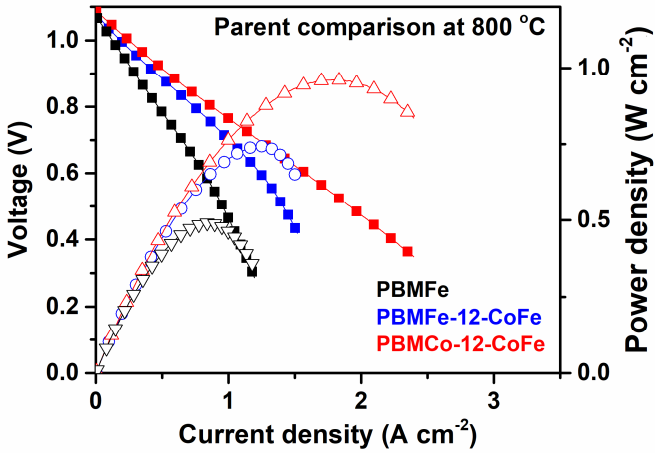

Figure 3-14 I-V curve and power densities of the PBMFe-12-CoFe and PBMCo-12-CoFe at 800 ºC in H_2 (3% H_2O).

ULSAN NATIONAL INSTITUTE OF
SCIENCE AND TECHNOLOGY

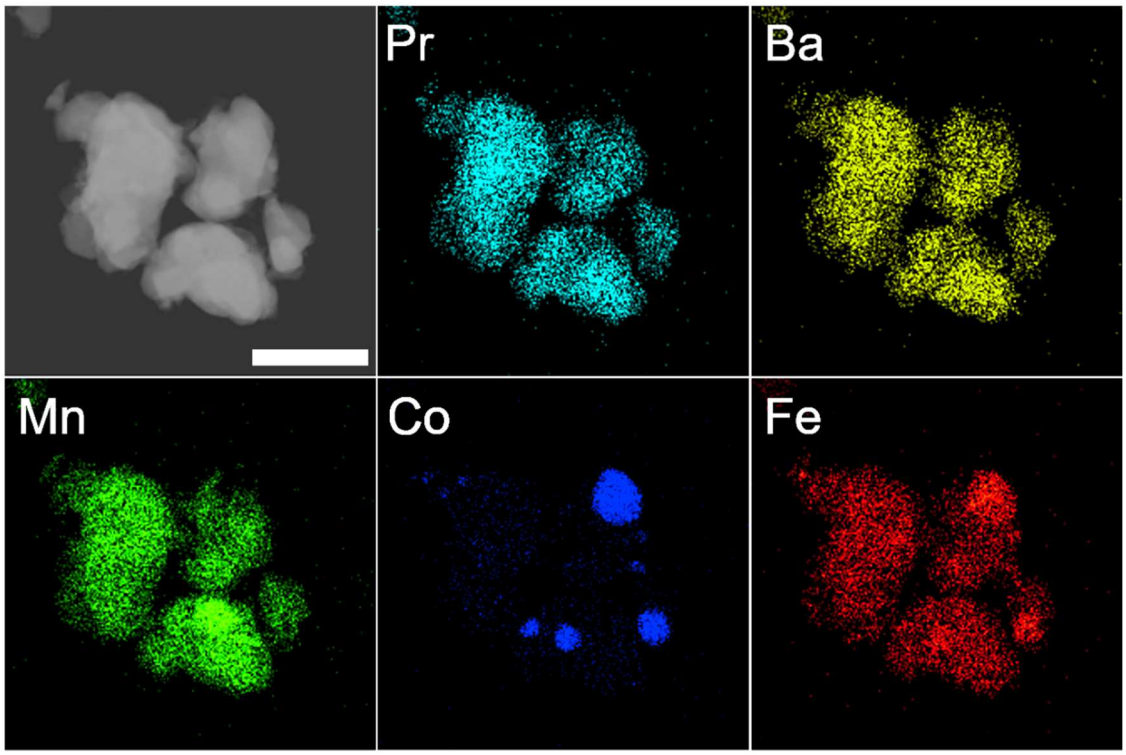

Figure 3-15 High-angle annular dark field (HAADF) image of PBMFe-12-CoFe (NPs formed by infiltration) sample with the EDS elemental map of Pr, Ba, Mn, Co, Fe, and O; scale bar 500 nm.

anodes with deposited Co and Fe catalyst (Figure 3-13), showed no increment in the electrochemical performance, suggesting that the exsolved particles formed by topotactic ion exchange play a key role in the catalytic activity.

To clarify the effect of the cation exchange on the electrochemical performance, Co–Fe infiltrated PBMFe and Co–Fe infiltrated PBMCo were evaluated (Figure 3-14). PBMFe was used for comparative purposes to simulate the parent material after the cation exchange, since the bulk of PBMCo-12-Fe is considered to alter to PBMFe through the cation exchange. The MPD values of PBMFe-12-CoFe and PBMCo-12-CoFe were determined to be 0.743 W cm^{-2} and 0.962 W cm^{-2}, respectively, revealing that the catalytic activity of the Co–Fe alloy particles infiltrated on the parent PBMFe and PBMCo without topotactic cation exchange is not as high as that of the cation-exchanged PBMCo-12-Fe. This can be attributed to the difference in surface morphology between samples. As displayed in the HAADF scanning TEM image of the PBMFe-12-CoFe sample (Figure 3-15), the infiltrated Co–Fe alloy particles exist irregularly as coarsened particles with a size of 50–300 nm. In contrast, exsolved nanoparticles of 20–50 nm are uniformly distributed on the surface of the PBMCo-12-Fe sample (Figure 3-4e). These results are in line with previous findings that present agglomeration and coarsening of catalytic NPs by infiltration as well-known concerns.[22]

ULSAN NATIONAL INSTITUTE OF SCIENCE AND TECHNOLOGY

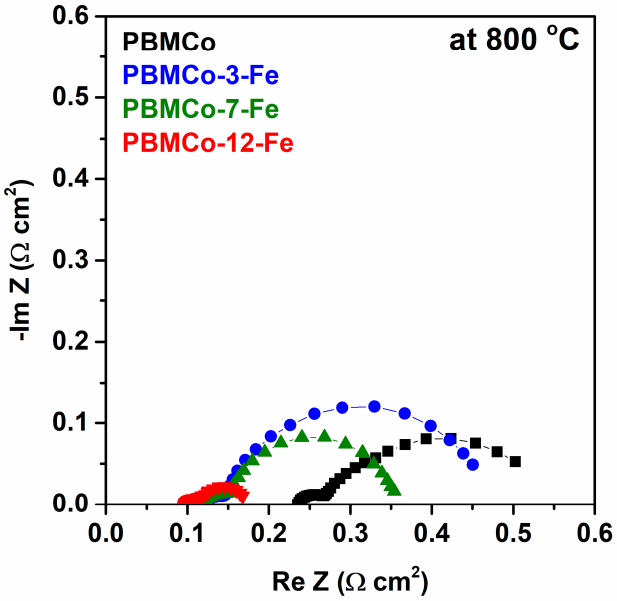

Figure 3-16 Impedance spectra of the PBMCo, PBMCo-3-Fe, PBMCo-7-Fe, and PBMCo-12-Fe at 800 ºC in H_2 (3% H_2O).

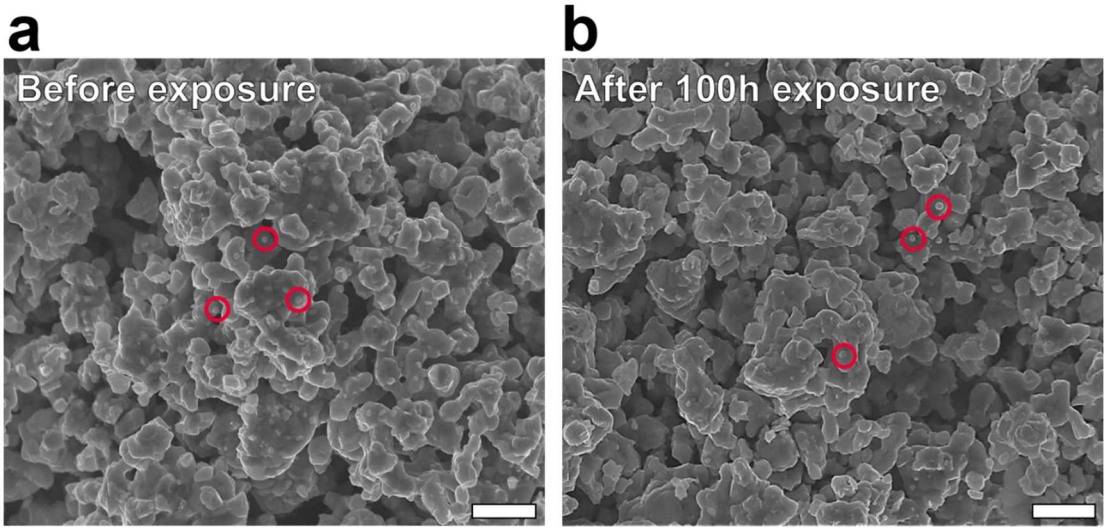

Figure 3-17 Comparison in SEM surface morphology of PBMCo-12-Fe before and after exposure to H_2 (with 3% H_2O) at 800 ºC for 100 hours. The red circles indicate the exsolved nanoparticles; scale bar 500 nm.

The non-ohmic resistances for PBMCo-3-Fe, PBMCo-7-Fe, and PBMCo-12-Fe were 0.330, 0.237, and 0.071 Ω cm^2, respectively, at 800 °C in H_2 (with 3% H_2O) (Figure 3-16), which are consistent with the trends observed for the maximum power density. In particular, the single cell performance of PBMCo-12-Fe demonstrates superior catalytic activity among recently developed ceramic anodes using exsolution[12], [23]-[27] (Figure 3-12b). Additionally, to measure the stability of the particles obtained via the topotactic ion exchange/exsolution method, we compared the SEM images of the PBMCo-12-

ULSAN NATIONAL INSTITUTE OF
SCIENCE AND TECHNOLOGY

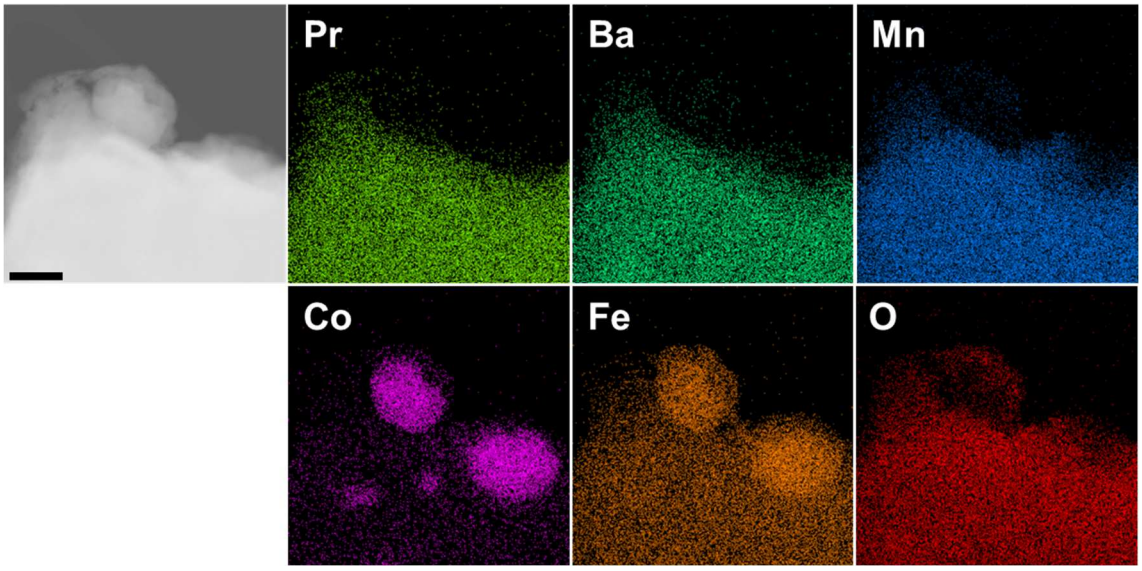

Figure 3-18 High-angle annular dark field (HAADF) image of PBMCo-12-Fe sample with the EDS elemental map of Pr, Ba, Mn, Co, Fe, and O after DRM test at 900 ºC; scale bar 100 nm.

Fe sample after prolonged exposure to 3% humidified hydrogen. As can be seen in Figure 3-17, the exsolved particles maintain their morphologies without undergoing agglomeration even after exposure at 800 °C in humidified H_2 over 100 h.

The catalytic activity of the samples for the dry reforming of methane (DRM) was also assessed using a quartz tube reactor, since Co-based species are known to be excellent catalysts for DRM.[28] At 900 °C, the CO_2 conversion using the PBMCo-12-Fe sample reached 30%, which is almost two times higher than that of PBMCo and four times higher than that of PBM, as shown in Figure 3-12c. The higher conversion of CO_2 for PBMCo-12-Fe strongly supports its excellent capability as DRM catalyst with a long-term stability over 160 h (Figure 3-12d). As shown in Figure 3-18, Co-Fe alloy has an overall metallic phase after DRM reactions and some FeO_x are formed on the surface of Co-Fe alloy due to the difference in redox property of Co and Fe[1]. The reactions involving CO_2 oxidation and CH_4 reduction during DRM are given by the following steps (equation (9) to (11)) according to a Mars-van Krevelen (MvK) mechanism[29]. That is, Co-Fe alloy particles undergo de-alloying/re-alloying process during DRM and consequently, FeO on the surface reacts with carbon deposited on Co to form CO (equation (11)).

$$CH_4 \rightarrow C_{Co} + 2H_2 \quad (9)$$

$$Fe + xCO_2 \leftrightarrow FeO_x + xCO \quad (10)$$

$$FeO_x + C_{Co} \rightarrow xCO + Co + Fe \quad (11)$$

3.4. Conclusions

In summary, we have demonstrated the first example of a topotactic ion exchange/exsolution method

ULSAN NATIONAL INSTITUTE OF
SCIENCE AND TECHNOLOGY

that offers extensive control over the structure and properties of the obtained nanoparticles. The effectiveness of this approach emphasizes the utility of the topotactic ion exchange manipulation for the selective exsolution of catalytic nanoparticles in oxide materials. The topotactic cation exchange between Co and Fe can occur spontaneously due to the favorable incorporation energy (−0.41 eV) and exchange energy (−0.34 eV) for the deposition of the guest material Fe on the host material PBMCo, consequently resulting in the transformation of PBMCo into PBMFe, according to the results of DFT calculation. The maximum power density of an electrolyte-supported cell with a PBMCo-12-Fe anode reaches 1.834 W cm^{-2} in humidified H_2 at 800 °C, achieving excellent electrochemical performance compared to other recently developed ceramic anodes. In addition, the catalyst activity in DRM is improved about four times and two times compared to PBM and PBMCo, respectively, at 900 °C. This approach based on topotactic cation exchange provides a powerful methodology for controlling the properties of exsolution by actively customizing the material through external cation intercalation, which goes beyond the existing methods that depend on the characteristics of the material itself.

ULSAN NATIONAL INSTITUTE OF SCIENCE AND TECHNOLOGY

References

[1] D. Neagu, G. Tsekouras, D. N. Miller, H. Menard, J. T. S. Irvine, Nat Chem **2013**, 5, 916.

[2] Y. Nishihata, J. Mizuki, T. Akao, H. Tanaka, M. Uenishi, M. Kimura, T. Okamoto, N. Hamada, Nature **2002**, 418, 164.

[3] C. Lin, J. B. Jang, L. Zhang, E. A. Stach, R. J. Gorte, ACS Catal. **2018**, 8, 7679.

[4] M. B. Katz, S. Zhang, Y. Duan, H. Wang, M. Fang, K. Zhang, B. Li, G. W. Graham, X. Pan, J. Catal. **2012**, 293, 145.

[5] Q. Ma, F. Tietz, D. Stöver, Solid State Ionics **2011**, 192, 535.

[6] Y. Li, W. Zhang, Y. Zheng, J. Chen, B. Yu, Y. Chen, M. Liu, Chem. Soc. Rev. **2017**, 46, 6345.

[7] D. Neagu, T. S. Oh, D. N. Miller, H. Menard, S. M. Bukhari, S. R. Gamble, R. J. Gorte, J. M. Vohs, J. T. S. Irvine, Nat Commun **2015**, 6, 8120.

[8] W. Kobsiriphat, B. D. Madsen, Y. Wang, M. Shah, L. D. Marks, S. A. Barnett, J. Electrochem. Soc. **2010**, 157, B279.

[9] O. Kwon, S. Sengodan, K. Kim, G. Kim, H. Y. Jeong, J. Shin, Y.-W. Ju, J. W. Han, G. Kim, Nat. Commun. **2017**, 8, 15967.

[10] S. Sengodan, Y. Ju, O. Kwon, A. Jun, H. Y. Jeong, T. Ishihara, J. Shin, G. Kim, ACS Sustain. Chem. Eng. **2017**, 5, 9207.

[11] C. Yang, J. Li, Y. Lin, J. Liu, F. Chen, M. Liu, Nano Energy **2015**, 11, 704.

[12] Z. Du, H. Zhao, S. Yi, Q. Xia, Y. Gong, Y. Zhang, X. Cheng, Y. Li, L. Gu, K. Świerczek, ACS Nano **2016**, 10, 8660.

[13] C. Yang, Z. Yang, C. Jin, G. Xiao, F. Chen, M. Han, Adv. Mater. **2012**, 24, 1439.

[14] D. Neagu, J. T. S. Irvine, Chem. Mater. **2010**, 22, 5042.

[15] G. Tsekouras, D. Neagu, J. T. S. Irvine, Energy Environ. Sci. **2013**, 6, 256.

[16] E. Y. Konysheva, X. Xu, J. T. S. Irvine, Adv. Mater. **2012**, 24, 528.

[17] R. Schöllhorn, Angew. Chemie Int. Ed. English **1980**, 19, 983.

[18] A. Clearfield, Chem. Rev. **1988**, 88, 125.

[19] S. Choi, S. Yoo, J. Kim, S. Park, A. Jun, S. Sengodan, J. Kim, J. Shin, H. Y. Jeong, Y. Choi, G. Kim, M. Liu, Sci. Rep. **2013**, 3, 2426.

[20] R. D. Shannon, Acta Cryst. **1976**, A32, 751.

[21] S. Kim, C. Kim, J. H. Lee, J. Shin, T.-H. Lim, G. Kim, Electrochim. Acta **2017**, 225, 399.

[22] D. Ding, X. Li, S. Y. Lai, K. Gerdes, M. Liu, Energy Environ. Sci. **2014**, 7, 552.

[23] H. Ding, Z. Tao, S. Liu, Y. Yang, J. Power Sources **2016**, 327, 573.

[24] C. Yang, J. Li, Y. Lin, J. Liu, F. Chen, M. Liu, Nano Energy **2015**, 11, 704.

[25] K. Sun, J. Liu, J. Feng, H. Yuan, M. He, C. Xu, Z. Wang, W. Sun, J. Qiao, J. Power Sources **2017**, 365, 109.

[26] Y. S. Chung, T. Kim, T. H. Shin, H. Yoon, S. Park, N. M. Sammes, W. B. Kim, J. S. Chung, J.

ULSAN NATIONAL INSTITUTE OF SCIENCE AND TECHNOLOGY

Mater. Chem. A **2017**, 5, 6437.

[27] T. Zhu, H. E. Troiani, L. V. Mogni, M. Han, S. A. Barnett, Joule **2018**, 2, 478.

[28] R. Bouarab, O. Akdim, A. Auroux, O. Cherifi, C. Mirodatos, Appl. Catal. A Gen. **2004**, 264, 161.

[29] Z. Bian, S. Das, M. H. Wai, P. Hongmanorom, S. Kawi, ChemPhysChem **2017**, 18, 3117.

[30] S. Joo, J. Kim, J. Shin, T.-H. Lim, G. Kim, J. Electrochem. Soc. **2016**, 163, F1489.

[31] G. Kresse, J. Furthmuller, Phys. Rev. B **1996**, 54, 11169.

[32] G. Kresse, J. Hafner, J. Phys. Condens. Matter **1994**, 6, 8245.

[33] M. Perdew, J. P., Burke, K. & Ernzerhof, Phys. Rev. Lett. **1996**, 77, 3865.

[34] H. J. Monkhorst, J. D. Pack, Phys. Rev. B **1976**, 13, 5188.

[35] T. Wan, A. Zhu, Y. Guo, C. Wang, S. Huang, H. Chen, G. Yang, W. Wang, Z. Shao, J. Power Sources **2017**, 348, 9.

[36] O. Kwon, K. Kim, S. Joo, H. Y. Jeong, J. Shin, J. W. Han, S. Sengodan, G. Kim, J. Mater. Chem. A **2018**, 6, 15947.

ULSAN NATIONAL INSTITUTE OF SCIENCE AND TECHNOLOGY

Chapter 4 Ni-Fe Bimetallic Nanocatalysts Produced by Topotactic Exsolution in Fe deposited $PrBaMn_{1.7}Ni_{0.3}O_{5+\delta}$ for Dry Reforming of Methane

This chapter has been published.

Reproduced with permission from S. Joo, O. Kwon, S. Kim, H. Y. Jeong, G. Kim, J. Electrochem. Soc. 2020, 167, 064518.

4.1. Introduction

As a new era of the gas economy has begun with the recent development of resources such as shale gas and methane hydrate, the natural gas reforming technology that can produce hydrogen in large quantities has brought into the spotlight.[1]-[3] Methane gas, a major component of natural gas, can be converted into syngas (a mixture of hydrogen and carbon monoxide) by reforming reactions (e.g., steam/dry reforming reaction of methane[4]-[7], partial oxidation[8]-[11], and autothermal reforming[12]). In particular, dry reforming of methane (DRM) has been actively researched since it can be a direct route for producing syngas, which can be the starting point for the synthesis of methanol, ammonia, and Fischer-Tropch reaction.[13] Ni-based supported catalysts have been widely used in DRM reactions, but the deactivation of catalysts due to coke formation or sintering has slowed their practical industrial applications.

Among various methods[14], exsolution can be an effective way to avoid these limitations due to their excellent carbon coking resistance and sintering resistance.[15]-[18] In detail, exsolution refers to the formation of nanocatalysts on the oxide surface by releasing cations doped in the support oxide in reducing condition. The resulting nanocatalysts are able to possess strong metal-support interactions because they are ‘embedded’ on the surface, which is advantageous in the durability compared to conventional synthesizing methods such as wet impregnation or vapor deposition.[17], [19] Recently, the use of topotactic ion exchange has been reported as a way to facilitate the exsolution phenomenon along with producing alloy catalysts.[5] In this way, the complete exsolution of metal cations is achievable without leaving cation defects in the host lattice, thereby maximizing the exsolution capability while maintaining the overall structural properties of the parent metal oxide.

ULSAN NATIONAL INSTITUTE OF
SCIENCE AND TECHNOLOGY

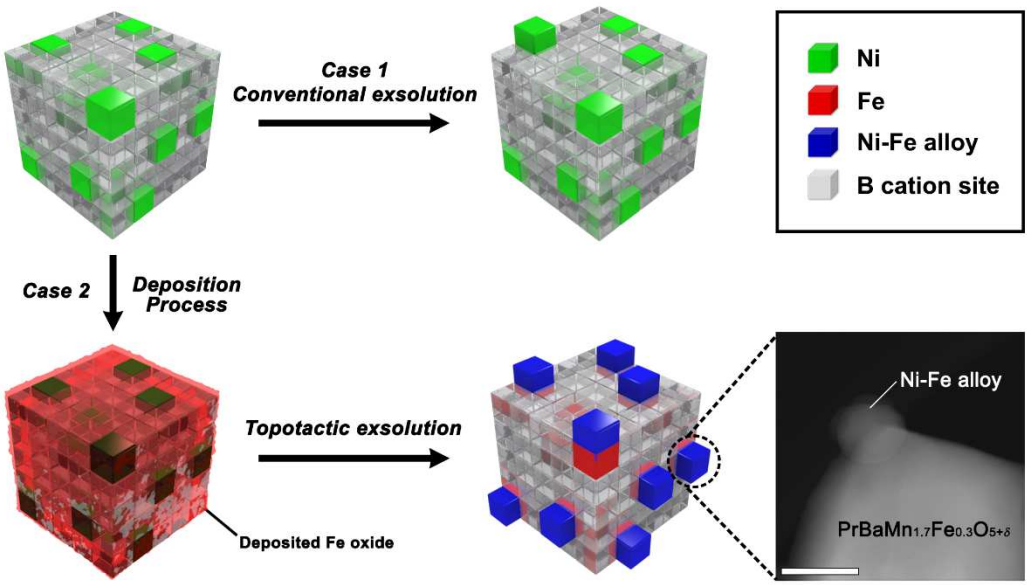

Figure 4-1 Schematic of the process for conventional exsolution and topotactic exsolution; scale bar 50 nm.

Meanwhile, a method of altering the nature of the catalyst by introducing a second metal to Ni has been proposed as another approach to mitigate coking.[20]-[22] The integration of nickel with other metals can easily change surface properties to achieve better catalytic performance. Although noble metals (*e.g.*, Pt[23], Ru[24], [25], Pd[26], Ir[24], [25], *etc*.) appear an attractive choice of material options as second metals with higher activity and better carbon resistance than Ni, they suffer from their high price and limited availability restricting a large-scale industrial use. Apart from noble metals, Fe can be a suitable choice as a second metal, as it combines good redox properties with Fe-Ni alloy formation upon intimate interaction between Fe and Ni.[25], [27], [28]

Herein, we report the behavior of a highly efficient, stable, and inexpensive exsolved Ni-Fe nanocatalysts on the layered perovskite $PrBaMn_{1.7}Ni_{0.3}O_{5+\delta}$ (PBMNi) using topotactic exsolution, where Fe (Fe^{2+}/Fe^{3+}) was adopted as the guest cation. As previously reported[18], Ni has a higher co-segregation energy than Fe, so it tends to exsolve toward the surface. Therefore, when the guest cation of Fe is employed on the surface of PBMNi where Ni is used as the host cation of B-site, the host PBMNi can be converted into PBMFe through the process of exchanging their sites (Figure 4-1). In other words, with the introduction of Fe, Ni-Fe can be easily created, and more nanoparticles latent beneath the surface can be exsolved to the surface. The Ni-Fe alloy nanoparticles decorated on the PBMNi oxide surface show a higher catalytic activity towards dry reforming of methane with enhanced stability (>100 hrs at 800 ^{o}C).

ULSAN NATIONAL INSTITUTE OF SCIENCE AND TECHNOLOGY

4.2. Experimental

4.2.1. Synthesis of catalysts

Table 4-1 Nomenclature for the compounds based on the Fe infiltrated PBMNi system

Compound	Abbreviations
$PrBaMn_2O_{5+\delta}$	PBM
$PrBaMn_{1.7}Ni_{0.3}O_{5+\delta}$	PBMNi
$PrBaMn_{1.7}Ni_{0.3}O_{5+\delta}$ + 12 wt. % infiltration of Fe	PBMNi-12-Fe
$PrBaMn_{1.7}Fe_{0.3}O_{5+\delta}$ + 12 wt. % infiltration of Fe	PBMFe-12-Fe

wt. %: weight percent to the anode

$Pr_{0.5}Ba_{0.5}Mn_{0.85}Ni_{0.15}O_{3-\delta}$ was prepared by the Pechini synthesis. The proper amounts of $Pr(NO_3)_3 \cdot 6H_2O$ (Aldrich, 99.9%, metal basis), $Ba(NO_3)_2$ (Aldrich, 99+%), $Mn(NO_3)_2 \cdot 4H_2O$ (Aldrich, 98%), and $Ni(NO_3)_2 \cdot 6H_2O$ were dissolved in distilled water to get stoichiometry. After complete dissolution, appropriate amounts of ethylene glycol and citric acid were added as complexing agents. This solution was thoroughly mixed with a magnetic stirrer and then combusted through the gelation process. The remaining powder was collected, followed by calcination at 600 ^oC for 4 hours to remove organic residue. The chemical composition of the samples and their abbreviations are given in Table 4-1 Nomenclature for the compounds based on the Fe infiltrated PBMNi system

4.2.2. Infiltration

The deposition for topotactic exsolution was performed by infiltration technique. The appropriate amounts of $Fe(NO_3)_3 \cdot 9H_2O$ (Aldrich, 98 + %) and citric acid were dissolved in distilled water to make a concentration of 0.7 M. The precursor solution was infiltrated in porous $Pr_{0.5}Ba_{0.5}Mn_{0.85}Ni_{0.15}O_{3-\delta}$ and calcined for 4 hours at 450 ^oC in air. The infiltration process was repeated until the desired weight percent.

4.2.3. Exsolution characterization

To compare the exsolution phenomenon, pre-calcined PBMNi was fired at 950 °C in air for 4 h. The sintered PBMNi was infiltrated with Fe precursor solution and reduced at 850 °C in H_2 atmosphere (with 3% H_2O) for 4 h. The crystal structures of the samples were identified by XRD (Bruker, D8 Advance, Cu Ka radiation, 40 kV, 40 mA). The morphologies of materials were investigated using SEM (FEI, Nova Nano 230 FE-SEM). TEM images were obtained with a JEOL JEM 2100F with a probe forming (STEM) Cs (spherical aberration) corrector at 200 kV. N_2 adsorption and desorption isotherms measurement were carried out at – 196 ^oC (BELSORP-Mini II, BEL Co.) to evaluate the specific surface

ULSAN NATIONAL INSTITUTE OF SCIENCE AND TECHNOLOGY

area. The specific surface area of the catalysts was calculated from the N_2 adsorption and desorption isotherms results by the BET method.

4.2.4. Catalytic activity of DRM

Catalytic activity for DRM was evaluated through gas chromatography (GC) (Agilent 7820 A GC instrument) with a thermal conductivity detector (TCD) and a packed column (Agilent carboxen 1000). The gas used for GC measurement was controlled using a mass flow controller (Atovac GMC1200) and the exact volume value of gas was calibrated through a bubble flow meter. The 0.2 g of sample powder (950 °C sintered in air for 4 h) was prepared and packed in the middle of the quartz tube reactor using glass wool. The sample powder was *in-situ* reduced at 900 °C for 30 min while blowing humified H_2 (3% H_2O) gas in a quartz tube reactor. After the reduction, the quartz tube was purged for 1 h with He gas to remove residual H_2, then CO_2, CH_4, and He were inserted with a ratio of 20:20:60 ml min^{-1}, respectively. The dry reforming reaction is shown as below, CO_2 conversion and CO selectivity were calculated using the following equations[4], [29]:

$$CH_4 + CO_2 \leftrightarrow 2CO + 2H_2 \ (\Delta H^0_{298K} = 247\ kJ/mol)$$

$$CO_2\ \text{conversion} = \frac{[CO_2]_{consumed}}{[CO_2]_{feed}} \times 100\% = \frac{[CO]_{detect}}{[CO]_{detect} + 2[CO_2]_{detect}} \times 100\%$$

$$CO\ \text{selectivity} = \frac{[CO]_{detect}}{[CO]_{detect} + [CO_2]_{detect}} \times 100\%$$

4.2.5. Fabrication of fuel cells

Commercial electrolyte powders, $La_{0.9}Sr_{0.1}Ga_{0.8}Mg_{0.2}O_{3-\delta}$ (LSGM, 99.9% Kceracell), was pressed into a pellet of 0.9 g and sintered at 1475 °C. After that, the pellet was polished to about 250 μm. $La_{0.4}Ce_{0.6}O_{2-\delta}$ was used as a buffer layer between anode and electrolyte to prevent ionic inter-diffusion. Anode powder PBMNi was mixed with an organic binder (Heraeus V006) (1:2 weight ratio) to make slurry ink. Cathode powders composed of $PrBa_{0.5}Sr_{0.5}Co_{1.5}Fe_{0.5}O_{5+\delta}$ (PBSCF)-$Ce_{0.9}Gd_{0.1}O_{2-\delta}$ (at a weight ratio of 60:40) were mixed with an organic binder (1:1.2 weight ratio) for a cathode slurry ink. These electrode inks were screen-printed on the LSGM electrolyte pellet to produce a configuration of PBMNi | LDC | LSGM | PBSCF-GDC, which was followed by sintering at 950 °C in the air for 4h. The Fe precursor solution was infiltrated on PBMNi after sintering. For the electrochemical tests, Ag wires were fixed to both electrodes using Ag paste as current collectors and the cell was sealed on an alumina tube using a ceramic adhesive (Ceramabond 552, Aremco). I-V polarization curves were measured using a BioLogic Potentiostat.

ULSAN NATIONAL INSTITUTE OF SCIENCE AND TECHNOLOGY

4.3. Result and discussion

4.3.1. XRD

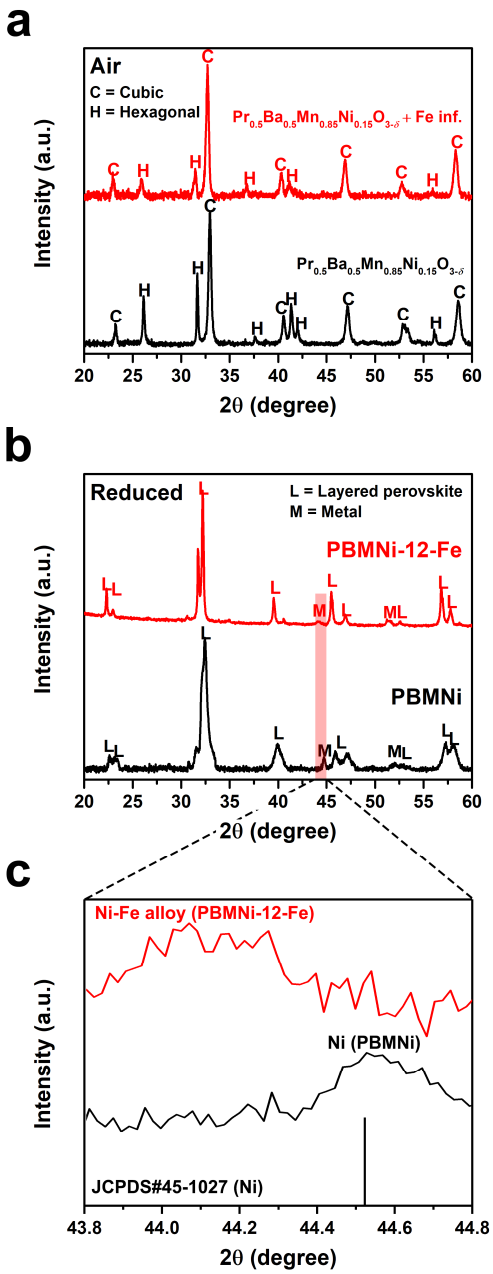

Figure 4-2 X-ray diffraction patterns of (a) $Pr_{0.5}Ba_{0.5}Mn_{0.85}Ni_{0.15}O_{3-}$, Fe infiltrated $Pr_{0.5}Ba_{0.5}Mn_{0.85}Ni_{0.15}O_{3-\delta}$ before reduction, (b) PBMNi, PBMNi-12-Fe after reduction, and (c) magnified metal peaks for PBMNi and PBMNi-12-Fe.

In order to investigate the structural information, X-ray diffraction was analyzed before and after the reduction of the samples. As shown in Figure 4-2a, PBMNi sintered at 950 ^{o}C for 4 hours exhibits simple perovskite of mixed cubic and hexagonal phases withoutl the secondary phase. The Fe infiltrated PBMNi does not show any significant difference compared to the pristine PBMNi. This is presumably because the amount of infiltrated Fe is not considerable compared to that of pristine PBMNi. Figure

ULSAN NATIONAL INSTITUTE OF SCIENCE AND TECHNOLOGY

4-2b shows the diffraction pattern of PBMNi and PBMNi-12-Fe samples after reduction. In a reducing atmosphere, the sample undergoes a phase transition from simple perovskite to layered perovskite while Ni of the host lattice exsolves to the surface of the host material. As shown in Figure 4-2c, the peak of exsolved Ni metal for PBMNi was observed at 2θ = 44.52° (JCPDS card#45-1027). In the case of PBMNi-12-Fe in which Fe was infiltrated, the peak for the exsolved metal is lower-angle shifted (44.52° for PBMNi and 44.07° for PBMNi-12-Fe) due to the formation of Ni-Fe alloy, which is attributed to the dissolution of Fe into the Ni lattice.[3] The diffraction pattern of PBMNi-12-Fe is similar to that of PBMCo-12-Fe[3] as previously reported. This can be explained by the transition of the $Pa_{0.5}Br_{0.5}M_{0.85}Ni_{0.15}O_{3-\delta}$ to $PrBaMn_{1.7}Ni_{0.3-y}Fe_yO_{5+\delta}$ as the cation exchange proceeds between Ni and Fe (Eq.1). When Ni of B site is replaced with Fe, the parent material is changed to $PrBaMn_{1.7}Fe_{0.3}O_{5+\delta}$, whose peak splitting of the XRD pattern is the characteristic of PBMFe, which is distinguished from that of PBMNi. These results demonstrate that topotactic exchange also occurs when Fe is introduced

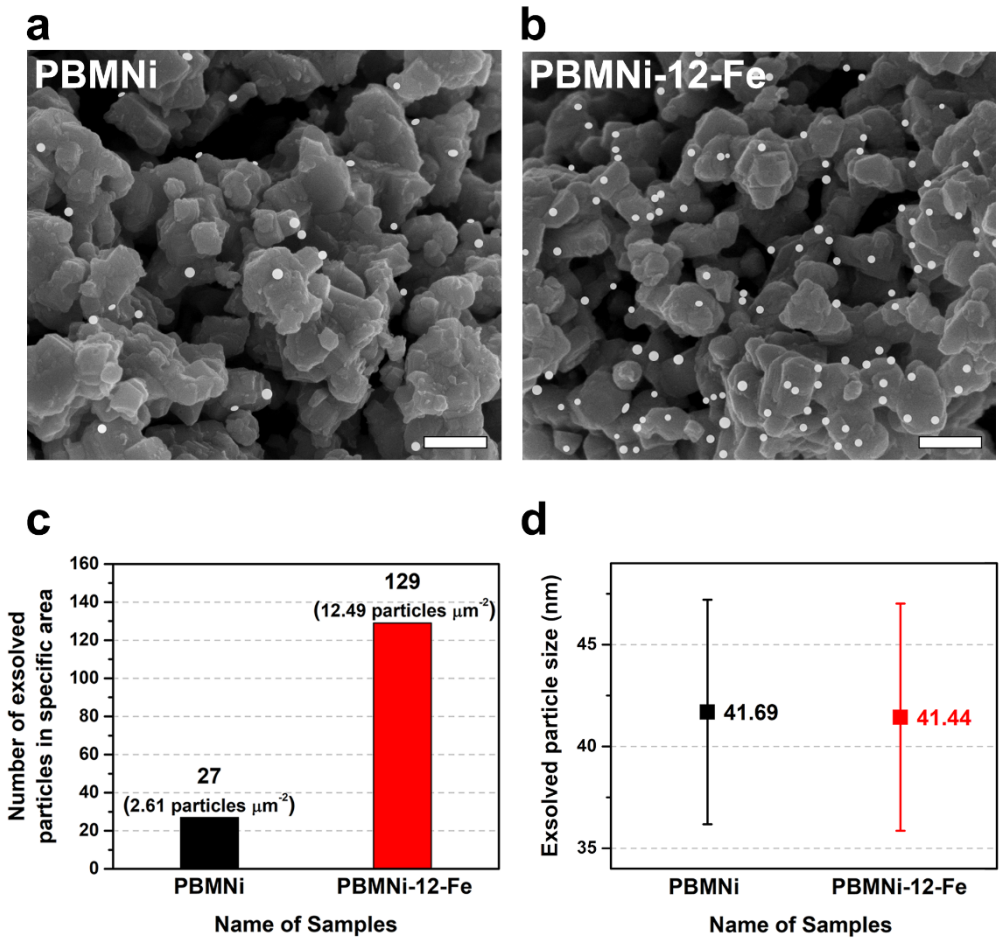

Figure 4-3 Scanning electron microscopy images and the correlation between the deposition of Fe and the particle population/size. SEM images of (a) PBMNi and (b) PBMNi-12-Fe; scale bars are 500 nm (Exsolved nanoparticles were colored in white.). (c) Exsolved particle population for PBMNi and PBMNi-12-Fe. (d) Particle size distribution for PBMNi and PBMNi-12-Fe.

ULSAN NATIONAL INSTITUTE OF SCIENCE AND TECHNOLOGY

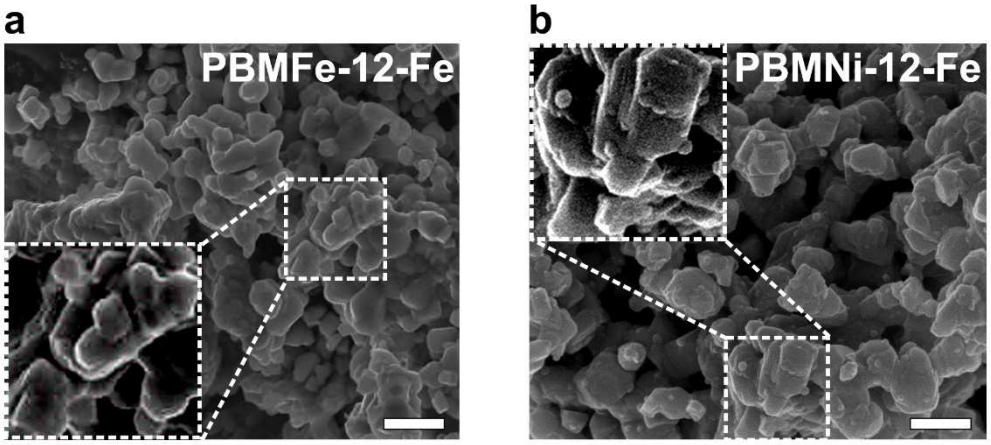

Figure 4-4 Scanning electron microscopy images of (a) PBMFe-12-Fe and (b) PBMNi-12-Fe. The morphological image of the exsolved surface was compared to the surface of the sample without exsolution.

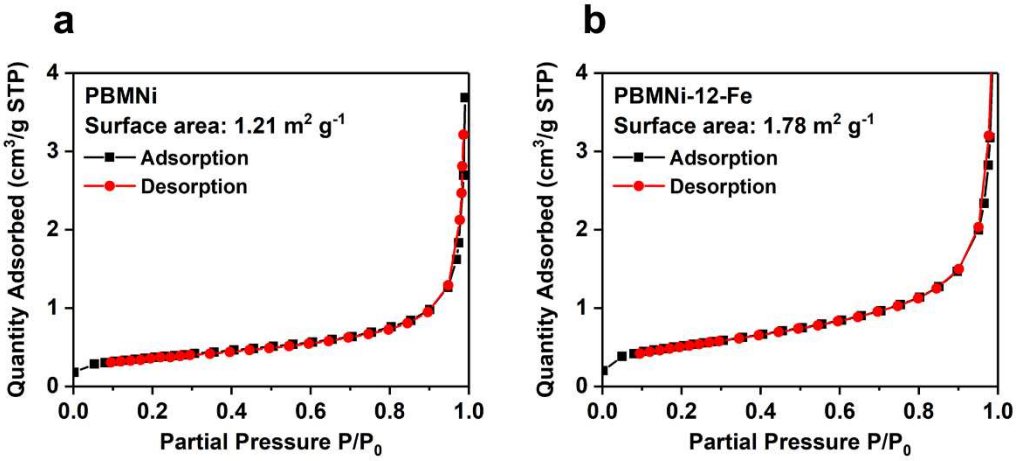

Figure 4-5 N_2 adsorption and desorption isotherms measurement of (a) PBMNi and (b) PBMNi-12-Fe.

to Ni, as the case of the host Co previously reported.

$$Pr_{0.5}Ba_{0.5}Mn_{0.85}Ni_{0.15}O_{3-\delta} + Fe_2O_3(\text{deposition}) \xrightarrow{\text{reducing}} PrBaMn_{1.7}Ni_{0.3-y}Fe_yO_{5+\delta} + y\text{Ni} - \text{Fe (exsolution and formation of alloy)} \quad (1)$$

4.3.2. SEM

To observe the effect of topotactic exsolution by the deposition of Fe, we compared the population of exsolved nanoparticles of PBMNi and PBMNi-12-Fe through scanning electron microscopy (SEM). The surface SEM images of PBMNi and PBMNi-12-Fe are shown in Figure 4-3a-b. The micrographs show that the spherical exsolved nanoparticles are evenly distributed on the surface of the parent oxide. As expected according to the previously reported topotactic exsolution, the Fe-deposited PBMNi

ULSAN NATIONAL INSTITUTE OF SCIENCE AND TECHNOLOGY

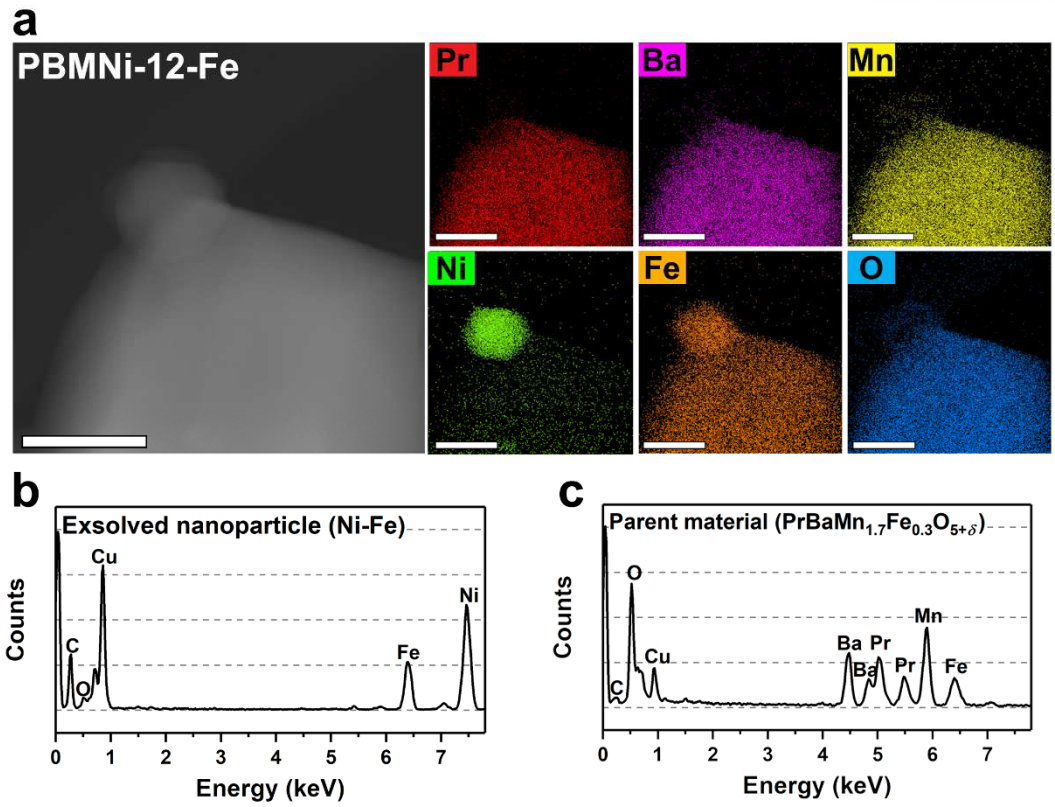

Figure 4-6 Transmission electron microscopy of exsolved particles and parent material. (a) HAADF scanning Transmission electron microscopy image and EDS elemental map of Pr, Ba, Mn, Ni, Fe, and O for exsolved particle and parent oxide of PBMNi-12-Fe sample; scale bar 50 nm. EDS spectrum of (b) the exsolved nanoparticles and (c) the parent material.

(PBMNi-12-Fe) exhibits a larger number of exsolved particles than PBMNi, verifying that the topotactic exsolution developed. On the other hand, the exsolved particle was barely observed in the case of PBMFe-12-Fe where the same amount of Fe was deposited in PBMFe. (Figure 4-4) To get a more quantitative comparison, image analysis was performed using ImageJ software. In the case of PBMNi, only 2.61 particles per μm^2 were exsolved, whereas 12.49 particles per μm^2 were exsolved for PBMNi-12-Fe. In other words, the use of topotactic exsolution has an effect of an increase in the number of particles by more than 4-fold. In general, materials composed of nanoparticles have a relatively larger surface area compared to materials of the same volume composed of bigger particles. Therefore, the increased particle number leads to an increase in surface area, which was confirmed by Brunauer-Emmett-Teller (BET) analysis (Figure 4-5). The values of specific surface area for PBMNi and PBMNi-12-Fe were found to be 1.21 and 1.78 $m^2 g^{-1}$, respectively. Moreover, topotactic exsolution affects the number of particles, but barely affects the size of exsolved particles. As shown in Figure 4-3d, the average size of exsolved particles does not differ significantly between the two samples, indicating that topotactic exsolution is able to produce regular and uniformly dispersed nanoparticles.

ULSAN NATIONAL INSTITUTE OF SCIENCE AND TECHNOLOGY

4.3.3. TEM

To confirm the component of the layered perovskite with exsolved nanoparticles, we observed the samples using transmission electron microscopy (TEM). As shown in the high-angle annular dark field (HAADF) scanning TEM image of PBMNi-12-Fe in Figure 4-6, particles of about 40 nm are exsolved from the parent oxide. Exsolved particles appear to an alloy composed of Ni-Fe based on energy dispersive spectroscopy (EDS) analysis. Apparently, most of Ni appears to have been exsolved from the parent oxide near the surface while Fe not only forms exsolved particles but also parent oxides, which suggests that the intercalation of Fe into Ni site occurs. According to the previous report[5], partial disappearance of Ni in the parent lattice is the result of topotactic exsolution where Ni and Fe change their places. Also, the XRD shows that the peaks around 22 ^{o} change before and after the exchange. The peaks near 22 ^{o} correspond to (200), which are 22.53 ^{o} and 22.30 ^{o} for PBMNi and PBMNi-12-Fe, respectively. The peak shift is due to the lattice expansion attributed to the intercalation of Fe. In other words, if smaller Ni ions (Ni^{2+} (r=0.690 Å) or Ni^{3+} (r=0.560 Å)) are replaced with larger Fe ions (Fe^{2+} (r=0.780 Å) or Fe^{3+} (r=0.645 Å)), the overall average lattice size increases.[5], [30]

Additionally, according to the EDS line spectrum, the nanoparticle is composed of Ni and Fe. The Fe/Ni molar ratio was found to be about 0.47. In spite of a significant amount of deposited Fe, Ni occupies more ratio in the nanoparticle than Fe, and it can be seen that the deposited Fe diffuses into the parent oxide. This can be further confirmed by the EDS line spectrum of the parent oxide, where the Ni signal was hardly observed in the parent oxide. Therefore, it can be concluded the most of Ni in the parent is exsolved to the surface through the exchange with Fe. In the previous study[5], the parent oxide of $PrBaMn_{1.7}Co_{0.3}O_{5+\delta}$ is reconstructed into $PrBaMn_{1.7}Fe_{0.3}O_{5+\delta}$ after the topotactic exchange. Interestingly, the EDS spectrum of $PrBaMn_{1.7}Ni_{0.3}O_{5+\delta}$ after the exchange is identical to that of $PrBaMn_{1.7}Co_{0.3}O_{5+\delta}$, evidencing PBMNi has a parent oxide of $PrBaMn_{1.7}Fe_{0.3}O_{5+\delta}$ as a result of the topotactic exchange.

ULSAN NATIONAL INSTITUTE OF SCIENCE AND TECHNOLOGY

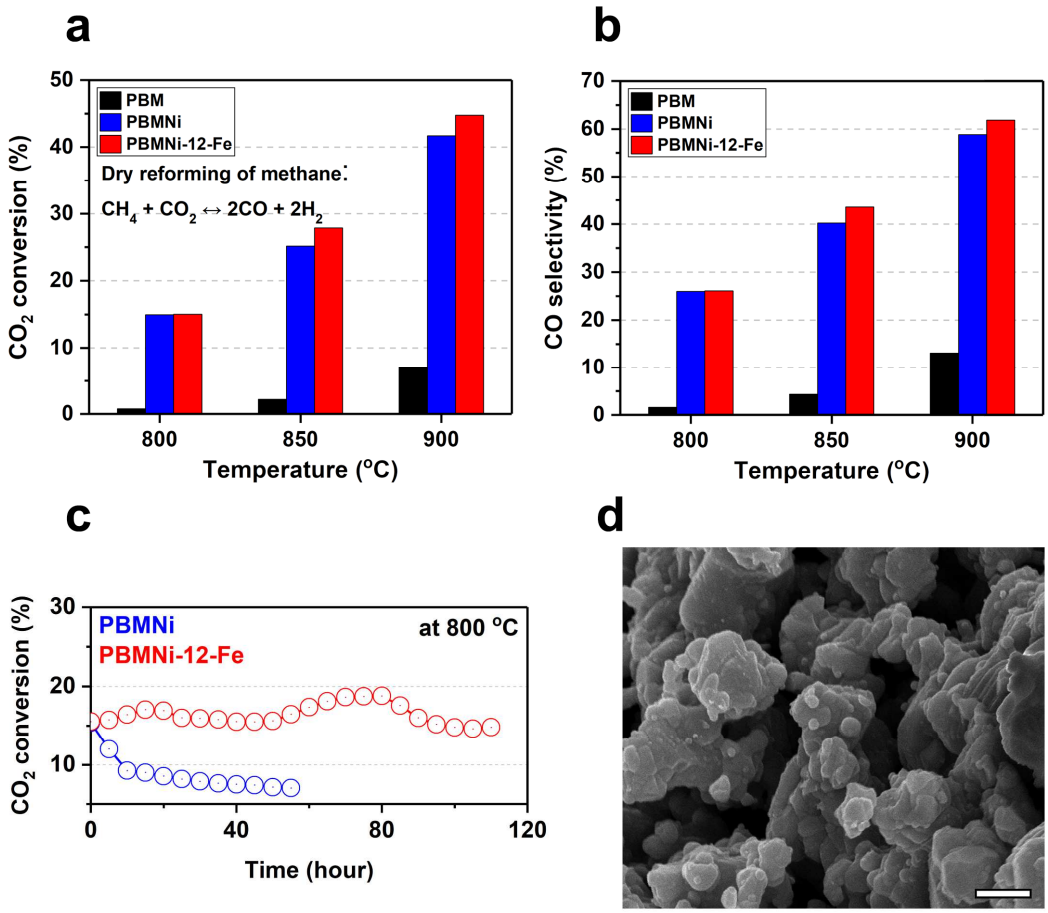

Figure 4-7 Catalytic properties. (a) Conversion of CO_2 for PBM, PBMNi, and PBMNi-12-Fe. (b) CO selectivity for PBM, PBMNi, and PBMNi-12-Fe. (c) Time-dependence of CO_2 conversion for the PBMNi and PBMNi-12-Fe in dry reforming of methane at 800 °C. (d) SEM image of the PBMNi-12-Fe sample after 100 hours of continuous DRM test; scale bar 500 nm.

4.3.4. Catalytic property

The catalytic activity of PBMNi and PBMNi-12-Fe samples for dry reforming of methane (DRM) was evaluated using a quartz tube reactor. The measurements were performed at 50 °C intervals on cooling from 900 to 800 °C. At 900 °C, the CO_2 conversion value of the PBMNi-12-Fe sample is about 45 %, which is 6-fold higher than 7.02 % of PBM. However, it is slightly higher than that of PBMNi, which is assumed to be due to the high catalytic activity of Ni catalysts for DRM. At 800 °C, the CO_2 conversion value of PBM was 0.81 % with little catalytic activity, while PBMNi-12-Fe shows remarkably increased catalytic activity of about 15 %, which is a more than 18-fold enhancement. Moreover, the stability of the PBMNi-12-Fe sample under the DRM atmosphere was evaluated, and the performance was maintained above the initial value for more than 100 hours. The surface of PBMNi-12-Fe was observed after a continuous DRM test of 100 hours to investigate carbon coking resistance. As shown in Figure 4-7c, the growth of carbon was barely observed even after the long-term catalytic test, and it was confirmed that Ni-Fe alloy nanoparticles had excellent carbon coking resistance.

ULSAN NATIONAL INSTITUTE OF
SCIENCE AND TECHNOLOGY

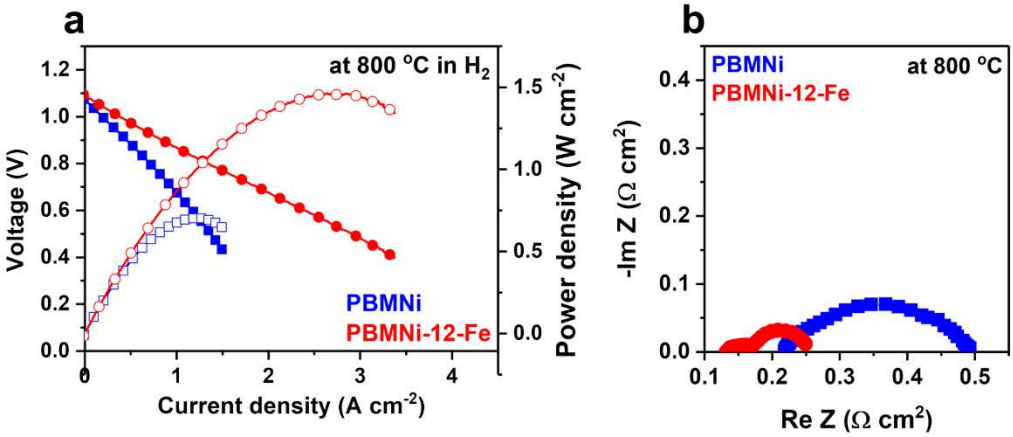

Figure 4-8 (a) I-V curve and power densities of the PBMNi and PBMNi-12-Fe in H_2 (3% H_2O), (b) Impedance spectra of PBMNi and PBMNi-12-Fe at 800 °C in H_2 (3% H_2O).

Additionally, the electrochemical performance of the fuel cell of the PBMNi-12-Fe sample was evaluated as an anode (Figure 4-8). The Fuel cell was composed of PBMNi-12-Fe | LDC | LSGM | PBSCF-GDC and tested using humidified H_2 (with 3% H_2O) as fuel and ambient air as the oxidant. The maximum power density of PBMNi-12-Fe is about 1.465 W cm^{-2} at 800 °C in a humidified H_2 atmosphere, and the electrochemical performance is more than doubled compared to that of PBMNi of 0.703 W cm^{-2}. This is consistent with the trend of electrochemical impedance spectroscopy (EIS) measurements, where the non-ohmic resistances for PBMNi and PBMNi-12-Fe were 0.254 and 0.117 Ω cm^2 at 800 °C in humidified H_2 atmosphere, respectively.

4.4. Conclusions

In summary, we have shown the synthesis of Ni-Fe bimetallic nanocatalysts using topotactic exsolution. When depositing Fe as a guest ion on PBMNi, Ni-Fe bimetallic catalyst can be generated by selectively exsolving Ni cation, and it can promote the formation of a larger number of exsolved particles. The spontaneous exchange between Ni and Fe ions converts PBMNi parent oxides into PBMFe according to XRD and XPS results, suggesting that topotactic exsolution has occurred. This results in increasing the number of exsolved particles by over four times while maintaining homogeneous particles. These nanoparticles have been found to exhibit about 18 times higher catalytic activity and stability over 100 hours at 800 °C compared to PBM samples without metal exsolution in DRM reaction.

ULSAN NATIONAL INSTITUTE OF SCIENCE AND TECHNOLOGY

References

[1] D. Ding, Y. Zhang, W. Wu, D. Chen, M. Liu, T. He, Energy Environ. Sci. **2018**, 11, 1710.

[2] J. W. Han, C. Kim, J. S. Park, H. Lee, ChemSusChem **2014**, 7, 451.

[3] L. S. Gangurde, G. S. J. Sturm, M. J. Valero-Romero, R. Mallada, J. Santamaria, A. I. Stankiewicz, G. D. Stefanidis, Chem. Eng. Process. - Process Intensif. **2018**, 127, 178.

[4] O. Kwon, K. Kim, S. Joo, H. Y. Jeong, J. Shin, J. W. Han, S. Sengodan, G. Kim, J. Mater. Chem. A **2018**, 6, 15947.

[5] S. Joo, O. Kwon, K. Kim, S. Kim, H. Kim, J. Shin, H. Y. Jeong, S. Sengodan, J. W. Han, G. Kim, Nat. Commun. **2019**, 10, 697.

[6] L. Lei, J. M. Keels, Z. Tao, J. Zhang, F. Chen, Appl. Energy 2018, 224, 280.

[7] J. L. Rogers, M. C. Mangarella, A. D. D'Amico, J. R. Gallagher, M. R. Dutzer, E. Stavitski, J. T. Miller, C. Sievers, ACS Catal. **2016**, 6, 5873.

[8] S. Sengodan, R. Lan, J. Humphreys, D. Du, W. Xu, H. Wang, S. Tao, Renew. Sustain. Energy Rev. **2018**, 82, 761.

[9] D. Lee, J. Myung, J. Tan, S.-H. Hyun, J. T. S. Irvine, J. Kim, J. Moon, J. Power Sources **2017**, 345, 30.

[10] H. Jiang, H. Wang, S. Werth, T. Schiestel, J. Caro, Angew. Chemie - Int. Ed. **2008**, 47, 9341.

[11] A. S. Yu, J. M. Vohs, R. J. Gorte, Energy Environ. Sci. **2014**, 7, 944.

[12] B. W. Kwon, J. H. Oh, G. S. Kim, S. P. Yoon, J. Han, S. W. Nam, H. C. Ham, Appl. Energy **2018**, 227, 213.

[13] P. M. Mortensen, I. Dybkjær, Appl. Catal. A Gen. **2015**, 495, 141.

[14] A. Abdulrasheed, A. A. Jalil, Y. Gambo, M. Ibrahim, H. U. Hambali, M. Y. Shahul Hamid, Renew. Sustain. Energy Rev. **2019**, 108, 175.

[15] D. Neagu, E. I. Papaioannou, W. K. W. Ramli, D. N. Miller, B. J. Murdoch, H. Ménard, A. Umar, A. J. Barlow, P. J. Cumpson, J. T. S. Irvine, I. S. Metcalfe, Nat. Commun. **2017**, 8, 1855.

[16] J. Myung, D. Neagu, D. N. Miller, J. T. S. Irvine, Nature **2016**, 537, 528.

[17] D. Neagu, T. S. Oh, D. N. Miller, H. Menard, S. M. Bukhari, S. R. Gamble, R. J. Gorte, J. M. Vohs, J. T. S. Irvine, Nat Commun **2015**, 6, 8120.

[18] O. Kwon, S. Sengodan, K. Kim, G. Kim, H. Y. Jeong, J. Shin, Y.-W. Ju, J. W. Han, G. Kim, Nat. Commun. **2017**, 8, 15967.

[19] B. Hua, M. Li, Y. F. Sun, J. H. Li, J. L. Luo, ChemSusChem **2017**, 10, 3333.

[20] C. Yang, J. Li, Y. Lin, J. Liu, F. Chen, M. Liu, Nano Energy **2015**, 11, 704.

[21] Y.-F. Sun, J.-H. Li, L. Cui, B. Hua, S.-H. Cui, J. Li, J.-L. Luo, Nanoscale **2015**, 7, 11173.

[22] C. Yang, Z. Yang, C. Jin, G. Xiao, F. Chen, M. Han, Adv. Mater. **2012**, 24, 1439.

ULSAN NATIONAL INSTITUTE OF SCIENCE AND TECHNOLOGY

[23] T. D. Gould, M. M. Montemore, A. M. Lubers, L. D. Ellis, A. W. Weimer, J. L. Falconer, J. W. Medlin, Appl. Catal. A Gen. **2015**, 492, 107.

[24] S. De, J. Zhang, R. Luque, N. Yan, Energy Environ. Sci. **2016**, 9, 3314.

[25] Z. Bian, S. Das, M. H. Wai, P. Hongmanorom, S. Kawi, ChemPhysChem **2017**, 18, 3117.

[26] J. Li, B. Wei, X. Yue, L. Zhe, ChemSusChem **2018**, 11, 2593.

[27] S. A. Theofanidis, V. V. Galvita, H. Poelman, G. B. Marin, ACS Catal. **2015**, 5, 3028.

[28] L. Wang, D. Li, M. Koike, S. Koso, Y. Nakagawa, Y. Xu, K. Tomishige, Appl. Catal. A Gen. **2011**, 392, 248.

[29] T. Wan, A. Zhu, Y. Guo, C. Wang, S. Huang, H. Chen, G. Yang, W. Wang, Z. Shao, J. Power Sources **2017**, 348, 9.

[30] R. D. Shannon, Acta Cryst. **1976**, A32, 751.

ULSAN NATIONAL INSTITUTE OF SCIENCE AND TECHNOLOGY

Chapter 5 Highly Active Dry Methane Reforming Catalysts with Boosted *in-situ* grown Ni-Fe Nanoparticles on Perovskite *via* Atomic Layer Deposition

This chapter has been published.

Reproduced with permission from S. Joo, A. Seong, O. Kwon, K. Kim, J. H. Lee, R. J. Gorte, J. M. Vohs, J. W. Han, G. Kim, Sci. Adv. 2020, 6, eabb1573. Reprinted with permission from AAAS.

5.1. Introduction

Supported metal catalysts have extensively used in the fields of catalysis, energy conversion, and energy storage (*e.g.*, dry reforming of methane), but catalyst deactivation due to agglomeration or coking restrains the catalyst lifetime and efficiency.[1]-[3] The exsolution of metal nanoparticles from the host oxide lattice to the surface has been the subject of extensive studies to overcome these difficulties.[4]-[7] The exsolution, called *in-situ* growth, offers solid and stable nanoparticles through the development that metal cations in the host oxide lattice (*e.g.*, perovskite oxides) are exsolved and anchored to the oxide surface in reducing conditions.[8]-[16]

Although *in-situ* grown nanocatalysts display the advantages of lower cost, higher time efficiency, higher thermal/chemical stability, and enhanced coking resistance compared to catalysts produced by more conventional methods (*e.g.*, wet infiltration or chemical vapor deposition), three major pitfalls have hampered their practical use and commercialization[17], [18]: (1) a limited solubility of the exsolving dopant (or catalytic) cations into the host lattice, (2) many of the dopant cations remain in the bulk so metal utilization is often low, and (3) a slow rate of particle generation.

A-site deficient (A/B<1) perovskites (ABO_3) have been used in an attempt to promote more exsolution of cations to the surface from the bulk by providing a driving force to trigger B-site exsolution.[19]-[21] However, a limited solubility, where only 6 mol% of the Ti^{4+} was replaced with the cations of interest to be exsolved (*e.g.*, $La_{0.52}Sr_{0.28}Ni_{0.06}Ti_{0.94}O_3$[20]) constrains the number of particles on the surface.[19], [20], [22] Exsolution using voltage-driven reduction[23] has been proposed as another strategy to improve the rate of exsolution and increase the population of nanoparticles on the surface; however, it is challenging to employ this method for high surface area materials. Recently, the use of topotactic ion exchange in exsolution (topotactic exsolution) was reported as a new route for promoting a larger number of exsolved cations.[24] In this case, however, the method *via* infiltration technique suffers from the difficulty to control the quantitative amount of catalyst and the need for a large amount of catalyst to wet the parent oxide, thus adding cost with respect to fabrication and materials.[25]

Therefore, for the ideal use of exsolution, the following requirements must be fulfilled: (1) the production of a larger population of surface particles and (2) a simple reduction procedure. Within the

ULSAN NATIONAL INSTITUTE OF SCIENCE AND TECHNOLOGY

framework of these criteria, the aim of our work is to meet these requirements by employing the topotactic exsolution concept where Fe guest cations deposited *via* atomic layer deposition (ALD) can be exchanged with Ni host cations in the A-site deficient perovskite, $La_{0.6}Sr_{0.2}Ti_{0.85}Ni_{0.15}O_{3-\delta}$. The lanthanum strontium titanates, well known highly stable catalyst support, are suitable for this case study with their ability to support a range of A-site deficiency and doping elements. Based on the topotactic exsolution we recently found, a larger number of exsolved particles emerge preferentially on the surface when Fe oxides are externally deposited.[24] Thus, deposited guest cation Fe could serve as a general driving force by means of exchanging with the host cation Ni. In this case, the diffusion rate of the deposited guest cation to the host lattice can be an important factor determining the rate of exsolution through the topotactic ion exchange.

A thin film layer prepared by ALD has been shown to provide a fast diffusion rate with high surface areas and a nano-scale control of the amount of deposition.[26] As such, ALD renders a uniform, highly quantitative layer of metal oxide every single step. Therefore, when the Fe guest cation is externally deposited *via* ALD, the topotactic ion exchange can be accelerated with the help of the fast diffusion rate of guest cation Fe[26], thereby producing a finely dispersed array of anchored alloy metal nanoparticles with the increased population density. We elucidate the mechanism of the enhanced exsolution *via* ALD revealed by density functional theory (DFT) calculations. Moreover, the as-exsolved particles exhibit high catalytic activity for the dry reforming of methane (DRM) process with no observable degradation in performance for more than 410 hours of continuous operation.

5.2. Experimental

5.2.1. Synthesis of perovskite materials

Table 5-1 Nomenclature for the compounds based on the Fe deposited LSTN system

Compound	Abbreviations
$La_{0.6}Sr_{0.2}Ti_{0.85}Ni_{0.15}O_{2.95}$ + reduction	LSTN
$La_{0.6}Sr_{0.2}Ti_{0.85}Ni_{0.15}O_{2.95}$ + 5 cycles of Fe_2O_3 deposition with ALD + reduction	LSTN-5C-Fe
$La_{0.6}Sr_{0.2}Ti_{0.85}Ni_{0.15}O_{2.95}$ + 10 cycles of Fe_2O_3 deposition with ALD + reduction	LSTN-10C-Fe
$La_{0.6}Sr_{0.2}Ti_{0.85}Ni_{0.15}O_{2.95}$ + 15 cycles of Fe_2O_3 deposition with ALD + reduction	LSTN-15C-Fe
$La_{0.6}Sr_{0.2}Ti_{0.85}Ni_{0.15}O_{2.95}$ + 20 cycles of Fe_2O_3 deposition with ALD + reduction	LSTN-20C-Fe
$La_{0.6}Sr_{0.2}Ti_{0.85}Ni_{0.15}O_{2.95}$ + 30 cycles of Fe_2O_3 deposition with ALD + reduction	LSTN-30C-Fe

1 cycle of deposition: exposing to Fe precursor for 360 s followed by oxidation to air.

All samples of the perovskite structure were synthesized by the Pechini sol-gel method[30]-[32]. The adequate amounts of $La(NO_3)_3.6H_2O$, $Sr(NO_3)_2$, and $Ni(NO_3)_2.6H_2O$ for stoichiometry were dissolved

ULSAN NATIONAL INSTITUTE OF SCIENCE AND TECHNOLOGY

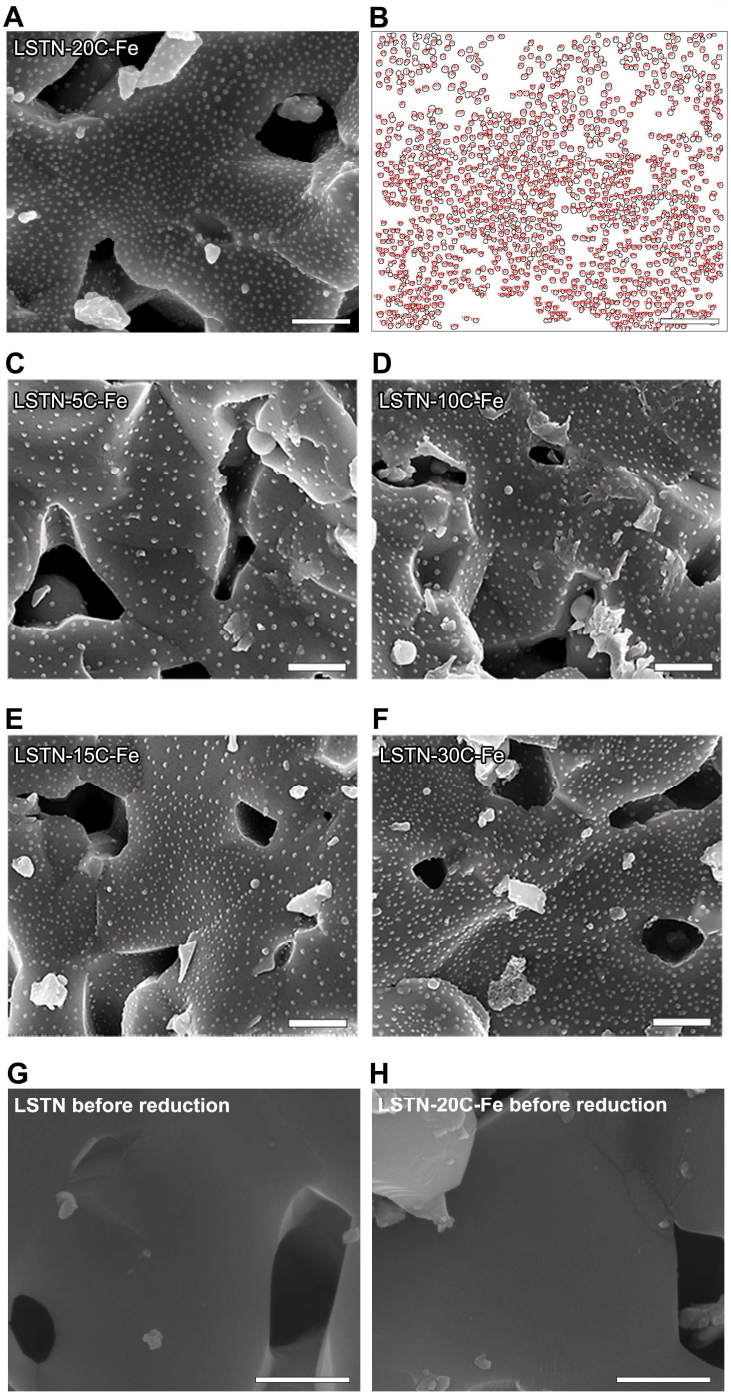

Figure 5-1 Particle count analysis on the surface. (A) SEM image corresponding to Fig. 1D. (B) exsolved nanoparticles mapping and contour extracted with ImageJ from Figure 5-1A; scale bars are 500 nm. SEM images of (C) LSTN-5C-Fe, (D) LSTN-10C-Fe, (E) LSTN-15C-Fe, and (F) LSTN-30C-Fe; scale bars are 500 nm. SEM images for (G) LSTN before reduction and (H) LSTN-20C-Fe before reduction; scale bars are 500 nm.

in distilled water. The adequate amount of $Ti[OCH(CH_3)_2]_4$ was dissolved in ethanol separately for ionization, and then ethylene glycol/citric acid as complexing agents were added to this solution. All solutions were mixed together and stirred overnight. A combustion process above 300 ^oC on a heating plate is followed to obtain fine powders. The powders were calcined at 600 ^oC for 4 hrs to remove

ULSAN NATIONAL INSTITUTE OF SCIENCE AND TECHNOLOGY

residual organics. The synthesized powders and their abbreviations are given in Table 5-1 Nomenclature for the compounds based on the Fe deposited LSTN system.

5.2.2. Atomic layer deposition of Fe oxide film

The iron-oxide films on LSTN were prepared by ALD using a home-built apparatus. The apparatus consists of quartz chambers containing precursor/substrate respectively, dosing lines, and valves connecting the chambers. Each chamber was enclosed by individual ovens to allow separate temperature control. Also, a mechanical vacuum pump was used to evacuate the chambers, approximately 10^{-3} Torr.[26], [33]

The condition used for depositing the precursor, ferrocene ($Fe(Cp)_2$, Sigma-Aldrich), was adopted from previous publications.[28] After evacuating the $Fe(Cp)_2$ precursor chamber at room temperature, it was heated to 160 ^oC to produce a reasonable vapor pressure of $Fe(Cp)_2$. During the deposition cycles, the $Fe(Cp)_2$ vapor was introduced to the evacuated substrate chamber, which contained approximately 0.2 g of $La_{0.6}Sr_{0.2}Ti_{0.85}Ni_{0.15}O_{2.95}$. The $La_{0.6}Sr_{0.2}Ti_{0.85}Ni_{0.15}O_{2.95}$ substrate was exposed to the vapor of $Fe(Cp)_2$ multiple times at 350 ^oC for 360 s to confirm that the reaction with the surface was complete. Excess precursor in the substrate chamber was then removed by evacuation and the substrate was oxidized by exposing it to air for 300 s.

5.2.3. Exsolution characterization

In order to compare the number of exsolution particles varying with the cycles of Fe oxide deposition *via* ALD, $La_{0.6}Sr_{0.2}Ti_{0.85}Ni_{0.15}O_{2.95}$ and other perovskite oxides were sintered at 1200 ^oC as the substrates. After the deposition through ALD, all samples were reduced at 850 ^oC for 4 hrs in H_2 atmosphere (with 3% H_2O).

The elemental analysis of the LSTN-*x*C-Fe samples (x = 0, 5, 10, 15, 20, and 30) for individual elements were quantified by inductively coupled plasma optical emission spectrometry (ICP-OES). In the measurement, a Spectro Genesis spectrometer was used in conjunction with concentric nebulizer. For the ICP-OES process, all samples for analysis (~50 mg) was dissolved in a 16 mL solution of Aqua Regia for 4 hours at 200 ^oC. Then, the solution was distilled with a 5 wt% HNO_3 solution to attain appropriate concentration for the ICP analysis.

The crystal structures of samples were analyzed by XRD (Bruker, D8 Advance, Cu Ka radiation, 40 kV, 40mA). The surface morphologies of the material were observed through SEM (FEI, Nova Nano 230 FE-SEM). The number of particles on the oxide surface was evaluated by ImageJ software. In the selected SEM images with appropriate magnification, the contrast and sharpness were slightly adjusted. The adjusted image was outlined based on the contrast to count the number of particles and to calculate

ULSAN NATIONAL INSTITUTE OF
SCIENCE AND TECHNOLOGY

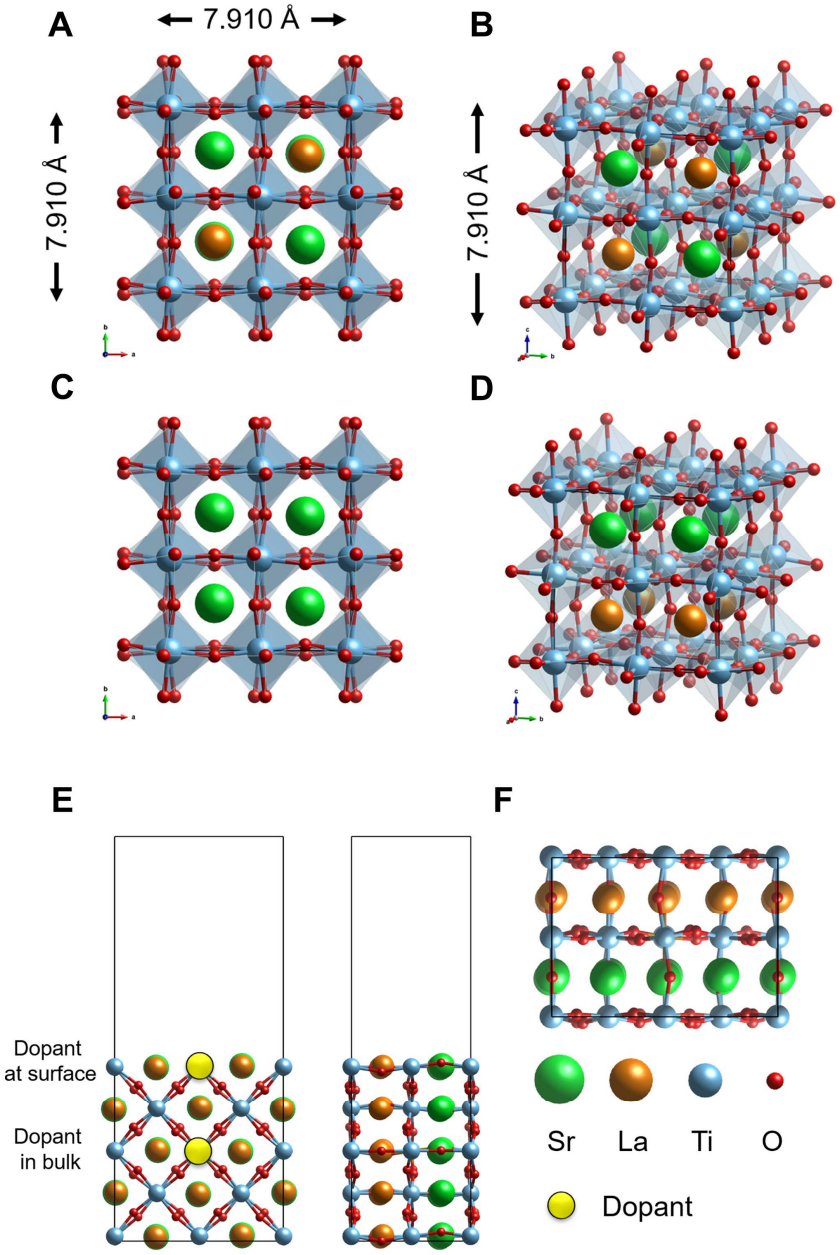

Figure 5-2 Optimized two possible cation configurations of bulk structures of $La_{0.5}Sr_{0.5}TiO_3$. (A, B) and (C, D) represent top and side views of uniformly and layer by layer cation distributions, respectively. (E) side and (F) top views of optimized surface structure of $La_{0.5}Sr_{0.5}TiO_3$(110) used for DFT calculations.

the size of particles (Figure 5-1B). XPS analysis was performed using ESCALAB 250XI from Thermo Fisher Scientific with a monochromatic A1-Ka (ultraviolet He1, He2) X-ray source. Cross-sectional samples for the TEM analysis were prepared by using a focused ion beam (FIB, Helios 450HP, FEI). TEM images were obtained with a FEI Titan (3) G2 60-300 with an imaging-forming Cs corrector at an accelerating voltage of 80 kV.

ULSAN NATIONAL INSTITUTE OF SCIENCE AND TECHNOLOGY

5.2.4. DFT

Density functional theory (DFT) calculations were performed using the Vienna ab initio Simulation Package (VASP).[34], [35] Exchange-correlation energies were treated by Perdew-Burke-Ernzerhof (PBE) functional based on generalized gradient approximation (GGA).[36] A plane wave expansion with a cutoff of 400 eV was used with a 4 × 2 × 1 Monkhorst-Pack *k*-point sampling of the Brillouin zone for all slab model calculations.[37] Gaussian smearing was used with a width of 0.05 eV to determine partial occupancies. Geometries were relaxed using a conjugate gradient algorithm until the forces on all unconstrained atoms were less than 0.03 eV/Å. In order to take into account for on-site Coulomb and exchange interactions, we used GGA+*U* schemes with the effective *U* values of 4.36, 4.0, and 6.0 for Ti, Fe, and Ni, respectively.[27] Based on our experimental observation, we constructed the pseudocubic $La_{0.5}Sr_{0.5}TiO_3$ with $a = b = c = 7.910$. Among the two possible cation configurations, we employed a more stable configuration (Figure 5-2), which had lower total energy by 0.19 eV.

To examine the segregation tendency of dopant elements, we constructed surface models by cleaving the DFT-optimized LST bulk along the (110) direction, which has been reported as the most preferred facet of B-site metal exsolution on $La_{0.5}Sr_{0.5}TiO_{3-\delta}$ based perovskites (Figure 5-2E-F). A nine layered LST slab was employed with the vacuum thickness of up to 17 Å. (Figure 5-2). The co-segregation energy of B-site metal (E_{seg}) with an oxygen vacancy is defined as below[27];

$$\mathrm{E_{co-seg}} = \mathrm{E_{(B-Vo)surf}} - \mathrm{E_{(B-Vo)bulk}}$$

where $E_{\mathrm{(B-Vo)surf}}$ and $E_{\mathrm{(B-Vo)bulk}}$ are the total energies of the system with B-site metal located at the surface and in the bulk with an oxygen vacancy, respectively. With our definition, more negative energy indicates easier exsolution.

5.2.5. Catalytic activity

The catalytic activity of the catalysts was assessed with a fixed-bed quartz-tube reactor with an internal diameter of about 10 mm. Approximately 0.2 g of sample powder was placed in the middle of the reactor. For the DRM test, the sample powder was reduced in situ in H_2 atmosphere (with 3% H_2O) at 900 °C for 1 hr. After the reduction, the remaining H_2 gas was purged with dry He, then the gas mixture of CO_2, CH_4, and He was introduced to the reactor with a ratio of 10:10:80 ml min^{-1}, respectively. Compositional analysis of the effluent gases from the reaction was performed using gas chromatography (GC) (Agilent 7820 A GC instrument) with a thermal conductivity detector (TCD) and a packed column (Agilent carboxen 1000). The gas flow was measured using a mass flow controller (Atovac GMC1200) and calibrated through a bubble flow meter for a more accurate ratio calculation. The DRM reaction is shown below, and the CH_4 reactivity and CH_4 conversion were obtained from the following equation:

$$\mathrm{CH_4 + CO_2} \leftrightarrow \mathrm{2CO + 2H_2}\ (\Delta \mathrm{H^0_{298K}} = 247\ \mathrm{kJ/mol})$$

ULSAN NATIONAL INSTITUTE OF SCIENCE AND TECHNOLOGY

$$\mathrm{CH_4\ reactivity}\ [\frac{\mathrm{molecules}}{\mathrm{s}\cdot \mathrm{g}_{cat.}}] = \frac{\mathrm{H_{2_{detect}}[molecules/s]}}{2 \times \mathrm{weight\ of\ catalyst\ [g]}}$$

$$\mathrm{CH_4\ conversion} = \frac{[\mathrm{CH_4}]_{\mathrm{consumed}}}{[\mathrm{CH_4}]_{\mathrm{feed}}} \times 100\% = \frac{[\mathrm{H_2}]_{\mathrm{detect}}}{[\mathrm{H_2}]_{\mathrm{detect}} + 2[\mathrm{CH_4}]_{\mathrm{detect}}} \times 100\%$$

The Arrhenius equation is given by the following equation;

$$\mathrm{k} = \mathrm{Ae}^{-\mathrm{E_a}/(\mathrm{RT})}$$

where A is the pre-exponential factor for the reaction, R is the universal gas constant, T is the absolute temperature (in Kelvins), and k is the reaction rate coefficient. Taking the logarithm to the Arrhenius equation, the activation energy (E_a) can be evaluated from the slopes of the lines. The values of slopes were obtained from fitting values in a graph of a function of temperature.

ULSAN NATIONAL INSTITUTE OF SCIENCE AND TECHNOLOGY

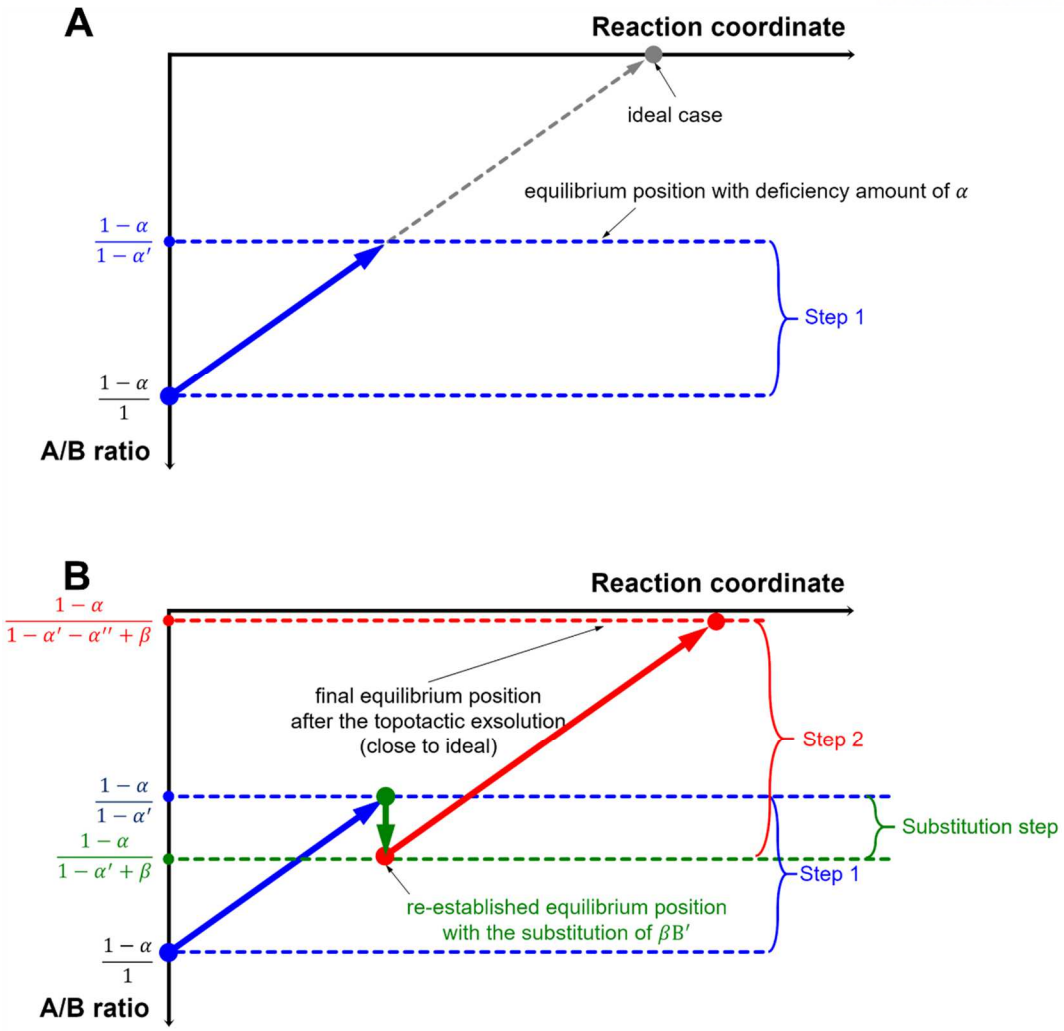

Figure 5-3 A/B ratio for the exsolution pathway. (A) Conventional exsolution pathway with deficiency amount of α. (B) Topotactic exsolution pathway with re-established equilibrium position through the substitution step of Fe cation into Ni site.

5.3. Result and discussion

5.3.1. Topotactic exsolution *via* ALD

In this study, Ni-doped lanthanum strontium titanate, $La_{0.6}Sr_{0.2}Ti_{0.85}Ni_{0.15}O_{3-\delta}$ was selected as a model system to study ALD-modified topotactic exsolution. As in our previous studies of topotactic exsolution, we chose Ni as the exsolving cation due to its higher co-segregation energy compared to other transition metals (*e.g.*, Mn or Fe), and we chose Fe as the guest cation.[27] The deposition of guest cations was carried out *via* ALD with varying cycles. The samples after the deposition were reduced at 850 ºC in a humidified hydrogen atmosphere. Table 5-1 Nomenclature for the compounds based on the Fe deposited LSTN system summarizes the samples that were characterized and the abbreviations we use to denote each composition.

In the original concept of A-site deficient perovskite, α moles of A-site vacancies in principle would be

ULSAN NATIONAL INSTITUTE OF SCIENCE AND TECHNOLOGY

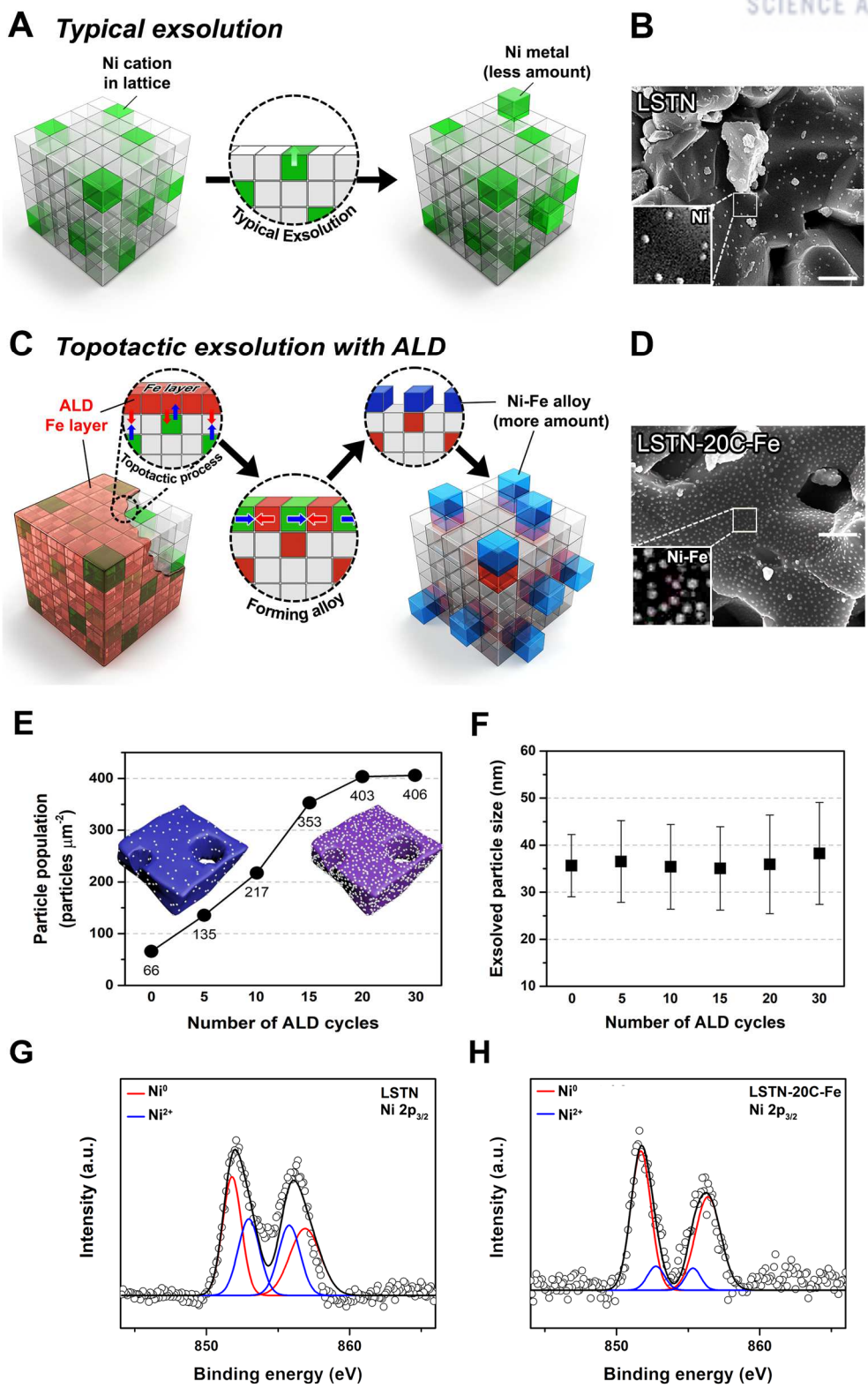

Figure 5-4 Schematic comparison, scanning electron microscopy images, the correlation between the number of ALD cycles and the particle size/population, and X-ray photoelectron curves for the samples. (A) Conventional exsolution for LSTN and (B) corresponding SEM image of LSTN; scale bar is 500 nm. (C) topotactic exsolution *via* ALD for LSTN-20C-Fe and corresponding SEM image of (D) LSTN-20C-Fe after reduction; scale bar is 500 nm. (E) Exsolved particle population from 0 to 30 ALD cycles. (F) Particle size distribution from 0 to 30 ALD cycles. X-ray photoelectron curves of (G) LSTN after reduction and (H) LSTN-20C-Fe.

ULSAN NATIONAL INSTITUTE OF SCIENCE AND TECHNOLOGY

stoichiometry with the A/B ratio of unity (ideal case in Figure 5-3A). However, under typical reducing conditions, only some of the B-site elements can be exsolved and the inactive cations remain in the bulk so that the A/B ratio cannot reach unity (Step 1 in Figure 5-3A and Eq.2). By the way, if only the value of A/B ratio can be lowered, it would lead to a new equilibrium position to make particle exsolution much more dynamic. The topotactic exsolution[24] can be utilized here as a way to lower the A/B ratio value. That is, introduced the guest cation B' can be substituted into B-site (Substitution step in Figure 5-3B and Eq.3), enabling the structure to establish a new equilibrium position toward more active exsolution. As a result, the substitution step could lead to a larger number of exsolved particles. We term this exsolution facilitation process 'topotactic exsolution' throughout this study (Step 2 in Figure 5-3B Eq. 3).

$$A_{1-\alpha}BO_{3-\delta} \xrightarrow{\text{Exsolution}} (1-\alpha)ABO_{3-\delta'} + \alpha B, \text{ (ideal) (1)}$$

$$A_{1-\alpha}BO_{3-\delta} \xrightarrow{\text{Exsolution:Step 1}} A_{1-\alpha}B_{1-\alpha'}O_{3-\delta''} + \alpha' B, \text{ (conventional exsolution) (2)}$$

$$A_{1-\alpha}BO_{3-\delta} + B'O_{(\text{deposited})} \xrightarrow{\text{Substitution step}} A_{1-\alpha}B_{1-\alpha'}B'_{\beta}O_{3-\delta'''} + \alpha' B$$

$$\xrightarrow{\text{Topotactic exsolution: Step 2}} A_{1-\alpha}B_{1-\alpha'-\alpha''}B'_{\beta}O_{3-\delta''''} + (\alpha' + \alpha'')B.$$

(topotactic exsolution) (3)

ULSAN NATIONAL INSTITUTE OF
SCIENCE AND TECHNOLOGY

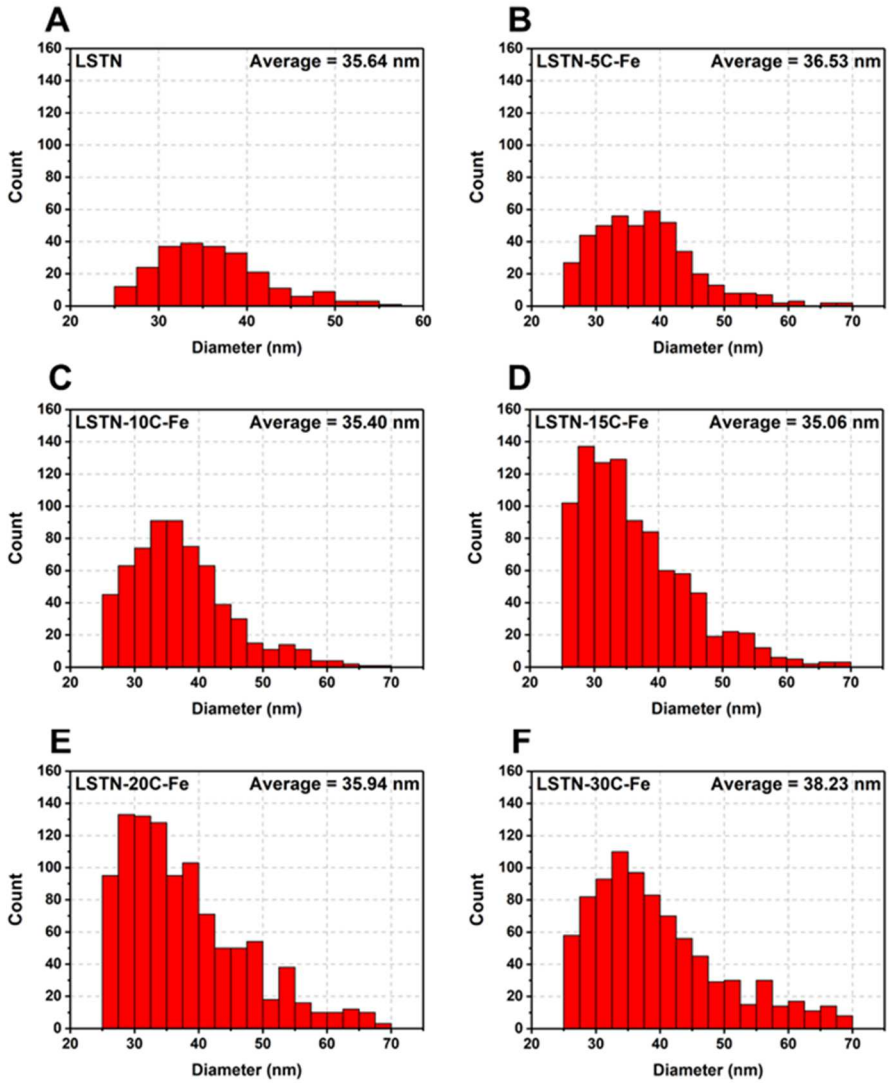

Figure 5-5 Particle size distributions for the samples. The histogram of the particle size distribution for (A) LSTN, (B) LSTN-5C-Fe, (C) LSTN-10C-Fe, (D) LSTN-15C-Fe, (E) LSTN-20C-Fe, and (F) LSTN-30C-Fe.

5.3.2. The relationship between the ALD cycle and the number of exsolved particles

To provide insight into the topotactic exsolution process, the correlation between the ALD cycle and the number of exsolved particles was investigated using scanning electron microscopy (SEM). Figure 5-4, A and C show a schematic illustration for the comparison of existing exsolution and the topotactic exsolution. In the case of the conventional exsolution concept of A-site deficient perovskite, a limited fraction of B-site cations can be released toward the incomplete stoichiometry equilibrium in typical reducing conditions. On the contrary, for the topotactic exsolution, a larger portion of B-site cations can be pushed out because of the lowered A/B ratio value (Figure 5-3B). To quantitatively determine the number of exsolved particles in relation to the number of ALD cycles, the number of particles in the corresponding area of the SEM images for the reduced pristine (Figure 5-4B) and Fe ALD modified

ULSAN NATIONAL INSTITUTE OF
SCIENCE AND TECHNOLOGY

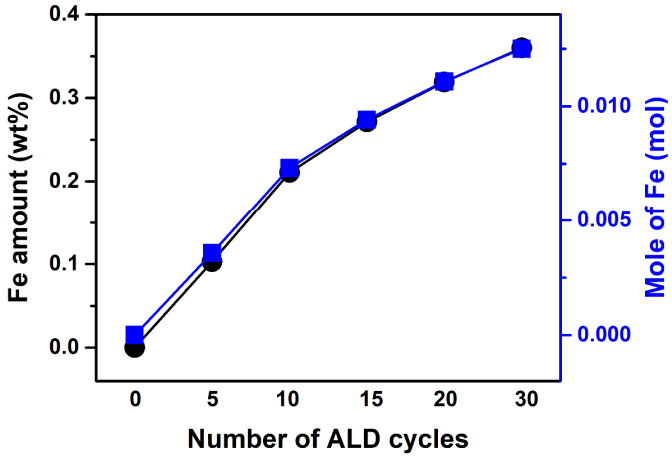

Figure 5-6 Growth curves for ALD layers on LSTN powder. All measures were measured after thermal treatment to ensure the removal of moisture content.

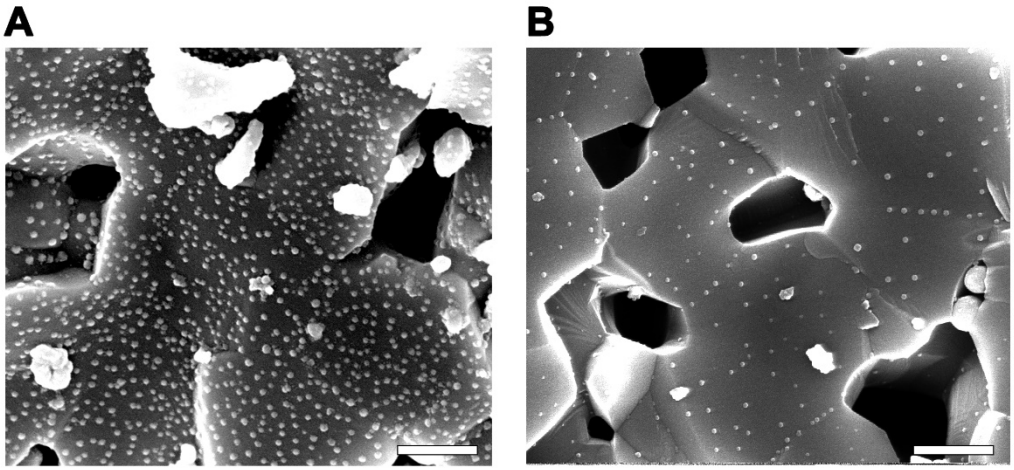

Figure 5-7 SEM image of (A) LSTN-20C-Fe and (B) pristine LSTN reduced for 30 minutes; scale bars are 500 nm.

samples (Figure 5-4D and Figure 5-1C-F) was counted by ImageJ software (Figure 5-1B). As shown in Figure 5-4E, the particle population per unit area was found to increase as the number of ALD cycles increases. The average size of particles is shown in Fig. 1F. On the other hand, before reduction, it was confirmed that all samples had a smooth surface regardless of ALD cycles (Figure 5-1G-H). The exsolved nanoparticles of 25-50 nm are uniformly distributed on the surface of all samples (Figure 5-1 and Figure 5-5). It can be seen that the number of ALD cycles does not affect the size of exsolved particles. Notably, at 20 cycles, the particle population reaches 403 particles μm^{-2}, which is about 6-fold more than that of pristine LSTN. The number of particles at 30 cycles does not seem to increase, indicating that the facilitation of exsolution is saturated at a certain level of deposition amount. The enhancement in the population density of particles is comparable to that obtained by voltage-driven reduction with a population density of about 400 particles μm^{-2}.[23]

ULSAN NATIONAL INSTITUTE OF SCIENCE AND TECHNOLOGY

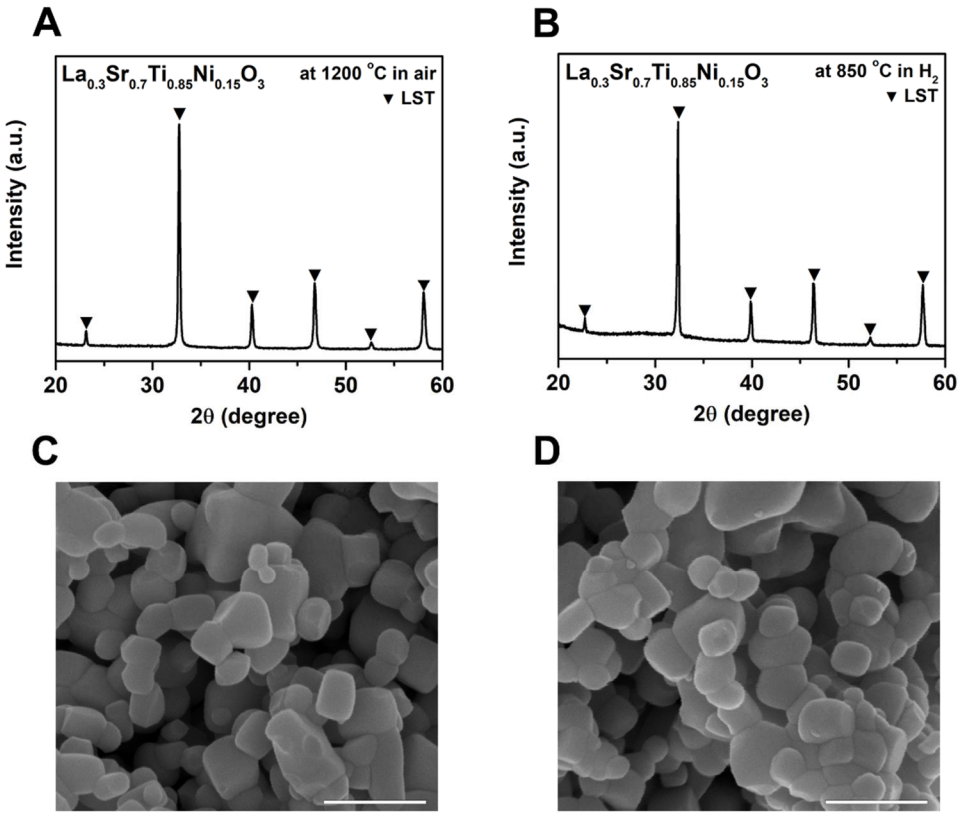

Figure 5-8 X-ray diffraction patterns of (A) $La_{0.3}Sr_{0.7}Ti_{0.85}Ni_{0.15}O_3$ before reduction and (B) $La_{0.3}Sr_{0.7}Ti_{0.85}Ni_{0.15}O_3$ after reduction. SEM images of (C) $La_{0.3}Sr_{0.7}Ti_{0.85}Ni_{0.15}O_3$ before reduction and (D) $La_{0.3}Sr_{0.7}Ti_{0.85}Ni_{0.15}O_3$ after reduction; scale bars are 500 nm.

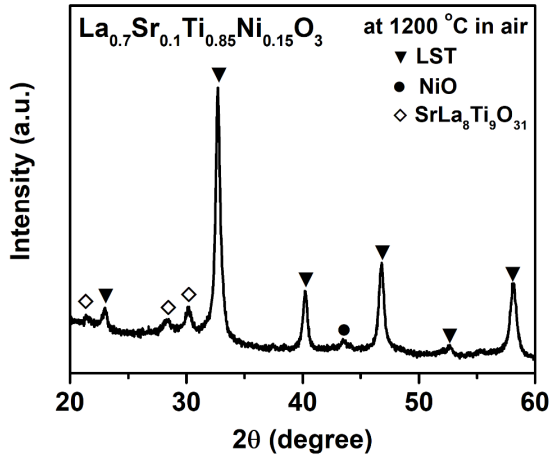

Figure 5-9 X-ray diffraction patterns of $La_{0.7}Sr_{0.1}Ti_{0.85}Ni_{0.15}O_3$ before reduction.

Furthermore, it is confirmed that exsolution is promoted even with a very small amount of ALD deposited Fe oxide. The growth rate of Fe_2O_3 layer formed by ALD was measured by inductively coupled plasma optical emission spectrometry (ICP-OES) and the data are shown in Figure 5-6. The left axis represents wt% of Fe deposited on the LSTN substrate and the right axis represents mol of Fe

ULSAN NATIONAL INSTITUTE OF SCIENCE AND TECHNOLOGY

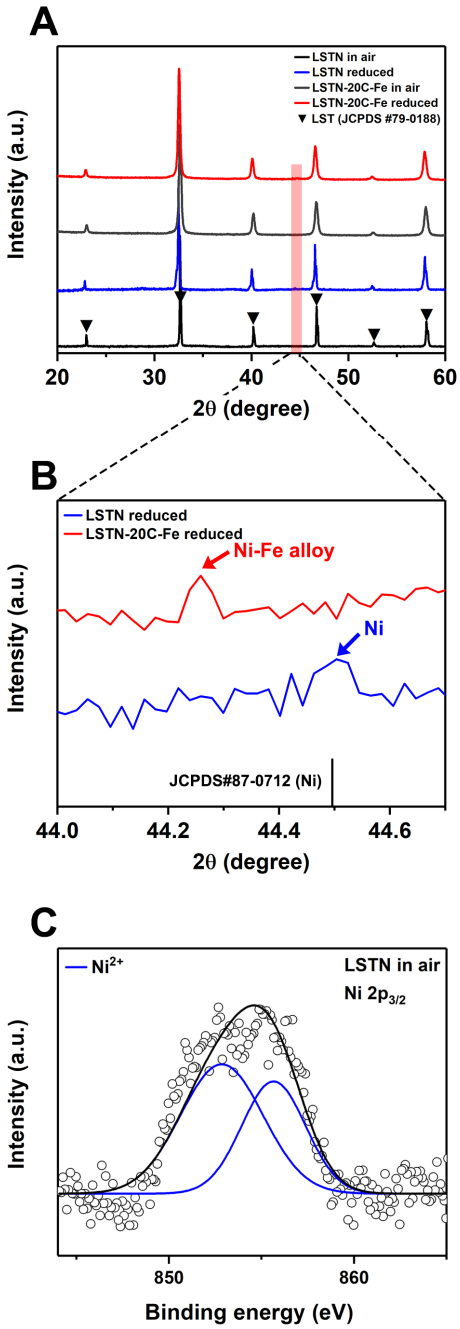

Figure 5-10 X-ray diffraction patterns and X-ray photoelectron curves of the samples. X-ray diffraction patterns of (A) LSTN and LSTN-20C-Fe before/after reduction (red highlights around 44.5 º indicate exsolved metals) and (B) magnified metal peaks for LSTN and LSTN-20C-Fe. (C) X-ray photoelectron curves of LSTN before reduction.

for the weight percentage to 1 mol of LSTN. Interestingly, only 0.011 mol of Fe was required using ALD whereas 0.176 mol of Fe[24] was necessary using the infiltration method (Figure 5-6). This effectiveness of topotactic exsolution using ALD shows about 16 times higher than that of using the previous infiltration due to the features of regular and thin deposition of ALD. Besides, with the advantage of the fast diffusion rate of the Fe oxide layer via ALD, this solution outperforms the existing

ULSAN NATIONAL INSTITUTE OF SCIENCE AND TECHNOLOGY

methods in terms of the rate of producing nanoparticles. For example, in the case of LSTN-20C-Fe, a similar number of nanoparticles were produced in only 30 minutes as compared to that of 4 hours of reduction (Figure 5-7). In comparison, the sample of LSTN without the deposition of Fe, much fewer particles were formed than LSTN-20C-Fe reduced for 30 minutes, indicating that topotactic exsolution is advantageous over conventional methods not only in quantitative but also in the length of the process.

5.3.3. X-ray diffraction and X-ray photoelectron spectroscopy

The perovskite oxides were examined by X-ray diffraction before and after reduction. In the ABO_3 perovskite structure, the oxygen non-stoichiometry determined by the ratio or type of A/B elements can vary the amount of B-site dopant to be accommodated. We increased the amount of Ni doping by about 2.5 to 5 times compared to the previous reports.[19], [20] Thus, several A-site deficiencies and La^{3+}/Sr^{2+} ratios were attempted to dissolve 0.15 mol Ni as B-site dopant. For example, the A-site and oxygen stoichiometric perovskite with the composition of $La_{0.3}Sr_{0.7}Ti_{0.85}Ni_{0.15}O_3$ displays no secondary phases or NiO peaks in air and even after the reduction, suggesting that Ni exsolution rarely occurs and the composition is not suitable for the exsolution study (Figure 5-8). The SEM images where the traces of Ni exsolution are hardly seen after a reduction are also in line with the XRD results. For the $La_{0.7}Sr_{0.1}Ti_{0.85}Ni_{0.15}O_3$ A-site deficiency of 0.2 mol with oxygen stoichiometric composition, NiO, La_2O_3, and $SrLa_8Ti_9O_{31}$ were segregated from the perovskite phase, implying that the La-rich composition may destabilize the perovskite structure (Figure 5-9). Therefore, we reduced a slight amount of La and devised a new composition of $La_{0.6}Sr_{0.2}Ti_{0.85}Ni_{0.15}O_{2.95}$ (LSTN) with A-site deficiency of 0.2 mol. The new composition showed a sufficient solubility of Ni in B-site without segregation of any secondary structure when sintered at 1200 ^oC in air with (pseudo-)cubic lattice parameters of 3.866 Å. Also, as confirmed at around 44.49 ^{o} (JCPDS card#87-0712) in a reducing condition (Figure 5-10), Ni exsolution was observed, which is consistent with the SEM results (Figure 5-4). After the deposition of Fe oxides through ALD, the patterns of reduced LSTN-20C-Fe do not deviate from those of LSTN in air. This can be interpreted that the amount of the deposited Fe oxides layer is only a few weight percent (Figure 5-6) and it does not affect the XRD pattern.[28] For the LSTN-20C-Fe as well, the peak for Ni (or Ni-Fe) was observed after a reduction.

X-ray photoelectron spectroscopy (XPS) was conducted to determine the oxidation states of the B-site dopants for the LSTN after reduction and LSTN-20C-Fe. The binding energy peaks of Ni ions are composed of Ni^{2+} $2p_{3/2}$ and Ni metal. 852.96 and 855.78 eV correspond to the peaks of multiplet Ni^{2+} $2p_{3/2}$, and 852.08 and 856.9 eV correspond to Ni metal and its satellite feature, respectively. As shown in (Figure 5-10C), the majority of species is NiO without the metallic Ni phase for LSTN in air. In contrast, during the reduction, the splitting of peaks between 850-860 eV progresses by the formation of metallic Ni particles due to the exsolution. For the reduced LSTN without the Fe ALD deposition, the metallic phase constitutes about 61 % of the total (Figure 5-4G). For the LSTN-20C-Fe, this is

ULSAN NATIONAL INSTITUTE OF
SCIENCE AND TECHNOLOGY

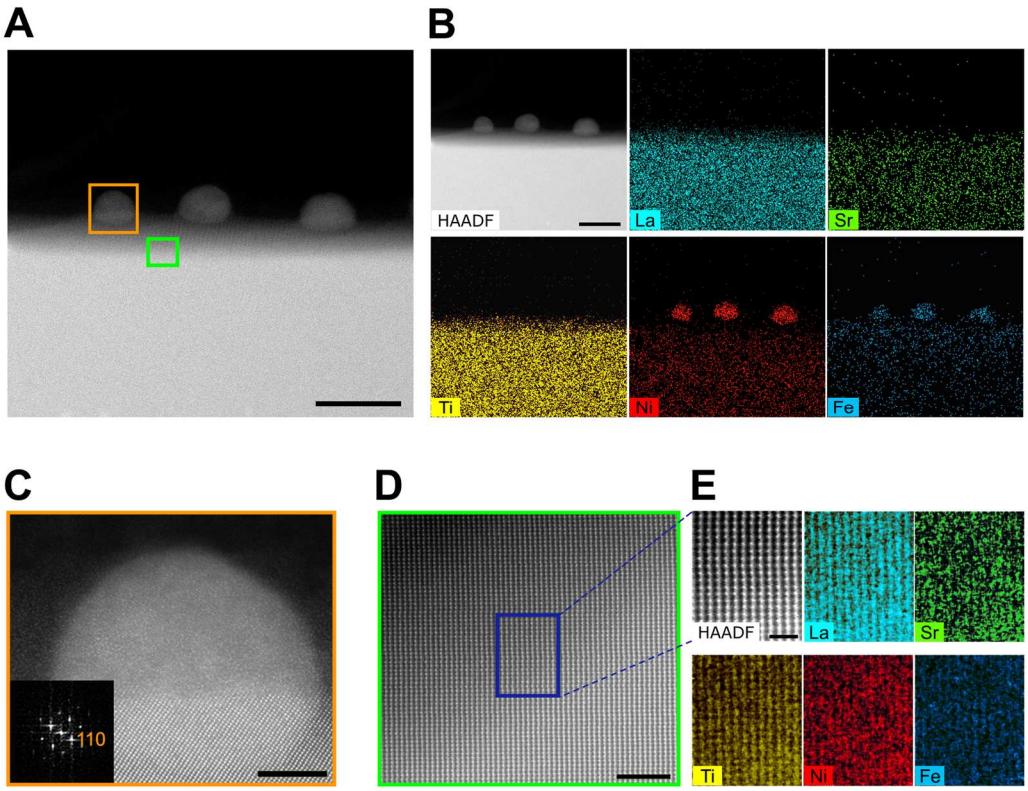

Figure 5-11 Transmission electron microscopy of exsolved particles on LSTN parent material. (A) HAADF scanning TEM image of LSTN-20C-Fe; scale bar 40 nm. (B) EDS elemental map of La, Sr, Ti, Ni, and Fe; scale bar 40 nm. (C) HAADF scanning TEM image of LSTN-20C-Fe and the corresponding fast-Fourier transformed pattern with zone axis=[100]; scale bar 5 nm. (D) HAADF scanning TEM image of the enlarged area; scale bar 3 nm. (E) EDS elemental map of La, Sr, Ti, Ni, and Fe in the parent material of LSTN-20C-Fe; scale bar 1 nm.

further intensified and the ratio of metal was found to be about 87 %, which means that most of Ni in the lattice were exsolved to the surface as a result of the topotactic exsolution. These results are in good agreement with the SEM results where the number of exsolved particles increases as the number of ALD cycles increases as shown in Figure 5-4 (B and D) and Figure 5-1A-F).

ULSAN NATIONAL INSTITUTE OF SCIENCE AND TECHNOLOGY

Table 5-2 EDS elemental analysis on exsolved Ni-Fe alloy particles on LSTN-10C-Fe and LSTN-20C-Fe.

Exsolved particle	Ni mole ratio of 1 mol Ni-Fe	
Number	**LSTN-10C-Fe**	**LSTN-20C-Fe**
Site #1	0.78	0.54
Site #2	0.62	0.66
Site #3	0.65	0.61
Site #4	0.69	0.61
Site #5	0.69	0.64
Site #6	0.70	0.54
Site #7	0.71	0.58
Average	0.69	0.60

Table 5-3 Co-segregation (B-site metal with an oxygen vacancy) and Ni↔TM exchange energies (in eV) on transition metal doped $La_{0.5}Sr_{0.5}TiO_3$(110).

Bulk	M-O_v-M co-segregation energy (eV)	Ni↔TM exchange energy (eV)
Ti	-0.12	-3.20
Cr	-1.05	-2.27
Fe	-1.45	-1.87
Mn	-1.89	-1.43
Co	-2.92	-0.40
Ni	-3.32	0
Cu	-4.32	1.00

5.3.4. High-resolution transmission electron microscopy analysis

In order to see the microstructure and composition of the exsolved particles and their interface with the perovskite lattice, we employed transmission electron microscopy (TEM). As shown in the high-angle annular dark field (HAADF) scanning TEM image of LSTN-20C-Fe (Figure 5-11), the nanoparticles with a diameter of around 30 nm were socketed on the surface of the perovskite parent oxide, which is consistent with the previous studies[20], [22]. As a result of energy dispersive spectroscopy (EDS), it is confirmed that the exsolved nanoparticles on the surface are composed of Ni and Fe (Figure 5-11B). This is one advantage of the topotactic exsolution bringing about multiple functionalities to the catalysts with producing alloys, as previously revealed.[24] As detailed in Table 5-2, Ni is the major component of the alloy composition at a ratio of 6:4, and Fe also accounts for a considerable amount. This can be explained by the result of DFT calculation where Fe also tends to exsolve to the surface along with Ni due to its higher co-segregation energy (-1.45 eV) than that of Ti. For the case of the perovskite bulk oxide, the components are identified as La, Sr, Ti, Ni, and Fe (Figure 5-11B). The lattice spacing between the planes of the bulk oxide is about 2.78 Å (Figure 5-11C), and this value is consistent with

ULSAN NATIONAL INSTITUTE OF SCIENCE AND TECHNOLOGY

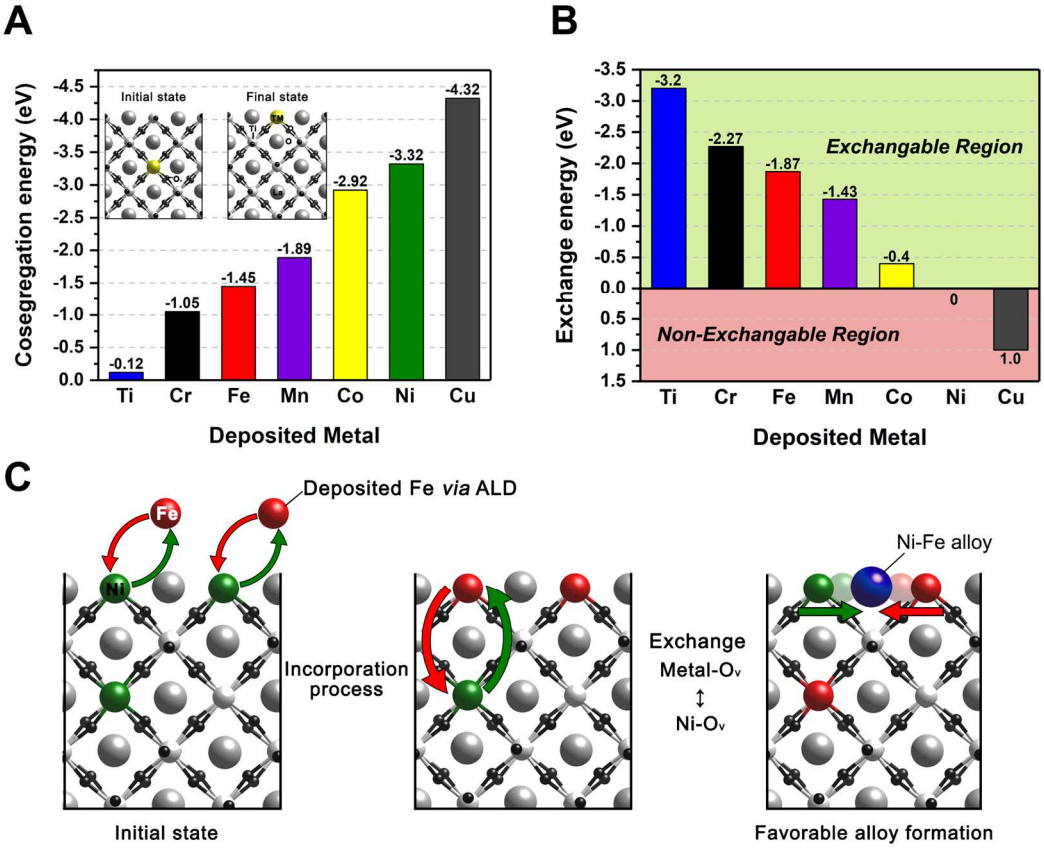

Figure 5-12 Schematics of the DFT model for the calculation of B-site metal co-segregation with an oxygen vacancy and cation exchange. (A) Co-segregation energy and (B) exchange energy comparison of various transition metals. (C) Schematics of the DFT calculations of the cation exchange and alloy formation.

the lattice constant of the (110) planes of LSTN-20C-Fe. As shown in Figure 5-11D-E, the HAADF scanning TEM and detailed atomic-scale scanning EDS mapping were conducted in the parent oxide to confirm the substitution of Fe into the parent LSTN. A pattern of the stripes as displayed in Figure 5-11D-E corresponds to the cubic lattice, verifying the presence of the Fe substitution into the lattice.

5.3.5. Density functional theory calculations

The effect of Fe infiltration on the enhancement of Ni exsolution on LSTN was further elucidated by DFT calculations. Based on previous experimental results where B-site metal exsolution preferentially occurred on the (110) termination of LSTN[20], we cleaved bulk LST to make LST(110) surface. We have previously shown that the different co-segregation tendency of transition metal dopants can be utilized for topotactic exsolution. That is, the co-segregation tendency of the depositing guest ion should be lower than that of the exsolving host ion.[24], [27], [29] Therefore, we examined the co-segregation energies for single dopant elements of various transition metals as well as host Ti cation (Figure 5-12A). Our DFT results show that co-segregation energy follows the order of Cu > Ni > Co > Mn > Fe > Cr > Ti (Table 5-3 and Figure 5-12A), implying that Ni in the bulk can be exchanged with deposited Fe. Fe

ULSAN NATIONAL INSTITUTE OF SCIENCE AND TECHNOLOGY

tends to exsolve more easily with higher co-segregation energy than the host Ti of LSTF (Figure 5-12B), which agrees with the previous result for Fe exsolution on LSTF[19]. Additionally, DFT-calculated cation exchange energies between guest transition metals and bulk Ni were shown in Figure 5-12B. A negative sign in exchange energy indicates that the deposited metal can spontaneously exchange with Ni. Cations of Co, Mn, Fe, Cr, and Ti exhibit spontaneous exchange energy, and the order of the exchange is the opposite of the co-segregation energy. For instance, Fe shows the highest exchange energy of -1.87 eV (Table 5-3 and Figure 5-12B-C) except for Ti and Cr, which signifies that the surface Fe can be preferentially substituted with the Ni in bulk of LSTN. On the contrary to the conventional exsolution where the stoichiometry of the perovskite may reach the limit of stoichiometric equilibrium of A- and B-site cations making the exsolution of Ni sluggish,[20] for the topotactic exsolution, the deposited Fe on the surface can induce the further exsolution of Ni by exchanging its position with Ni remained in bulk.

Furthermore, we explored the formation process of Ni-Fe alloy on the LST surface by calculating the surface alloy formation energy based on our previous work[29]. The formation of Ni-Fe alloy on the LST surface is thermodynamically favorable with the formation energy of -0.43 eV whereas the alloy formation is not favorable in bulk (0.08 eV). This is in good agreement with the TEM and catalytic property results.

ULSAN NATIONAL INSTITUTE OF SCIENCE AND TECHNOLOGY

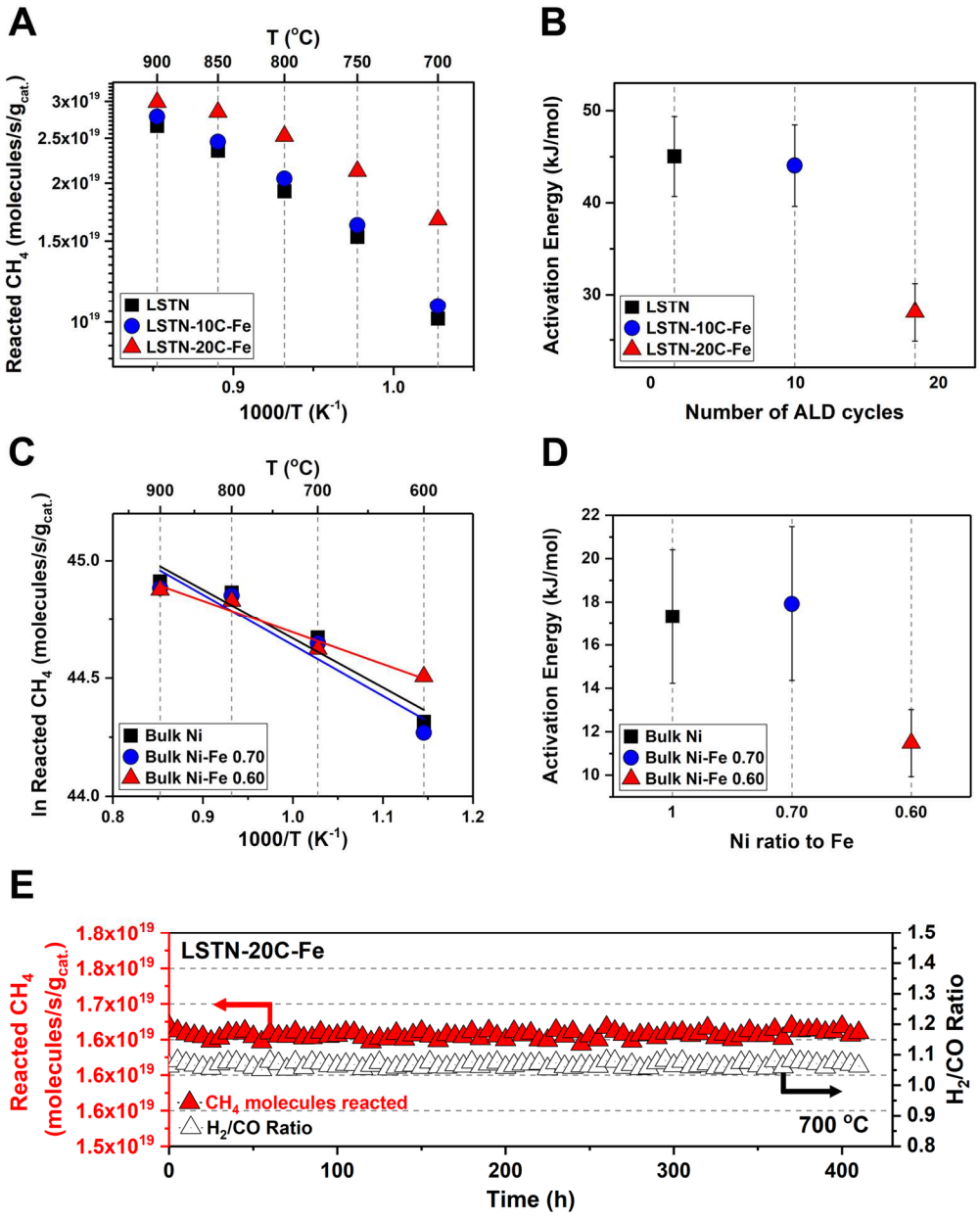

Figure 5-13 Catalytic properties for the DRM. (A) Reacted methane during the DRM reaction for LSTN, LSTN-10C-Fe, and LSTN-20C-Fe. (B) The activation energy of the methane reactivity calculated for LSTN, LSTN-10C-Fe, and LSTN-20C-Fe. (C) Arrhenius-type plots of reacted CH_4 for Bulk Ni and Bulk Ni-Fe alloy catalysts. (D) The activation energy of the methane reactivity calculated for Bulk Ni, Bulk Ni-Fe 0.70, and Bulk Ni-Fe 0.60. (E) Time-dependence of CH_4 reactivity and H_2/CO ratio for LSTN-20C-Fe in dry reforming of methane at 700 °C.

5.3.6. Catalytic property

The catalytic activity of the LSTN-*x*C-Fe for the dry reforming of methane (DRM) was evaluated by detecting the exiting gas through the catalyst located in the middle of the fixed-bed tube reactor. Figure 5-13 compares the catalytic behavior of the LSTN, LSTN-10C-Fe, and LSTN-20C-Fe samples. The

ULSAN NATIONAL INSTITUTE OF SCIENCE AND TECHNOLOGY

catalytic activity was measured in the temperature range of 700 to 900 ^{o}C with gas hourly space velocity (GHSV) = 30000 ml g^{-1} h^{-1}. As depicted in Figure 5-13A, the reacted methane for the LSTN-10C-Fe is slightly improved compared to LSTN, but that for the LSTN-20C-Fe is remarkably improved at 64 % compared to that of LSTN. In particular, as the temperature decreases, the degree of the activity decline is inversely proportional to the number of ALD cycles, which is related to activation energy shown in Figure 5-13B. The activation energies of LSTN and LSTN-10C-Fe are similar, and it decreases greatly at LSTN-20C-Fe, so it is presumed that the reactivity of the catalysts is proportional either to the number of exsolved particles or to the degree of the alloy formation. To identify this presumption, the three different ratios of Ni-Fe alloy catalysts (*e.g.*, the ratios of Ni to Fe are 1.0 to 0 (Bulk Ni), 0.70 to 0.30 (Bulk Ni-Fe 0.70), and 0.60 to 0.40 (Bulk Ni-Fe 0.60), respectively), on an inert support γ-Al_2O_3 were evaluated for the DRM test. In this way, the mechanism of the DRM can be assessed with a monofunctional pathway, where the methane reactant is dependent on the metal alone. As depicted in Figure 5-13C-D, Arrhenius-type plots for Bulk Ni and Bulk Ni-Fe alloys were plotted, from which the activation energies were calculated. Interestingly, the trends of the activation energy for the alloy catalysts on inert support appear analogous to those for the LSTN series, which demonstrates that the different ratios of Ni-Fe alloys were formed depending on the number of ALD cycles. This is supported by EDS elemental analysis shown in Table 5-2, *e.g.*, the average ratio of Ni to Fe is around 0.60 to 0.40 for the LSTN-20C-Fe sample. According to the DFT results, Fe also has a higher alloy formation energy, which is in accordance with the experimental result where the more Fe cations are substituted into the bulk, the higher the ratio of Fe exists in Ni-Fe alloy. Additionally, the stability of the particles obtained via topotactic exsolution was evaluated for LSTN-20C-Fe. In continuous DRM measurements (Figure 5-13E), the CH_4 reactivity remained constant over 400 hours, validating the durability of the supported metal catalyst.

5.4. Conclusions

In conclusion, we have employed topotactic exsolution reinforced by ALD on the widely used perovskite oxide, nickel doped lanthanum strontium titanate. As an effective means of producing alloy nanoparticles, topotactic exsolution with ALD has several noteworthy implications including (1) a larger population of exsolved nanoparticles, (2) the selective formation of alloy catalysts, and (3) a faster rate of the nanoparticle generation. Fe as guest transition metal exhibits the exchange energy of -1.87 eV with host Ni, resulting in the spontaneous exchange between Ni and Fe, topotactic exsolution. The spontaneously produced bimetallic catalysts in a short time are also excellent in catalytic activity in DRM, which not only improved the initial value by 64 % compared to pristine LSTN but also reduced activation energy by about 40 % with prolonged stability of 410 hours. This newly developed topotactic exsolution with ALD could serve as a general driving force applicable to other exsolution systems.

ULSAN NATIONAL INSTITUTE OF SCIENCE AND TECHNOLOGY

References

[1] D. Pakhare, J. Spivey, Chem. Soc. Rev. **2014**, 43, 7813.

[2] P. I. Cowin, C. T. G. Petit, R. Lan, J. T. S. Irvine, S. Tao, Adv. Energy Mater. **2011**, 1, 314.

[3] S. Sengodan, S. Choi, A. Jun, T. H. Shin, Y.-W. Ju, H. Y. Jeong, J. Shin, J. T. S. Irvine, G. Kim, Nat. Mater. **2014**, 14, 205.

[4] P. Szuromi, Science (80-.). **2019**, 366, 834.

[5] J. Lu, C. Zhu, C. Pan, W. Lin, J. P. Lemmon, F. Chen, Sci. Adv. **2018**, 4, eaar5100.

[6] V. Kyriakou, D. Neagu, G. Zafeiropoulos, R. K. Sharma, C. Tang, K. Kousi, I. S. Metcalfe, M. C. M. Van De Sanden, M. N. Tsampas, ACS Catal. **2020**, 10, 1278.

[7] Y. Chen, S. Yoo, K. Pei, D. Chen, L. Zhang, R. Murphy, B. Zhao, Y. Zhang, Y. Chen, M. Liu, Adv. Funct. Mater. **2018**, 1704907, 1.

[8] Y. Nishihata, J. Mizuki, T. Akao, H. Tanaka, M. Uenishi, M. Kimura, T. Okamoto, N. Hamada, Nature **2002**, 418, 164.

[9] R. Shiozaki, A. G. Andersen, T. Hayakawa, S. Hamakawa, K. Suzuki, M. Shimizu, K. Takehira, J. Chem. Soc. - Faraday Trans. **1997**, 93, 3235.

[10] Y. Gao, D. Chen, M. Saccoccio, Z. Lu, F. Ciucci, Nano Energy **2016**, 27, 499.

[11] Y. Li, W. Zhang, Y. Zheng, J. Chen, B. Yu, Y. Chen, M. Liu, Chem. Soc. Rev. **2017**, 46, 6345.

[12] G. Dimitrakopoulos, A. F. Ghoniem, B. Yildiz, Sustain. Energy Fuels **2019**, 3, 2347.

[13] N. W. Kwak, S. J. Jeong, H. Gil Seo, S. Lee, Y. Kim, J. K. Kim, P. Byeon, S.-Y. Chung, W. Jung, Nat. Commun. **2018**, 9, 4829.

[14] Y. R. Jo, B. Koo, M. J. Seo, J. K. Kim, S. Lee, K. Kim, J. W. Han, W. C. Jung, B. J. Kim, J. Am. Chem. Soc. **2019**, 141, 6690.

[15] X. Lv, H. Chen, W. Zhou, F. Cheng, S. D. Li, Z. Shao, Renew. Energy **2020**, 150, 334.

[16] K. Kousi, D. Neagu, L. Bekris, E. I. Papaioannou, I. S. Metcalfe, Angew. Chemie - Int. Ed. **2020**, 59, 2510.

[17] H. Han, J. Park, S. Y. Nam, K. J. Kim, G. M. Choi, S. S. P. Parkin, H. M. Jang, J. T. S. Irvine, Nat. Commun. **2019**, 10, 1.

[18] M. B. Katz, S. Zhang, Y. Duan, H. Wang, M. Fang, K. Zhang, B. Li, G. W. Graham, X. Pan, J. Catal. **2012**, 293, 145.

[19] D. Neagu, G. Tsekouras, D. N. Miller, H. Menard, J. T. S. Irvine, Nat Chem **2013**, 5, 916.

[20] D. Neagu, T. S. Oh, D. N. Miller, H. Menard, S. M. Bukhari, S. R. Gamble, R. J. Gorte, J. M. Vohs, J. T. S. Irvine, Nat Commun **2015**, 6, 8120.

[21] Y. Zhu, X. Liu, S. Jin, H. Chen, W. Lee, M. Liu, Y. Chen, J. Mater. Chem. A **2019**, 7, 5875.

[22] T. S. Oh, E. K. Rahani, D. Neagu, J. T. S. Irvine, V. B. Shenoy, R. J. Gorte, J. M. Vohs, J. Phys. Chem. Lett. **2015**, 6, 5106.

[23] J. Myung, D. Neagu, D. N. Miller, J. T. S. Irvine, Nature **2016**, 537, 528.

ULSAN NATIONAL INSTITUTE OF SCIENCE AND TECHNOLOGY

[24] S. Joo, O. Kwon, K. Kim, S. Kim, H. Kim, J. Shin, H. Y. Jeong, S. Sengodan, J. W. Han, G. Kim, Nat. Commun. **2019**, 10, 697.

[25] D. Ding, X. Li, S. Y. Lai, K. Gerdes, M. Liu, Energy Environ. Sci. **2014**, 7, 552.

[26] C. Lin, J. B. Jang, L. Zhang, E. A. Stach, R. J. Gorte, ACS Catal. **2018**, 8, 7679.

[27] O. Kwon, S. Sengodan, K. Kim, G. Kim, H. Y. Jeong, J. Shin, Y.-W. Ju, J. W. Han, G. Kim, Nat. Commun. **2017**, 8, 15967.

[28] T. M. Onn, M. Monai, S. Dai, E. Fonda, T. Montini, X. Pan, G. W. Graham, P. Fornasiero, R. J. Gorte, J. Am. Chem. Soc. **2018**, 140, 4841.

[29] O. Kwon, K. Kim, S. Joo, H. Y. Jeong, J. Shin, J. W. Han, S. Sengodan, G. Kim, J. Mater. Chem. A **2018**, 6, 15947.

[30] D. Chen, R. Ran, K. Zhang, J. Wang, Z. Shao, J. Power Sources **2009**, 188, 96.

[31] Z. Shao, W. Yang, Y. Cong, H. Dong, J. Tong, G. Xiong, J. Memb. Sci. **2000**, 172, 177.

[32] G. Chen, W. Zhou, D. Guan, J. Sunarso, Y. Zhu, X. Hu, W. Zhang, Z. Shao, Sci. Adv. **2017**, 3, e1603206.

[33] C. Lin, A. C. Foucher, Y. Ji, C. D. Curran, E. A. Stach, S. McIntosh, R. J. Gorte, ACS Catal. **2019**, 9, 7318.

[34] G. Kresse, J. Furthmuller, Phys. Rev. B **1996**, 54, 11169.

[35] G. Kresse, J. Hafner, J. Phys. Condens. Matter **1994**, 6, 8245.

[36] M. Perdew, J. P., Burke, K. & Ernzerhof, Phys. Rev. Lett. **1996**, 77, 3865.

[37] H. J. Monkhorst, J. D. Pack, Phys. Rev. B **1976**, 13, 5188.

ULSAN NATIONAL INSTITUTE OF SCIENCE AND TECHNOLOGY

List of Publications

15. **Sangwook Joo,†** Kyeounghak Kim,† Ohhun Kwon, Jinkyung Oh, Linjuan Zhang, Jing Zhou, Jian-Qiang Wang, Hu Young Jeong, Jeong Woo Han*, and Guntae Kim*
"Enhancing Thermocatalytic Activities via Up-shift of the d-Band Center of Exsolved Co-Ni-Fe Ternary Alloy Nanoparticles for Dry Reforming of Methane " Submitted to Applied Catalysis B: Environmental

14. **Sangwook Joo,†** Chaehyun Lim,† Ohhun Kwon, Hu Young Jeong, Yong-wook Sin, Sihyuk Choi*, and Guntae Kim*
"The First Observation of Ni Nanoparticle Exsolution from YSZ and its Application for Dry Reforming of Methane" Submitted to Materials Reports Energy. (2020)

13. Kyeounghak Kim, **Sangwook Joo**, Rui Huang, Hyung Jun Kim, Guntae Kim*, and Jeong Woo Han*
"Mechanistic insights into phase transition phenomena from simple to layered perovskite under reducing conditions to enhance the catalytic activity" **Energy & Environmental Science.** Just Accepted (2020)

12. Hyunmin Kim,† **Sangwook Joo,†** Ohhun, Kwon, Sihyuk Choi*, and Guntae Kim*
"Cobalt-free Pr0.5Ba0.4Sr0.1FeO3-δ as a highly efficient cathode for commercial YSZ-supported solid oxide fuel cell" **ChemElectroChem.** 4378–4382 (2020)

11. **Sangwook Joo,†** Arim Seong,† Ohhun Kwon, Kyeounghak Kim, Hu Young Jeong, Raymond J. Gorte, John M. Vohs, Jeong Woo Han, and Guntae Kim*
"Atomic Layer Deposition-Engineered Topotactic Exsolution for Fast and Abundant Nanoparticles on Nickel Doped Lanthanum Strontium Titanate" **Science Advances.** 6, eabb1573 (2020)

10. Jeongwon Kim, Yejin Yang, Arim Seong, Hyuk-Jun Noh, Changmin Kim, **Sangwook Joo**, Ara Cho, Linjuan Zhang, Jing Zhou, Jian-Qiang Wang, Jeong Woo Han, Javeed Mahmood,* Jong-Beom Baek* and Guntae Kim*
"Identifying Electrocatalytic Active Sites of Ru-based Catalyst with High Faraday Efficiency in CO_2 saturated media for Aqueous Zn-CO_2 System" **J. Mater. Chem.** 8, 14927-14934 (2020)

9. Ohhun Kwon,† **Sangwook Joo,†** and Guntae Kim*

ULSAN NATIONAL INSTITUTE OF SCIENCE AND TECHNOLOGY

"Review on exsolution and its driving forces in perovskites" **Journal of Physics: Energy.** 2, 032001 (2020)

8. Arunchander Asokan,† Chaehyun Lim,† Jeongwon Kim,† Ohhun Kwon, Hansol Lee, **Sangwook Joo**, Hu Young Jeong, and Guntae Kim*
"Carbon nanofibers encapsulated nickel-molybdenum nanoparticles as hydrogen evolution catalysts for aqueous Zn-CO_2 system" **ChemNanoMat.** 6, 937-946 (2020)

7. **Sangwook Joo,†** Ohhun Kwon,† Seona Kim, Hu Young Jeong, and Guntae Kim*
"Ni-Fe Bimetallic Nanocatalysts Produced by Topotactic Exsolution in Fe deposited $PrBaMn_{1.7}Ni_{0.3}O_{5+d}$ for Dry Reforming of Methane" **J. Electrochem. Soc.** 167, 064518 (2020).

6. Yunfei Bu,† **Sangwook Joo,†** Yanxiang Zhang†, Yifan Wang, Dandan Meng, Xinlei Ge*, and Guntae Kim*
"A Highly Efficient Composite Cathode for Proton-Conducting Solid Oxide Fuel Cells" **Journal of Power Sources.** 451, 227812 (2020)

5. Changmin Kim,† Jeongwon Kim,† **Sangwook Joo**, Yejin Yang, Jeeyoung Shin, Meilin Liu, Jaephil Cho,* and Guntae Kim*
"Highly Efficient CO_2 Utilization via Aqueous Zinc– or Aluminum–CO_2 Systems for Hydrogen Gas Evolution and Electricity Production" **Angew. Chem. Int.** Ed 58, 9506-9511 (2019)

4. **Sangwook Joo,†** Ohhun Kwon,† Kyeounghak Kim, Seona Kim, Hyunmin Kim, Jeeyoung Shin, Hu Young Jeong, Sivaprakash Sengodan, Jeong Woo Han, and Guntae Kim*
"Cation-swapped homogeneous nanoparticles in perovskite oxides for high power density" **Nature Communications**. 697 (2019)

3. Changmin Kim,† Jeongwon Kim,† **Sangwook Joo**, Yunfei Bu, Meilin Liu, Jaephil Cho,* and Guntae Kim*
"Efficient CO_2 utilization via a hybrid Na-CO_2 system based on CO_2 dissolution " **iScience**. 9, 278-285 (2018)

2. Ohhun Kwon, Kyeounghak Kim, **Sangwook Joo**, Hu Young Jeong, Jeeyoung Shin, Jeong Woo Han, Sivaprakash Sengodan* and Guntae Kim*
"Self-assembled alloy nanaparticles in a layered double perovskite as a fuel oxidation catalyst for solid oxide fuel cells" **Journal of Materials Chemistry A**. 6, 15947 (2018)

ULSAN NATIONAL INSTITUTE OF
SCIENCE AND TECHNOLOGY

1. **Sangwook Joo**, Junyoung Kim, Jeeyoung Shin*, Tak-Hyoung Lim*, and Guntae Kim*
"Investigation of a Layered Perovskite for IT-SOFC Cathodes: B-Site Fe-Doped $YBa_{0.5}Sr_{0.5}Co_{2-x}Fe_xO_{5+\delta}$" **J. Electrochem. Soc.** 163 (14) F1489-F1495 (2016)

ULSAN NATIONAL INSTITUTE OF
SCIENCE AND TECHNOLOGY

Acknowledgments

I would like to express my little appreciation to many people for their help to complete my degree. First and foremost I want to thank my Ph. D. advisor, Prof. Guntae Kim, you have been a tremendous mentor for me. I would like to thank you for encouraging my research and for allowing me to grow as a research scientist. Your advice on both research as well as on my career has been priceless. Additionally, I would like to express my gratitude to my committee members, Prof. Jong-Beon Baek, Prof.Hyun-Kon Song, Prof. Jeong Woo Han, Prof. WooChul Jung for their generous advice and encouragement.

I also thank our group members of ‘gunslab’. As my name Sangwook stands for, I’ve always tried to do ‘win-win’ with them, and they’ve supported me in accomplishing research achievement and personal growth: I would like to thank Prof. Sivaprakash Sengodan, Dr. Seonyoung Yoo, Prof. Sihyuk Choi, Dr. Areum Jun, Dr. Junyoung Kim, Dr. Seona Kim, Dr. Changmin Kim, Dr. Chaehyun Lim, Dr. Ohhun Kwon, Dr. Arunchander Asokan, Dr. Donghwi Jeong, Gihyeon Kim, Jeongwon Kim, Seungtae Lee, Hyunmin Kim, Arim Seong, Yejin Yang, Hyojae Hwang, Sewon Pyo, Minseo Kim, Hyoi Jo, Jinkyung Oh, Prof. Jeeyoung Shin, Prof. Young-Wan Ju, and Prof. Yunfei Bu. I wish you all the best in the future.

And lastly, I would like to appreciate my parents, my sister, my grandmother, and all of my family for their support and sacrifice.